Class of Science

PhD Thesis in Biophysical Sciences

Intravital Two Photon Calcium Imaging of Glioblastoma Mouse Models

Candidate:

Vinoshene Pillai

Supervisor:

Prof. Gian Michele Ratto

2020/2021

Preface

This dissertation presents my work as a PhD student (2015-2021). These years have been very educational in both a personal and a professional way. I did my bachelor in Pure Chemistry and later majored in organic Chemistry during my master. Thus, coming from a different scientific discipline, it took me quite an effort to understand and learn a lot of new techniques while building credibility in this new field of research. Nevertheless, I appreciate to be given the opportunity to pursue my doctorate at SNS, especially in Ratto Lab where I was involved in a variety of different projects.

Main project:

- **Intravital imaging of glioblastoma mouse models**. Cellular signaling is an important mechanism of communication. In glioblastoma (GBM), calcium signaling has been identified to promote its progression and malignancy. Therefore, in this project, I performed two photon imaging to visualize and quantify intracellular calcium activity of tumor cells in a murine GBM model (GL261 model). Fluorescence time lapse imaging is a powerful technique that gives insights on cellular motility and processes at single cell resolution in live animals. This technique is proven to be valuable for characterizing and quantifying cellular signaling in tumor cells, revealing its involvement in tumor proliferation and migration. As a qualitative evaluation of brain tumor activity, I also explored wide-field imaging, which is currently a popular imaging technique to visualize brain activity at a mesoscale level. Apart from developing a fluorescent GBM model using the well-established GL261 cell line, I exploited new molecular techniques to produce a spontaneous murine GBM model. This model closely resembles the human pathology and allows us to study GBM in a developmental model. *Manuscript in preparation*.

Other projects:

- ***In vivo* detection of murine glioblastoma through multimodal imaging technique**. The aim of this project is to discriminate healthy brain from GBM tissues in GL261 mouse model through the combination of Raman and reflectance spectroscopies. My role was in tumor cell transfection, animal preparation and performing two photon imaging experiments. *Baria et al. Neurophotonics, 2020* (2)

- **Modeling genetic mosaicism of neurodevelopmental disorders *in vivo* by a Cre-amplifying fluorescent reporter (Beatrix)**. The comprehension of the mechanisms behind genetic mosaicism in neurodevelopmental disorders requires the generation of sparse mosaic models, where each neuron is univocally identified by the expression of a fluorescent protein *in vivo*. Beatrix is a novel tool that can be used to create mosaicism

with tunable degree. I was involved in this project by performing *in utero* electroporation in order to generate a mouse model of the human disease Type II Focal Cortical Dysplasia. I have also performed the electrophysiology experiments that provided the first available description of the physiological phenotype of this disease. Furthermore, this tool is going to be an intrinsic part of my future study, where it will be utilized to generate an inducible GBM mouse model. *Trovato et al. Nature Comm, 2020* (1)

- **PCDH19 female epilepsy**. PCDH19 is neurological condition characterized by early-onset seizures, intellectual disability, and autism. It is caused by the X-chromosome gene PCDH19 that encodes for the protein protocadherin-19, whose function in the brain remains unknown. I was involved in performing preliminary *in vivo* electrophysiological recordings and analysing early data that indicates PCDH19 involvement in synaptic transmission. I also trained a master student on experimental techniques used in this project. *Manuscript submitted to Nature Neuroscience*.

- **Diurnal regulation of intracellular chloride *in vivo***. Fast synaptic inhibition relies on the regulation of intracellular chloride ($(Cl^-)_i$). In this project, we have discovered that neuronal $(Cl^-)_i$ concentration follows a circadian regulation where there is high $(Cl^-)_i$ concentration at night and low $(Cl^-)_i$ concentration during day. A major hypothesis is that by lowering $(Cl^-)_i$ concentration, it raises synaptic inhibitory function and therefore, reduces epileptic pathophysiology at the time of sleep. In this project, I performed *in vivo* electrophysiology experiments on anesthetized mice to study susceptibility to induced epilepsy at different time of the day. Then I was also involved in doing chronic implants in behaving mice trained to move on a polystyrene ball while EEG at different time of the day is being recorded. *Manuscript submitted to Cell*.

Published papers:

1. Trovato, F., Parra, R., Pracucci, E., Landi, S., Cozzolino, O., Nardi, G., Cruciani, F., **Pillai, V.**, Mosti, L., Cwetsch, A. W., Cancedda, L., Gritti, L., Sala, C., Verpelli, C., Maset, A., Lodovichi, C., Ratto, G. M. (2020). Modelling genetic mosaicism of neurodevelopmental disorders in vivo by a Cre-amplifying fluorescent reporter. *Nature Communications*, 11, 6194.

2. Baria, E., Praccuci, E., **Pillai, V.**, Pavone, F. S., Ratto, G. M., Cicchi, R. (2020). In vivo detection of murine glioblastoma through Raman and reflectance fibre-probe spectroscopies. *Neurophotonics*, 7(4), 045010.

3. Pracucci, E., **Pillai, V.**, Lamers, D., Parra, R., Landi, S. (2021). Neuroinflammation: a signature or a cause of epilepsy? *International Journal of Molecular Sciences*.

Submitted papers:

1. Pracucci, E., Graham, R., Alberio, Laura., Nardi, G., Cozzolino, O., **Pillai, V.**, Saieva, L., Walsh, D., Landi, S., Zhang, J., Trevelyan, A. J., Ratto, G.M. (2021). Circadian rhythm in cortical chloride homeostasis underpins variation in network excitability. *Cell*.

1. Lamers, D., Landi, S., Mezzena, R., Baroncelli, L., **Pillai, V.**, Cruciani, F., Migliarini, S., Mazzoleni, S., Pasqualetti, M., Passafaro, M., Bassani, S., Ratto, G. M. (2021). Cortical excitability in a conditional model of PCDH19 epilepsy. *Nature Neuroscience*.

ABSTRACT

Glioma is a brain tumor that derives from glial cells and it represents about 40% of all diagnosed central nervous system tumors. The most common type of glioma is glioblastoma multiforme (GBM), which is one of the most malignant tumors that can affect humans, with a median life expectancy of only 14 months. Its invasive properties and the presence of the blood-brain barrier makes GBM very hard to treat. Furthermore, GBM has a high degree of cellular and genetic heterogeneity, and the study of its genome is a very active field of research. As such, it complicates the diagnosis, treatment and prognosis. Recently, researchers are focusing on alterations in cellular signaling processes related to central nervous system (CNS) pathologies and diseases. Crosstalk among neurons, glial cells and/or between neurons and glial cells is important in controlling cellular processes, including cell proliferation, cell division and programmed cell death. Calcium signaling has been proposed to be directly involved in GBM proliferation, motility and invasion, but there are no demonstrations *in vivo* of the correlation between GBM cell motility and calcium signaling. In light of this idea, we have modified the mouse glioma cell strain (GL261) to express a red fluorescent protein and a genetically encoded calcium sensor (GCaMP6s). Two photon imaging data that we acquired demonstrate that most of the tumor volume, i.e. the core, is occupied by tightly packed spherical cells characterized by reduced cellular motility and low intracellular calcium ($(Ca^{2+})_i$) activity. This core is surrounded by sparse cells displaying a very polarized morphology that migrate at a higher rate. These cells in the peripheral region are characterized by very active $(Ca^{2+})_i$ signaling. Additionally, we observed a novel phenomenon where groups of cells display synchronized $(Ca^{2+})_i$ waves propagating within the ensemble based on their common activation. Cells in these clusters/ensembles appear to have a direction-biased cellular motility. We postulate that tumor cells from peripheral regions and belonging to active clusters represent the infiltrating component of the tumor. Finally, by means of *in utero* electroporation, we transfected a small population of glial precursors with the active mutant of Ras (HRasV12), GCaMP6s and a red reporter, that subsequently generates a spontaneous glioma model. Two photon imaging demonstrated that, within 10 days from the electroporation, the brain is gradually invaded by hypertrophic cells characterized by elevated motility and infiltrative potential. Similarly to the GL261 model, the infiltration is organized in cell streams endowed by very elevated $(Ca^{2+})_i$ activity.

Contents

Chapter 1

Introduction

Many years ago, brain cancers were diagnosed and treated based on how the cancer looked like under a microscope. Now, due to information and technology advancement, cancers are treated individually by looking into their intrinsic biology. Although our understanding of brain cancers has been increasing over the years, we are still far away from finding a cure.

Major obstacle in the study of brain cancers are the high-grade tumors such as *Glioblastoma multiforme* (GBM). Alterations in cellular signaling processes are being explored as a possible involvement in GBM growth. As such, calcium signaling has been proposed to be directly involved in GBM proliferation, progression and infiltration.

In this chapter, I will discuss about the role of calcium in GBM pathobiology.

1.1 Central nervous system tumor

The central nervous system (CNS) consists of the brain and spinal cord. An abnormal growth of cells growing from tissues within the brain or the spinal cord are classified as CNS tumor. A CNS tumor can either be benign or malignant. A tumor is said to be malignant when it has the potential to grow fast and invade nearby tissues, whereas a benign tumor means that it can grow but will not spread (1). The World Health Organization (WHO) published an update in 2016 to classify CNS tumors, for the first time combining molecular alterations together with histologic findings (2). CNS tumor grading were assessed using four morphological criteria: mitotic activity, microvascular proliferation, cytological atypia and necrosis. According to these criteria, CNS tumors are graded into low-grade (I-II) and high-grade (III-IV), where high-grade tumors are characterized by enhanced vascularization that sustains their fast progression (3).

1.2 Glioblastoma multiforme

Brain tumors can be categorized as primary originating from within the brain, or secondary that arise from metastasizing lesions outside the cranium. Gliomas account for more than 70% of all primary brain tumors and they arise from glial or neural precursor cells that includes astrocytomas, oligodendroglioma, ependymoma, oligoastrocytoma (mixed glioma), medullablastoma and optic nerve glioma (4). The most common and malignant type of glioma is the glioblastoma multiforme (GBM) which is a grade IV neoplasm with astrocytic differentiation and accounts for 48.3% of all primary brain tumors. Glioblastoma can develop both “de novo” or evolve from a previous astrocytoma. According to the recent statistical

report by the Central Brain Tumor Registry of the United States, pathological incidence of glioblastoma has been increasing over the years with a 5-year survival rate of 3.3% (5).

Glioblastoma has several distinct histological characteristics which includes nuclear atypia with multinucleated cells, high mitotic activity, irregularly shaped cells and high degree of differentiation. Furthermore, these tumors have enhanced microvascular growth with areas of necrosis that is surrounded by an accumulation of relatively long, loosely arranged cells often referred to as 'palisading' tumor cells (6). The aforementioned attributes of glioblastoma contribute to its high infiltration and invasion potential that leads to its poor prognosis.

The treatment of glioblastoma faces many challenges due to the presence of blood-brain barrier and the high malignancy of the tumor itself. Current treatment pipeline starts with maximum surgical resection of the tumor mass, if necessary, followed by radiotherapy and chemotherapy. Once diagnosed, maximal resection usually extends overall survival of the patient, but relapse is unavoidable due to the inability of the treatment to remove microscopic tumor cells that have invaded the brain parenchyma (7). In short, standard treatments are there to ease symptoms and prolong life but not to cure the disease.

1.2.1 A Hallmark of Glioblastoma: Infiltration

Infiltration has been identified as one of the hallmarks of GBM proliferation. GBM cells generally invade a few centimeters in radius away from the tumor mass into the brain tissue and in some cases, migrate into the contralateral hemisphere via the corpus callosum (8, 9). It is this characteristic of GBM that essentially causes recurrence and treatment resistance (10). Despite advances in understanding GBM invasion mechanisms, there is still lack of information relating to the speed, direction and intratumoral invasion dynamics (11). Therefore, understanding GBM invasion mechanism and coming up with targeted therapeutic strategy is critical.

Scherer, a German pathologist, for the first time in 1938 has attempted to describe routes of GBM invasion and the influence of preexisting brain structures on tumor evolution (12). He concluded that the GBM structure depends mainly on native brain tissues of the locality invaded rather than the GBM cells themselves. His observations provided key points in the modern molecular and histological diagnosis of GBM (13). Since then, the study of GBM has advanced particularly in the effort to characterize the tumor and gain comprehension of its mechanism. In these last few years, many of these researches are dedicated to finding possible therapeutic targets (7).

Nowadays, it is widely known that GBM infiltrate the brain along blood vessel in the perivascular space and into the brain parenchyma. This infiltration potential is highly supported by the presence of the tumor micro-environment (14). GBM microenvironment exists in constant contact with a heterogeneous surrounding consisting of oligodendrocytes, astrocytes, immune cells, malignant and non-malignant cells, glioma stem-like cells (GSCs)

and extracellular matrix (ECM) components (15, 16) (Figure 1.1). GBM cells establishes a symbiotic bi-directional relationship with these stromal cells to obtain tissue homeostasis favorable to supporting tumor growth via signaling pathways, gap junctions and microtubules along with secretion of growth factors, cytokines, chemokines and extracellular vesicles (17). Interestingly, alterations in signaling processes via ionic channels is an emerging concept in the study of GBM pathobiology.

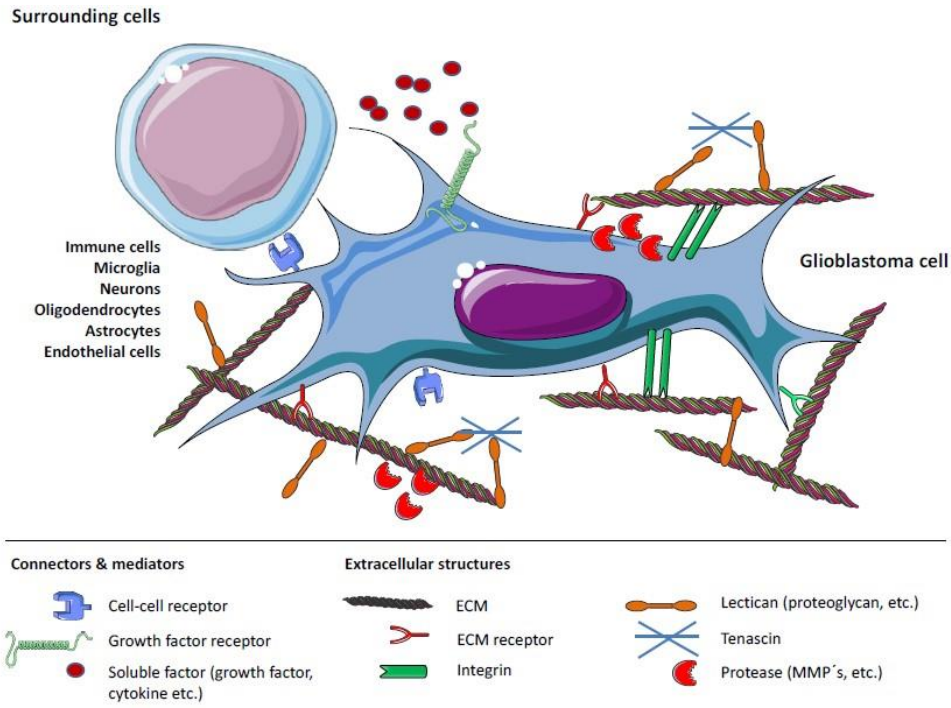

Figure 1.1: Mechanisms that promotes glioblastoma (GBM) cell invasion and migration. Continuous bi-directional communication between GBM cells with its heterogeneous microenvironment sustains its growth. Vital cytokines and growth factors are activated by neuroinflammation and are produced by these crosstalk, which supports tumor infiltration. Figure adapted from Vollmann et al. (16).

1.3 Communication in Glioblastoma

1.3.1 Ion channels

The initial study of the role of ion channels in cancer have been dated back to late 1980s and early 1990s (18, 19, 20). These findings encouraged significant interest in this field and unraveled its role in determining pathological features of cancer hallmarks (21). Transport of ions across the cell membrane is a fundamental process in maintaining normal cellular functions. Ion channels have specific roles in ensuring cell survival, i.e. through cell cycle checkpoints, cell death, proliferation capacity, migration and cell volume regulation (22, 23), 24). Altered regulation of ionic channels plays an important role in GBM cell survival and metastasis, and maybe it contributes to the progression of cellular fate from normal to neoplastic state (25). There are numerous signaling factors that activates GBM cells to affect

infiltration, motility and proliferation, thus further reinforcing the link between normal neurogenesis and tumorigenesis (26). Specifically, one such factor is calcium $(Ca^{2+})_i$ (27).

1.3.2 Calcium

Calcium is a ubiquitous secondary messenger participating in the regulation of various diverse cellular processes such as energy transduction, secretions, apoptosis, chemotaxis, synaptic vesicle fusion, muscle contraction and neuronal synaptic plasticity (28, 29, 30, 31). Intracellular calcium concentration, $(Ca^{2+})_i$, is maintained at ~100 nM because high concentration of Ca^{2+} ions are toxic to cells. In a standard solution, hydrated Ca^{2+} ions diffuse approximately 40 μM per second. However, in cells, due to the presence of other charged molecules and of numerous high affinity binding sites, diffusion of Ca^{2+} ions are much slower (32). In order to utilize Ca^{2+} as a second messenger, cells have devised an ingenious mechanism of signaling that has overcome the inherent problems associated with lower diffusion rates and cytotoxicity of $(Ca^{2+})_i$, by presenting changes in Ca^{2+} concentration as brief spikes which are often organized as regenerative waves (30, 32, 33).

To preserve normal cellular functions, cells need to maintain varied distribution of $(Ca^{2+})_i$ against chemical gradient between their intracellular (~100 nM free) and extracellular (~1.2 mM) Ca^{2+} concentration (30). Cells chelate, compartmentalize and remove Ca^{2+} ions to maintain this 20 000-fold gradient through regulation of energy driven Ca^{2+} pumps. In mammals the sarcoplasmic/endoplasmic reticulum Ca^{2+}-ATPase (SERCA), plasma membrane Ca^{2+}-ATPase(PMCA) and Golgi network secretory pathway Ca^{2+}/Mn^{2+}-ATPase (SPCA) are the main Ca^{2+} pumps (34, 35) (Figure 1.2).

1.3.3 Importance of Calcium Signaling in the Brain

Brain functions are carried at specific synapses through the release of neurotransmitters inducing a series of biochemical signaling events at the neuronal postsynaptic regions (36). Proper development of the nervous system is crucial to ensure that these functions are carried out efficiently. Ca^{2+} channels play an important role in regulating various nervous system developmental processes. Notably, short-term rise in $(Ca^{2+})_i$ levels, also known as $(Ca^{2+})_i$ transients, functions principally in mediating neuronal development stages such as migration, survival, growth, differentiation and network formation by maintaining rapid and transient influx patterns (37).

The influx and efflux of Ca^{2+} between intracellular compartments to plasma membranes in the brain triggers Ca^{2+} dependent signal transduction pathways. Pathways induced by the flow of Ca^{2+} include changes in gene expression, synaptic plasticity, neuronal excitability, release of neurotransmitters and memory storage (37, 38). This fundamental role of Ca^{2+} that controls synaptic activity and memory formation implicates key protein effectors, such

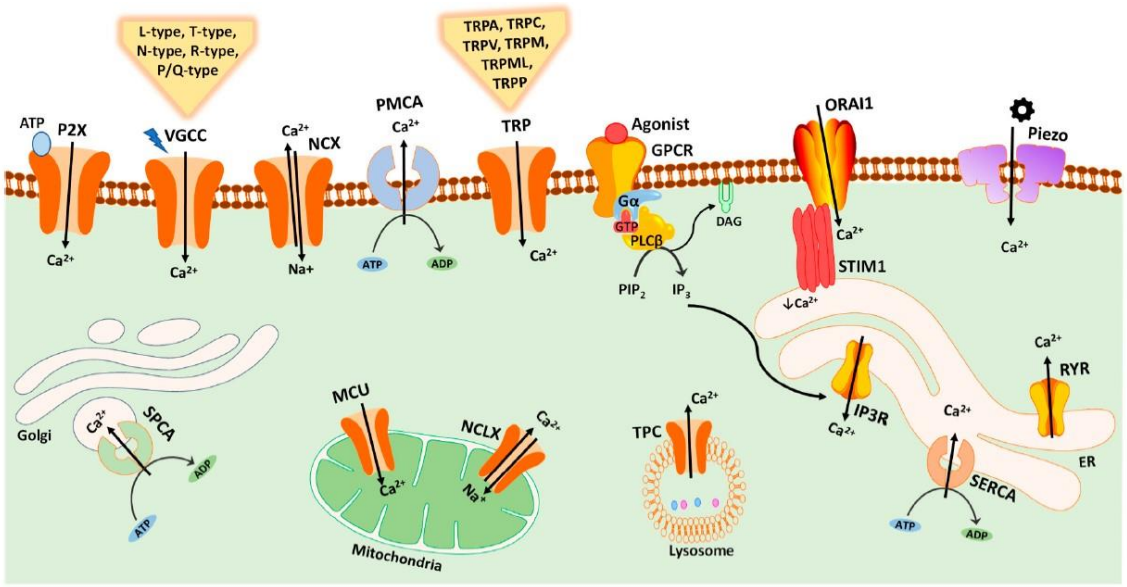

Figure 1.2: Schematic representation of major Ca^{2+} pumps, channels, exchangers and sensors of mammalian cells adapted from Maklad et al. (35). The main Ca^{2+} pumps such as SERCA, PMCA and SPCA helps to regulate $(Ca^{2+})_i$ distribution against chemical gradients, while the plasma membrane channels such as transient receptor potential (TRP) channels, voltage-gated calcium channels (VGCC), ligand-gated ionotropic P2X receptors, mechanosensitive Piezo channels and store-operated Ca^{2+} entry pathways mediated by stromal interaction molecule 1 (STIM 1) and ORAI1 regulates Ca^{2+} influx. Mitochondrial Ca^{2+} levels are maintained by mitochondrial calcium uniporter (MCU) complex and the mitochondrial Na^{+}/Ca^{2+} exchanger (NCLX). There are also the endoplasmic reticulum (ER) Ca^{2+} channels: ryanodine receptor (RYR) and inositol-1,4,5-triphosphate receptor (IP3R), and the two-pore channels (TPC) that regulates Ca^{2+} release from the endolysosomal system (35).

as calcium/calmodulin-regulated protein kinases (CaMKs), mitogen-activated protein kinases/extracellular signal-regulated kinases (MAPK/ERKs) and cAMP-responsive element binding protein (CREB) that is downstream of the mentioned pathways. In astrocytes, high density of IP_3 receptors are associated with Ca^{2+} release sites. The secondary messenger cAMP alters characteristics of IP_3 receptors upon phosphorylation by protein kinase A (PKA) leading to localized Ca^{2+} transients (39).

These diverse Ca^{2+}-mediated functions are the result of $(Ca^{2+})_i$ signaling in the form of waves that differs in their scale, temporal and spatial properties. Specific changes in the duration and distance traveled by $(Ca^{2+})_i$ signals results in distinct function modifications (39). Therefore, a properly controlled homeostasis of $(Ca^{2+})_i$ signaling is vital not only in supporting normal brain physiology but also protecting neuronal integrity and long-term cell survival (40).

1.3.4 Role of Calcium in Cancer

Over the last few years, many studies have been dedicated to elucidate the involvement of calcium in tumor biology and regulation of malignant characteristics in tumor cells (41). The human genome consists of an ensemble of 250 genes referred to as the 'calcium toolbox' that

codes for setting up specific $(Ca^{2+})_i$ signal in a given cell within a designated physiological state. Every cell expresses a subset of this calcium toolbox which is the signalosome proteins. When assembled, they form macromolecular complexes called calcisomes. Calcisomes encodes external information into $(Ca^{2+})_i$ signals and then decodes these signals to carry information into cellular events (42, 43). This process of $(Ca^{2+})_i$ signaling serves as 'calcium codes' differing in magnitude, time and frequency. Disturbance in $(Ca^{2+})_i$ pulses contribute to sustaining cancer malignancy (32, 35).

Morrone et al. reviewed recent findings and summarized main calcium channels that are involved in cancer cells, which are the voltage-gated Ca^{2+} channels (VGCC; L-type: $Ca_v1.1$-1.4; N-type: $Ca_v2.2$; T-type: $Ca_v3.1$-3.3; R-type: $Ca_v2.3$; and P/Q-type: $Ca_v2.1$), purinergic receptors, and the Ca^{2+} permeable ion channels of the transient receptor potential (TRP) family. These calcium channels are mainly involved in glioma progression, raising the possibility of their involvement in higher-grade gliomas such as GBM (44).

Additionally, Ca^{2+} signaling via connexin (Cx) channels have also been identified to be involved in a variety of diseases including cancers (45, 46, 47). Cx are found in almost every tissue and they form gap junctions that allow intercellular communication (48). These gap junctions are permeable to molecules smaller than 1.2 kDa, thus making it possible for secondary messengers such as Ca^{2+} to pass through. As such, they play a critical role in cellular differentiation, migration and survival (49, 50).

1.3.5 Alterations of Calcium in Glioblastoma

Among brain tumors, GBM is highly malignant, aggressive and lethal. Similar to other cancer cells, Ca^{2+} channels are involved in GBM infiltration, proliferation and enhanced migration (51). Major GBM-related Ca^{2+} channels are comprised of the T-type VGCC, calcium channel-associated TRP channels and ionotropic ATP-gated P2X7 receptor (44) (Figure 1.3). Likewise, Cx channels are also implicated in GBM Ca^{2+} signaling (52, 53).

1.3.5.1 T-type VGCC

Low-voltage activated T-type Ca^{2+} channels are key regulators of cell cycle and cell survival (54). Zhang et al. in 2012 demonstrated the first evidence of antitumor effect in U87 human GBM cells through direct inhibition of T-type Ca^{2+} channels (55). The knockdown of T-type subunits $Ca_v3.1$ and $Ca_v3.2$ in U251 and U87 GBM cells, disrupted protein kinase B (AKT) signaling and induced apoptosis (56). Then, the inhibition of only $Ca_v3.2$ in both GBM primary cell lines and mouse xenograph decreased expression of oncogenes and increased expression of tumor suppressor genes that slowed down GBM cell proliferation (57). More recently, Visa et al. showed that $Ca_v3.1$ can mediate chemotherapeutic resistance and that interfering with this pathway slows down GBM progression in a xenograph mouse model (58).

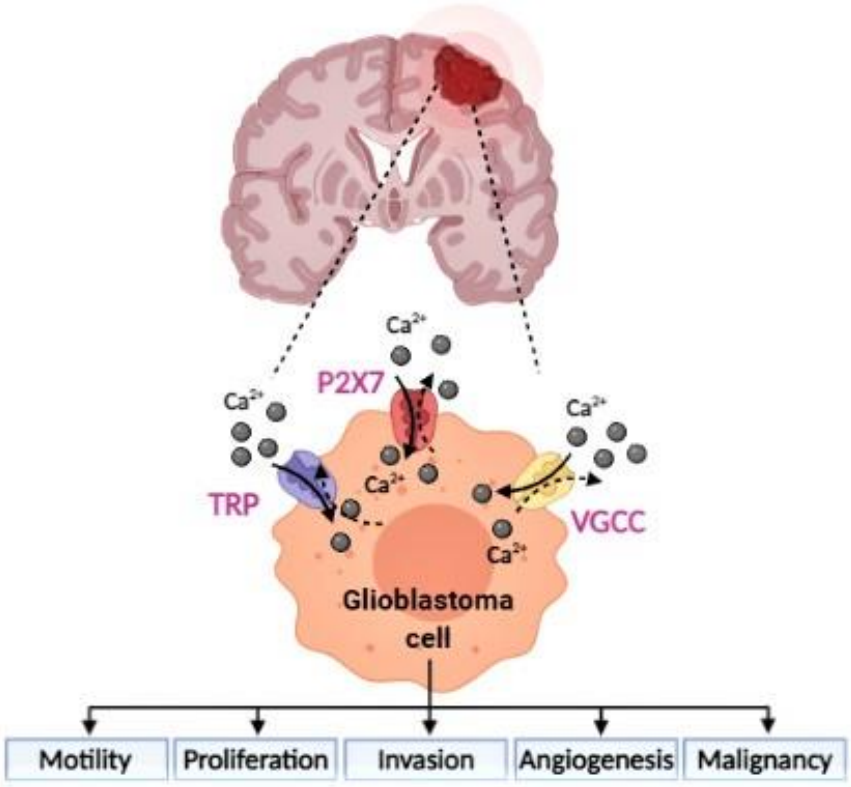

Figure 1.3: Altered regulation of calcium channels in Glioblastoma (GBM). Calcium homeostasis disruption could define malignant phenotype such as enhanced motility and proliferation, invasion, angiogenesis and malignancy in GBM cells. Figure created using BioRender.com

1.3.5.2 TRP channels

Members of the calcium channel-associated transient receptor potential (TRP) are known to be involved in a number of cellular functions, including tumorigenesis (59, 60). There are many studies documenting the role of TRP channels in glioblastoma progression. One of the earliest evidence was the activation of TRP-vanilloid 1 (TRPV1) by capsaicin that led to an influx of $(Ca^{2+})_i$ and caused apoptosis in U373 human GBM cells via p38 mitogen-activated protein kinases (MAPK) activation (61). It is also reported that the activation of TRPV1 by endovanilloids released by neural precursor cells (NPCs) reduced GBM expansion in a GL261 mouse model (62). In studies that involves TRPV2 channel, it appeared that TRPV2 activation potentiates chemosensitivity of temozolomide, carmustine and doxorubicin in U87MG cells and it negatively regulates GBM cell proliferation and survival (63, 64). It is also shown that TRPV2 enhances glioblastoma stem-like cells (GSCs) differentiation towards a mature glial phenotype suppressing their proliferation (65).

TRP-cation channel 1 (TRPC1) expression promotes proliferation and motility in GBM cells (66, 67). TRPC1, when stimulated with epidermal growth factor (EGF), relocates to the leading edge of migratory GBM cells (D54MG) suggesting its role in GBM migration (67). Moreover, TRPC1 plays an important role in glioma cell division due to its regulatory effect

on $(Ca^{2+})_i$ signaling during cytokinesis (66). Additionally, TRPC6 affects stability in human GBM cells under hypoxia by regulating metabolism of hypoxia-inducible factor 1-*alpha* (68).

Another TRP channel from melastatin-subfamily (TRPM) has shown to contribute to GBM progression. Mentol, an agonist of TRPM8, stimulates an increase in $(Ca^{2+})_i$ and enhances the migrational ability of GBM cells (69). On the other hand, inhibition of TRPM7 suppresses the capacity of GBM to proliferate, migrate and invade (70). Alptekin et al. established the involvement of TRP genes in GBM patients. They studied gene expression profile by qrt-PCR and found that TPRV1, TPRV2, TRPC1, TRPC6, TRPM2, TRPM3, TRPM7 and TRPM8 were overexpressed in GBM patients and was positively correlated with prolonged overall survival (71).

1.3.5.3 P2X7 Receptors

P2X7R is an ATP-gated cation permeable member of the purinergic ionotropic receptor family. P2X7R have attracted researchers over the years in the context of cancer (72). Activation of P2X7R promoted cell migration as well as pro-inflammatory factors in rat C6 glioma cells (73). Yet, in another study, when P2X7R is suppressed in C6 cells using an antagonist or short-hairpin RNA (shRNA), tumor growth and angiogenesis were promoted in *in vivo* rat model through EGF receptor signal pathway (74). It is clear that the role of P2X7R in cancer biology is still uncertain. Morrone et al. in their review stated two different hypothesis regarding the role of P2X7R in cancer. The first suggests that P2X7R works as an antitumor protein inducing cancer cell death, while the second proposes that P2X7R promotes cancer cell survival and invasiveness (44). However, there are studies that suggests P2X7R to be a predictor gene for glioma patient radiosensitivity and survival probability since the activation of P2X7R in radiosensitive M059J human GBM cells increased cell death (75, 76).

1.3.5.4 Connexin channels

Gap junctions are composed of two hemichannels (connexons) that connects the cytoplasm of neighboring cells. These channels are made up of transmembrane spanning Cx proteins (77). Unpaired connexons can function as normal plasma membrane channels, known as hemichannels (HCs), to provide a communication conduit between the cell cytoplasm and the extracellular environment (78). One of the most widely studied Cx is Cx43. It's role is consistently explored in GBM since it is largely expressed in astrocytes (52). Cotrina et al. demonstrated the requirement of Cx (Cx43 and Cx32) expression in purine-dependent Ca^{2+} signaling, thereby suggesting a possible target in conditions associated with abnormal astrocytic signaling (79). Studies have shown that as the malignancy of glioma increased, the expression of Cx43 reduces. (80, 81). However, in reality the expression of Cx43 is heterogeneous within the same tumor (52). Wang et al. in their review, have summarized that

inhibition of Cx43 expression of glioma cells at the periphery of the tumor mass, may be beneficial for surgical resection as it reduces the invasive capacity of the malignant cells (82). In the effort to fight cancer, researchers have found an approach in which they use antibodies (Ab) to target Cx HCs (78). For example, a monoclonal Ab (mAb) targeting an epitope in Cx43 via intravenous administration in C6 glioma-bearing rats has shown significant increase in overall lifespan and complete recovery without delayed relapses in 20% of the animals. This suggests a tumor-suppressing effect of antibodies can be related to inhibition of specific functions of Cx43 in glioma cells (83, 78). Recently, Sheng published a commentary article where he provided critical insights on research of peptidomimetics of Cx43 carboxyl terminus (Cx43-CT). The Cx43-CT is said to activate SRC proto-oncogene, non-receptor tyrosine kinase (c-SRC) in glioma stem cells (GSCs) (53). Pelez et al. found that TAT-Cx43, a Cx43 CT-mimetic peptide that inactivates c-SRC, decreases metabolic adaptability and plasticity in GSCs, preventing these malignant stem cells from surviving in nutrient-limiting circumstances (84, 85, 53). Additionally, different researchers have found Cx43 CT-mimetic peptide to suppress GSC's survival by suppressing its microtubule dynamics (86, 53).

1.3.6 Therapeutic Interventions Targeting Calcium Channels

The previous subsection discussed the alterations of several Ca^{2+} channels in the promotion of GBM progression. Many of these studies provided insights into finding potential combination of therapies for the treatment of GBM. Here, I review and outline some studies that are more translational and are being conducted in clinical trials. The progress from research to translational studies is very important because it helps to bring hope, treatment advances and often improved outcomes for GBM patients who responds poorly to current standard treatments. Table 1.1 summarizes clinical trials that are completed or ongoing, targeting Ca^{2+} transporting proteins on patients with different stages of GBM and their outcomes.

On the whole, these studies display great prospect in GBM therapeutic approaches and it is natural to predict an acceleration in the number future researches which would define the importance of Ca^{2+} signaling in GBM. However, it is noteworthy that the studies that are done so far aimed to block plasma membrane Ca^{2+} channels and not to use channel activators to induce overload of cytosolic Ca^{2+} and subsequent cell death.

Interventions	Channel/ Pump Targeted	Type/ Stages of glioma	Clinical Trial Phase	Study end year	Outcomes	NCT#	Ref
CAI + Radiation	Non-voltage sensitive channels	Newly diagnosed GBM	II	2010	CAI can be safely administered with cranial irradiation but there were no significant efficacy on patients	00004146	(69)
Mipsagargin	Serca pumps	Recurrent or pro-gressive GBM	II	2017	Acceptable tolerability and favorable pharmacokinetic profile	02067156	(70)
Mibefradil + Temozolomide	T-type channels	Recurrent Glioma	I	2017	Well tolerated and promising responses in patients	01480050	(71)
Mibefradil + Hypofractionated radiation	T-type channels	Recurrent Glioma	I	2017	Safe co administration with RT, effective brain penetration and promising response in a selection of patients	02202993	(70)
CTO + Temozolomide or chemoradiation	Non.voltage sensitive channels	GBM and other anaplastic gliomas	I	Ongoing	Acceptable safety profile, favorable brain penetration and promising response in difficult-to-treat patients	01107522	(72) (73)
Levetiracetam + Temozolomide + Chemotherapy	Partial bloackade of N-type currents	Newly diagnosed GBM	II	Ongoing	Survival benefits in patients	02815410	(74) (75)
ST101 channels	T-type channels	Recurrent or progressive GBM and other solid tumor	I-II	Ongoing	No results available as the study started recently on July 2020	04478279	(76)

CAI, Carboxyamidotriazole; CTO, Carboxyamidotriazole orotate

Table 1.1: Clinical trials for treatment of GBM. Modified and updated table adapted from Maklad et al. (35).

1.4 Intratumoral Heterogeneity of Glioblastoma

Intratumoral heterogeneity (ITH), especially in high-grade gliomas such as GBM, has been described as the biggest challenge of therapy resistance. Researchers are currently exploiting new imaging techniques to identify GBM regional heterogeneity and their underlying genetic and epigenetic characteristic to enhance understanding of this highly aggressive tumor (95, 96, 97, 98). Many GBM ITH studies have been focused on finding out genetic alteration, metabolic differences, molecular and cellular heterogeneity focusing mainly on the peritumoral tissue because its infiltrative capacity is reinforced by the environment surrounding the core of the tumor, as previously mentioned (99, 100, 101, 98). For instance, a study reported distinct GBM border morphology that exhibits different cellular dynamics. They identified two tumor border configurations with different invasive patterns: an invasive margin and a diffuse infiltration margin (102). Whereas in another recent study, cortical epileptogenesis in the peritumoral microenvironment was monitored during tumor infiltration using *in vivo* electrophysiology and calcium imaging. They disclosed early and late components of tumor-related epileptogenesis in an immunocompetent mouse model (103).

However, despite of many research advances of ITH in GBM, no studies have been done in understanding of the relationship between intratumoral calcium dynamics with GBM migrational pattern. As previously discussed in this chapter, it is evident that $(Ca^{2+})_i$ in many ways plays a crucial role in GBM migration and progression. Therefore, this thesis project has been dedicated to understanding intratumoral $(Ca^{2+})_i$ dynamics focusing in two tumor regions namely: the peripheral region and the tumor mass, and its role in GBM migrational pattern.

Chapter 2

Models, Techniques and Aims

In this chapter I will discuss briefly the currently available GBM models and *in vivo* imaging techniques that were used in this project. Finally, I will state the main aims of this project.

2.1 Experimental models in GBM

Gaining insights into the molecular and cellular pathways of GBM is fundamental to explore its pathobiology. Many experimental models have been created in order to be able to understand GBM. *In vitro* experimental models helps researchers to investigate simple mechanistic and specific functional insights but not recapitulate tumor behavior in a heterogeneous environment. Since rodents present similar genetic background, they can be used to closely mimic human GBM with all its associated complexity (104). Therefore, researchers need to balance this unavoidable differences in each model and select the best that fits their research question.

Presently, GBM mouse models are excellent for studying tumor initiation, progression, different routes of invasion, *in vivo* responses to therapy and intratumoral heterogeneity. There are 4 different types of GBM mouse models such as syngeneic/allograft models, xenograft models and genetically engineered mouse models (GEMMs) with germ-line mutation or somatic-mutation (105). In my project, I used one of most common allograft models, the GL261 mouse model, and then I developed a plasmid-based somatic-mutation model which can more accurately reproduce early developmental stages of human GBM.

2.1.1 Allograft and Xenograft Mouse Models

In an allograft model, implanted cancer cells are from the same species e.g. mouse tumor cells transplanted into an immunocompetent mouse. Whereas, in a xenograft model cells from a different species (e.g. human) are implanted into an immunocompromised mouse. These models are generated orthotopically into the brain with stereotactic surgery. Although they are widely used, these models do not recapitulate every aspect of human GBM. It is also important to note that in xenograft models, tumor-host immune response is inhibited, while neuroinflammation is an important component in GBM proliferative diffusion (106, 107, 108).

2.1.2 Genetically Engineered Mouse Models (GEMMs)

GEMMs are generated by introducing genetic abnormalities that are found in humans into mice through either somatic alterations or germ-line alterations. Germ-line modifications are

done using breeding strategies that generate animals carrying mutations in both oncogenes and tumor suppressors. However, some mutations are early lethal and therefore must be generated using approaches that are conditional such as the Cre-loxP recombination strategies (109, 110). Somatic mutations can be introduced using viral delivery or a plasmid-based approach. This method allows for gene expression in specific organs, cells types and at specific developmental stages. Popular approaches of viral delivery systems to induce GBM are the common retrovirus e.g. replication-competent avian sarcoma-leukosis (RCAS) viral vectors (111), adenovirus (112) and lentivirus (113). A limitation using viral delivery system is the maximum viral cargo limit and that the RCAS system needs specific mouse strains. More recently, plasmid-based approaches relying on CRISPR- and PiggyBac made it possible for multigene delivery with larger cargo sizes (114, 115, 116). Table 2.1 summarizes current animal models in the study of GBM.

Animal Models	Features		
		Advantages	Disadvantages
Transplantation	Allograph	Easy and fast; Immuno competent	Doesn't resemble human GBM
	Xenograph	Easy and fast	Immuno-compromised; Lacking appropriate brain environment
Genetically Engineered Mouse Models (GEMM)	Germ-line mutations	Early initiation events; resemble human GBM	Cant differentiate between primary and secondary mutation; Some mutations are early lethal
	Somatic mutations-Viral Vector	Controlled gene expression in target organs and cell type; Able to follow different developmental stages	Not suitable for multigene delivery; Clonal origin difficult to track
	Somatic mutations-Plasmid based	Same as viral vector; Multiple gene delivery; High efficiency for tumor formation	Invasive

Table 2.1: Advantages and Disadvantages of GBM Animal Models

2.2 *In vivo* Imaging Techniques

In neuroscience, microscopy is an essential tool to analyze cells and processes that occurs in the brain. Fluorescent microscopes offer us the ability to highlight individual cellular and subcellular structures and their local environment. In this project, the main experimental technique used is the two-photon microscopy.

2.2.1 Two-photon Microscopy

The theory of two-photon absorption was first mentioned by Dirac in 1927 but was fully developed by Goppert-Mayer in her dissertation in 1930 (117, 118, 119). However, it is not until 1990, that this theory was applied to a functional scanning microscope (120). Two-photon laser microscopy (TPLM) is based on the principle that if a fluorophore absorbs two photons simultaneously (within a time window shorter than 0.1 fs), the emitted fluorescence will be at a shorter wavelength of the excitation wavelength (Figure 2.1). This is achieved using a mode-locked laser, in which photons are emitted at a frequency of 80 MHz, where the intensity of light emitted is high for short bursts of time. The likelihood of near simultaneous absorption events increases with the squared intensity of the laser (121). This turns out to be a nice property of two photon excitation, because it gives rise to a localized excitation. The probability of excited fluorophore rapidly decays moving away from the focal plane, therefore, we can collect all the available photons coming from our samples without a pinhole. This phenomenon is an important part of the detection system (122).

TPLM uses the long wavelength near infrared light (IR) as source of photons. This allows us to penetrate deeper into tissue with high scattering like the brain. Owing to the restricted excitation at the focal point, photobleaching and phototoxicity are reduced, making TPLM very useful for observation of cells in living brain tissues in whole animals, in which a depth of hundreds of micrometers can be reached (123). Figure 2.2 illustrates the TPLM setup in our lab.

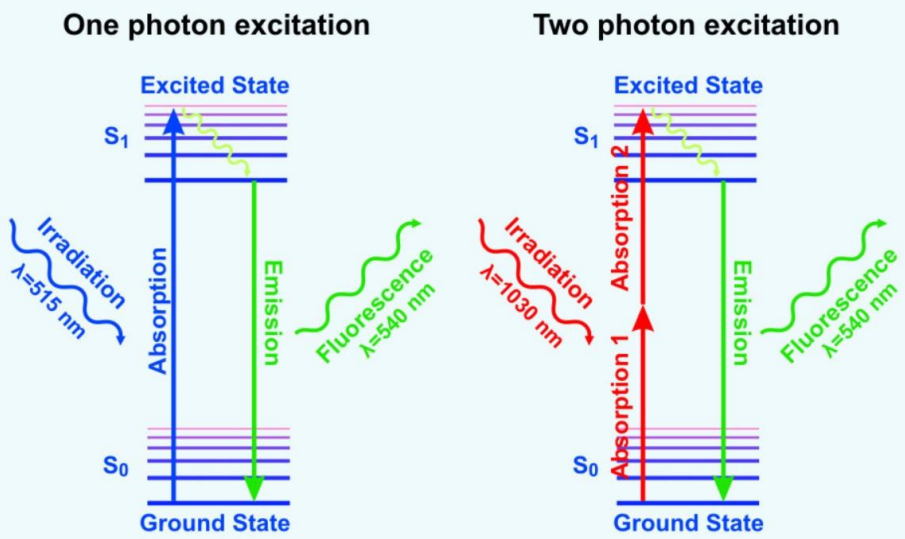

Figure 2.1: Simplified Perrin-Jablonski diagram for 1-photon and 2-photon excitation. The final fluorescent emission is the same for the two different modalities of excitation. Image adapted from (124).

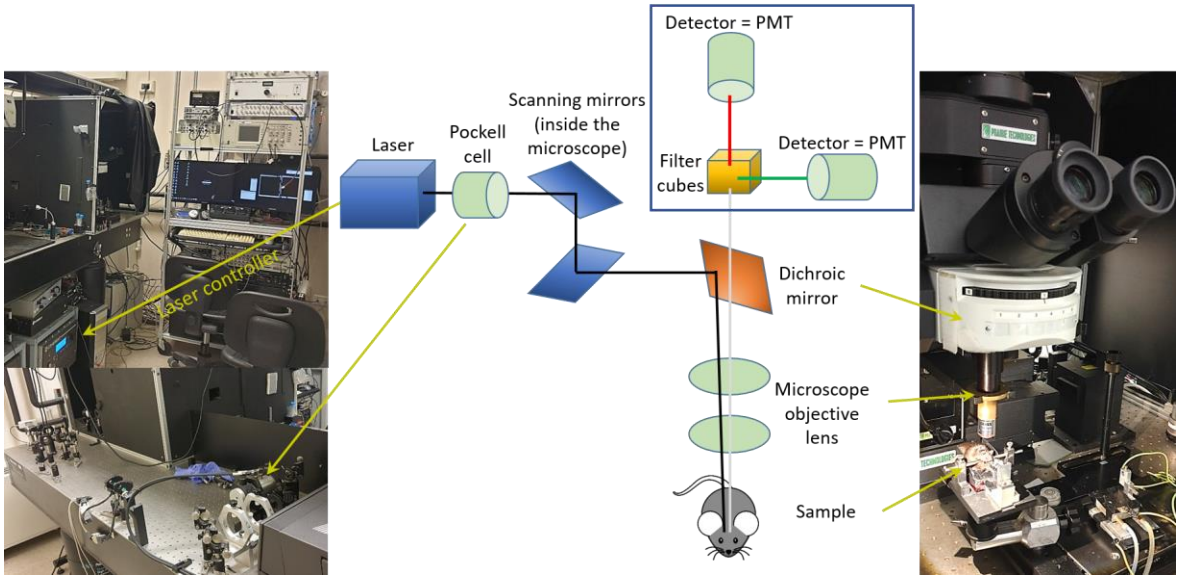

Figure 2.2: Diagram of a two-photon microscope. Image in the middle represents a schematic diagram of the two-photon setup while images on the right and left are pictures of the setup in our lab.

2.2.2 Wide-field Fluorescence Microscopy

Recently, our lab implemented wide-field (WF) imaging technique via a custom-made setup for imaging at a mesoscale level (Figure 2.3). This methodology allows us to map activity of large areas of the brain in resting conditions or under execution of specific tasks in anesthetized or behaving mice (e.g. in response to visual stimuli). Compared to two-photon microscopy that catches brain activity at single-cell level, WF microscopy is capable of recording cellular activity across one or multiple regions of the brain with high temporal resolution. This technique is used in this project to visualize global Ca^{2+} activity in GBM mouse model.

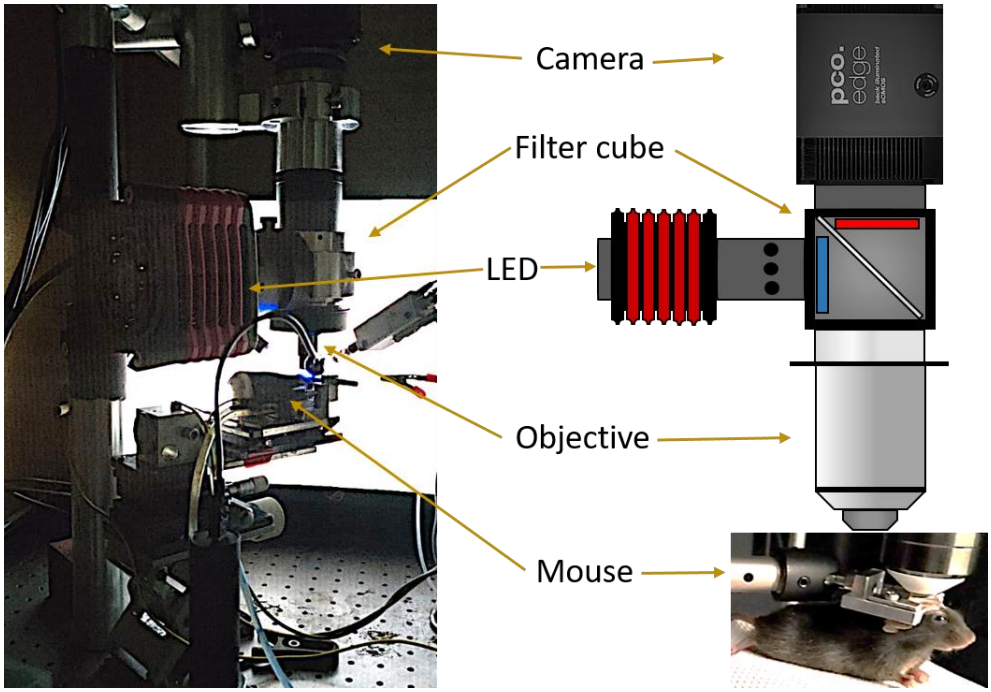

Figure 2.3: Custom made Wide-field microscope for *in vivo* **imaging.** Image on the right represents a schematic diagram of our wide-field setup while the image on the left is a picture of the actual setup.

In WF imaging, all areas of the mouse brain under the microscope are simultaneously exposed to the light source, unlike confocal imaging where light comes from a laser source that is focused to scan point-by-point the whole sample. We used a high-brightness light emitting diode (LED) as light source for WF fluorescence microscopy.

2.3 Aims

Finally, to conclude this chapter, the following are my research aims:

1. To study tumor invasion and progression in GBM animal models.
2. To show the importance of intravital 2-photon imaging as a technique that allows the identification of different tumor regions.
3. To analyze intratumoral calcium signaling patterns and its role in tumor migration.
4. To generate a GBM mouse model that closely resembles the human pathology using current molecular techniques.

Chapter 3

GL261-Model

Here I will describe the GBM mouse model used, the experimental methods and the obtained data. This study not only shed light on the importance of understanding the correlation of intratumoral Ca^{2+} dynamics and tumor migration, but it is also, to my knowledge, the first to make a quantitative analysis of *in vivo* intratumoral $(Ca^{2+})_i$ heterogeneity.

3.1 Introduction

The most frequently used murine GBM model is the transplant of GL261 cells. GL261 is an allograph immunogenic model with its cell line being established in mid 1990s. It was originally produced by intracranial injection of 3-methylcholantrene in C57BL/6 mice and consequently maintained by implanting pieces of tumor into the syngeneic mouse strain. Tumor pieces was placed serially through subcutaneous and intracranial implantation (125). Seeing that no detailed description of GL261 tumor model was available, Szatmari et al. published a paper in 2006 describing some *in vivo* characteristics of this tumor model. They found that GL261 tumors are highly aggressive with 100% mortality rate within 70 days after transplanting 100 tumor cells. This data was supported by Plautz et al., Natusume et al. and Glick et al. whereby they observed that the animals were all killed within 21 days post injection of 1-4 x 10^5 GL261 cells (108, 126, 127, 128).

Most importantly, Szatmari et al. reported that GL261 cells carry K-ras and p53 point mutation. K-ras mutations are frequently observed in human GBM tumors but present with lower frequency in other human brain tumor types (129). The p53 gene is a tumor suppressor gene and its mutation is very common in human brain tumors that correlates to poor prognosis (130, 131). However, they discovered that GL261 is a moderately immunogenic model because it has an elevated basal major histocompatibility complex (MHC1) expression that codes for cell surface proteins essential for the adaptive immune system. Although it presents this limitation, it can be still used for immunotherapy and gene therapy by carefully evaluating the obtained data (108).

Since GL261 model harbors main characteristics of human GBM tumors and exhibits invasive but non-metastatic growth pattern, it is a model of choice in this study. GL261 model fits the main purpose of this study, that is to investigate intratumoral Ca^{2+} dynamics and its correlation with migration/invasion properties. The easy and quick process to produce GL261 model is an added advantage that contributed to the selection of this model.

The development of intravital two-photon microscopy has opened vast opportunities to observe and visualize cellular processes at a single-cell resolution. Time-lapse imaging has provided valuable information on GBM cellular dynamics. In this study, I will begin by describing the development and characterization of our fluorescent GL261 mouse model that expresses a genetically encoded calcium sensor (GCaMP6s). Consecutively, by exploiting two photon microscopy, *in vivo* $(Ca^{2+})_i$ dynamics of distinct tumor regions are investigated and analysed. Then, I will further demonstrate a strong correlation between $(Ca^{2+})_i$ activity and GBM cells' invasive migratory patterns. Finally, an observed novel phenomenon of $(Ca^{2+})_i$ signaling in GBM tumor cells is reported and I auspicate that the underlying biochemical mechanisms could represent a potential new therapeutic target.

3.2 Results

3.2.1 GL261 model, *in vitro* and *in vivo* validation

We started the study by generating a plasmid construct with a calcium sensor, GCaMP6s and a red fluorescent protein (RFP), DsRed2, which is modified with the actin-staining peptide, LifeAct as shown in Figure 3.1A. This plasmid allows for the expression of the calcium sensor as well as RFP that stains the actin cytoskeleton of the cells. The general idea is to be able to evaluate intracellular calcium, $(Ca^{2+})_i$, as well as outline cellular morphology. Figure 3.1B and Figure 3.1C illustrates the experimental pipeline, where GL261 wild-type (GL261-WT) cells were transfected with the plasmid construct using cell electroporation technique and the transfected cell line (GL261-TF) was then injected intracranially into the visual cortex of adult C57BL/6 mice. The injected mice were imaged using two-photon microscopy. Figure 3.1D shows a mosaic image of an entire tumor area that was imaged 8 days post implantation. Tumor cells can be seen in red, and in green are the collagen fibers that could be viewed due second harmonic generation (SHG). SHG is a nonlinear optical process where two photons of the same frequency interact with a nonlinear material and produce a frequency-doubled photon (132). SHG can be produced by non-centrosymmetric structures such as collagen fibers that possess a highly crystalline triple-helix structure (133). The dark area in the middle marks the injection area. The tumor grew around the injection area in an ellipsoid shape.

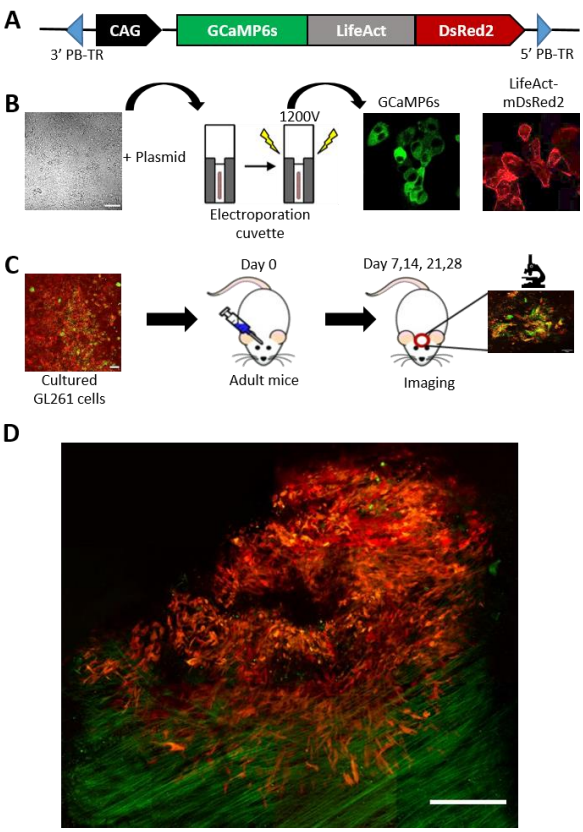

Figure 3.1: GL261 mouse model. **A)** pSP72 plasmid construct with CAG promoter expressing genetically encoded calcium indicator GCaMP6s (green) and LifeAct-DsRed2 (red), staining the actin cytoskeleton. **B)** Cell electroporation in culture. GL261 wild-type cells were transfected with plasmid construct in **A)** and generated a stably transfected GL261-GCaMP6s-LifeActDsRed2, fluorescent cell line (GL261TF) **C)** 2 µL of GL261-TF cells at concentration 2 x 10^4 cells/µL were injected into the cortex of adult mice (P90-150) and the resulting tumor-bearing mice were imaged using two photon microscopy. **D)** Mosaic image showing entire tumor area 8 days' post implantation. Maximum projection of a stack imaged every 5 µm from the surface down to about 250 µm depth (scale bar 100 µm). The green fluorescent signal represents collagen fibers as a result of SHG (133).

Cellular transfection is a process where foreign DNA is introduced into cells by non-viral methods, in this case, by cell electroporation technique. Thus, it is important to ensure that the transfected cells retain its original phenotypic characteristics. To validate our fluorescent cell line, we performed a number of *in vitro* assays. First, we evaluated the proliferation capacity of both GL261-WT and GL261-TF using an automated cell counting chamber. A known number of cells (i.e. 1 x 10^4 cells) was seeded on P60 cell culture plates and the number of cells were counted every 24 hours as shown in Figure 3.2A. We found no statistical difference in their proliferation capacity. However, we observed morphological differences in these two cell lines. Therefore, we measured the morphology of the cells using a common shape factor, which is the aspect ratio, a function of the largest diameter and the smallest diameter orthogonal to it (Figure 3.2B). Our result shows that the GL261-WT cells harbors a more elongated shape. We reasoned that since the cell lines exhibit distinct morphological difference, we should see a difference in their *in vitro* migrational capacity. It is important to keep in mind that cell shape plays a pivotal role in migration behavior. The shape of cells, regulate traction forces at the cell front and rear. Indeed, Figure 3.2C and Figure 3.2D shows that GL261-TF cell line exhibit a reduced *in vitro* migrational capacity. The wound healing assay shows that the GL261-WT cells achieved 100% closure within 48 hours while GL261-TF cells achieved 48% closure. The display of different *in vitro* phenotype of both cell lines could be due to the fact that, the GL261-TF line underwent a sorting procedure to obtain 100%

fluorescent cells after transfection. This means that only a sub-population of cells are harvested and maintained.

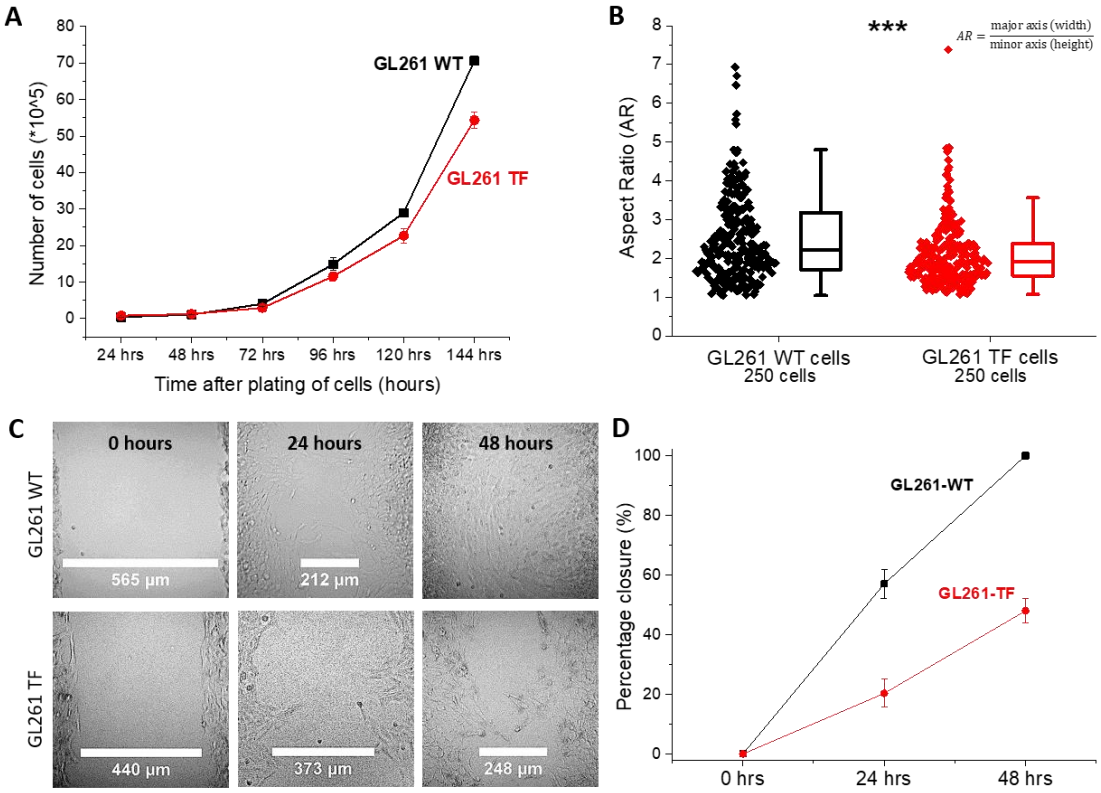

Figure 3.2: *In vitro* **validation of GL261-WT vs GL261-TF**. **A)** Cell proliferation measurement using an automated cell counting chamber. Cells were seeded at a known density (i.e. 1 x 10^4 cells) and measured for 6 days consecutively. There is no significant difference between GL261-WT and GL261-TF cells (n=4 repetitions) (p = 0.149, two-way Anova). Standard deviation is within the sample size. **B)** *In vitro* cell morphology measured by evaluating the ratio of cell width to its height. The shape description analysis was done on 3 culture plates each. GL261-WT appear to have significantly larger aspect ratio (p = 0.00004, two-sided Mann Whitney test) compared to the fluorescent GL261 cell line, showing that the wild-type cells have a more elongated morphology. **C)** Image-based monitoring of wound healing on GL261 cell lines. The assay was done on cells that were seeded into the wells of the culture insert that was placed on a 35mm tissue culture plate and imaged at different time points. Imaging was performed over 48 hours using phase contrast (calibration bar 100 µm) (n=3 plates/each). **D)** Quantified rate of wound closure over time. GL261-WT exhibited a faster rate of closure.

To address the underlying differences in *in vitro* cell migration and to ensure aggressiveness of the tumor produced by the transfected cell line, we next examined the overall survival of mice bearing either tumor cell lines. We implanted 4 x 10^4 cells/2µL of GL261-WT or GL261-TF, into the brains of C57BL/6 mice. Survival of animals were evaluated by euthanizing them when they have a 20% reduction of their original weight. The survival rates were assessed using the Kaplan-Meier method (Figure 3.3A). We found that both cell lines are indeed aggressive with no significant difference between the two groups (n=6/group). This survival data is in line with the study done by Perez et al. where the median

survival of GL261-bearing mice was 39 days (134). We then measured the *in vivo* tumor volume of mice implanted with GL261-TF cells to have an approximation on tumor growth rate. Since our experiments are done chronically, we measured tumor volume using subcutaneous volume estimate. To evaluate tumor volume, first the shape of the tumor has to be assumed. Here, we calculated the volume assuming an ellipsoid shape since GL261 tumor grows in an ellipsoid manner as observed in Figure 3.1D. As suspected, by the 4th week post implantation, the tumor volume is quite large (Figure 3.3B). The results obtained supports the reliability of our fluorescent mouse model as an aggressive and a fast growing tumor model. It was critical to validated our fluorescent mouse model to ensure its *in vivo* properties did not differ from the largely used GL261-WT model and to support our working hypothesis that is to evaluated the intratumoral heterogeneity of $(Ca^{2+})_i$ activity in an aggressive GBM model.

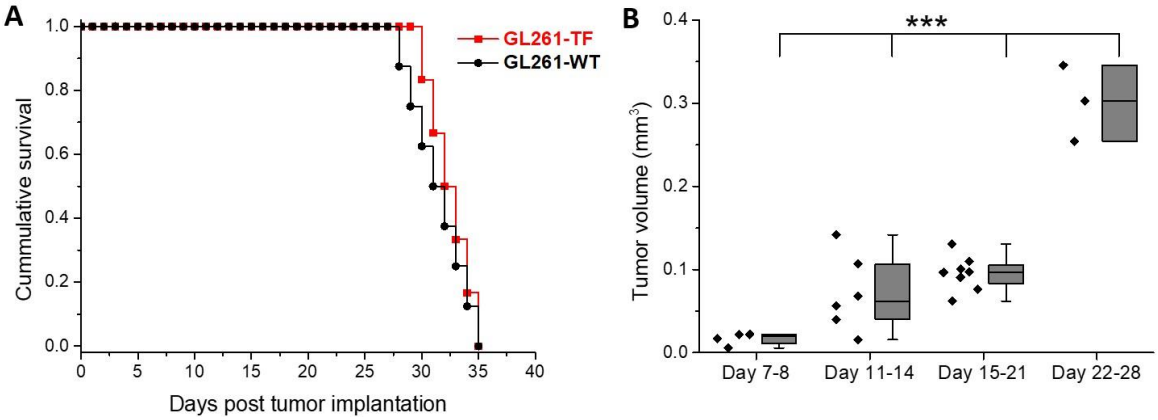

Figure 3.3: GL261 fluorescent model as an aggressive tumor model. **A)** Kaplan-Meier survival curve of wild-type and transfected GL261 bearing mice (n=6 mice/group). No significant differences were observed between the two groups (p>0.05, Mann-Whitney test) **B)** Tumor growth rate of GL261-TF implanted mice. A total of 11 mice were used to estimate tumor volume, where some mice were chronically imaged at different time windows. P value determined by Mann-Whitney test, ***p<0.001.

3.2.2 Exploiting two photon microscopy: Insights from a fluorescent tumor model

The attack to the GBM invasive margin is the key problem researchers are trying to elucidate in order to provide possible treatment strategies for GBM patients (135, 102). The GL261 tumor model has been shown to closely recapitulate many characteristics of the human pathology (136). However, contradictory observations and ideas have been reported on the *in vivo* growth of this tumor model. While many studies have shown that the GL261 tumor grows with an irregularly shaped borders accompanied by individual cells protruding few millimeters away from the tumor margin (137, 138, 139), some researchers have described GL261 tumors as nodular tumor with a large solid mass and low degree of infiltration (140, 141).

On that account, here we report that the *in vivo* GL261 tumor, albeit growing in an ellipsoid shape, it consists of a primary mass and protruding cell streams that detaches itself from the

mass migrating into the brain tissue. We identified these two tumor regions, as the peripheral region/invading front and the tumor core, using chronic *in vivo* two photon imaging. Figure 3.4A and Figure 3.4B shows a coronal section of GL261-TF tumor 7 days after tumor graft. The fluorescent tumor cells were injected into the mouse occipital cortex. It is evident that the tumor displays two distinct territories characterized by different morphology of component cells. Cells at the center of the core are characterized by spherical shape and they are densely packed, while cells at the peripheral region are more dispersed and elongated in shape. We then quantified the *in vivo* morphological difference and used the aspect ratio as a shape descriptor parameter as previously mentioned (n=9 mice). Figure 3.4C clearly shows variation in the morphological phenotype of the component cells in both analysed regions.

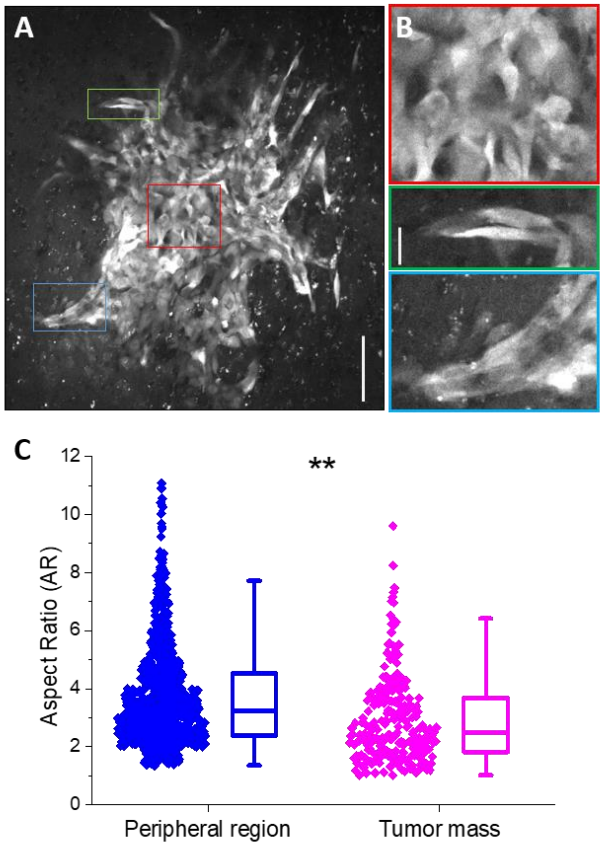

Figure 3.4: *In vivo* **two photon imaging of glioblastoma tumor in a GL261-TF mouse model**. **A)** and **B)** Maximum projection of z-stack images seven days after tumor graft (100 µm depth and 2 µm step size, calibration bar 100 µm). GL261-TF cell were injected into the mouse occipital cortex and within a week, the tumor became visible through a window applied on the transplanted site. The tumor shows two different territories characterized by a different morphology of the component cells. Near the center, cell density is very high, and the spheroidal cells appear to have substituted the original cell population (see red inset). Near the edges of the tumor cells are very elongated and they are arranged in linear chains (green and blue insets, calibration bar 20 µm). **C)** Global aspect ratio measurement of *in vivo* tumor morphology at two different regions, computed as in Figure 3.2B and at different time points during chronic imaging. Statistical significance determined by Mann-Whitney test (**p<0.01) (n=9 mice; 788 cells in peripheral region and 247 cells in tumor mass).

In vivo time-lapse imaging technique demonstrates that the GL261 model possess an infiltrative component. Figure 3.5A display GL261-TF cells migrating along the direction indicated by the arrow. Two images were acquired within a short time frame of 90 minutes' with the first image displayed in red and the second in green. Thus, when these images are superimposed, the cells are seen in yellow. The fluorescence plot on the right, clearly indicates the migration direction of the upper cell. The cell appears to advance towards the left pole. Figure 3.5B and 3.5C shows chronic acquisition of tumor cell migration with a longer temporal

scale, i.e. 24 hours. These cells were acquired at 50 µm depth from the cortical surface. We were able to recognize the acquisition area and we aligned the fields by using collagen fibers as a reference. The cells seem to collectively migrate towards the left suggesting possible communication between small groups of cells.

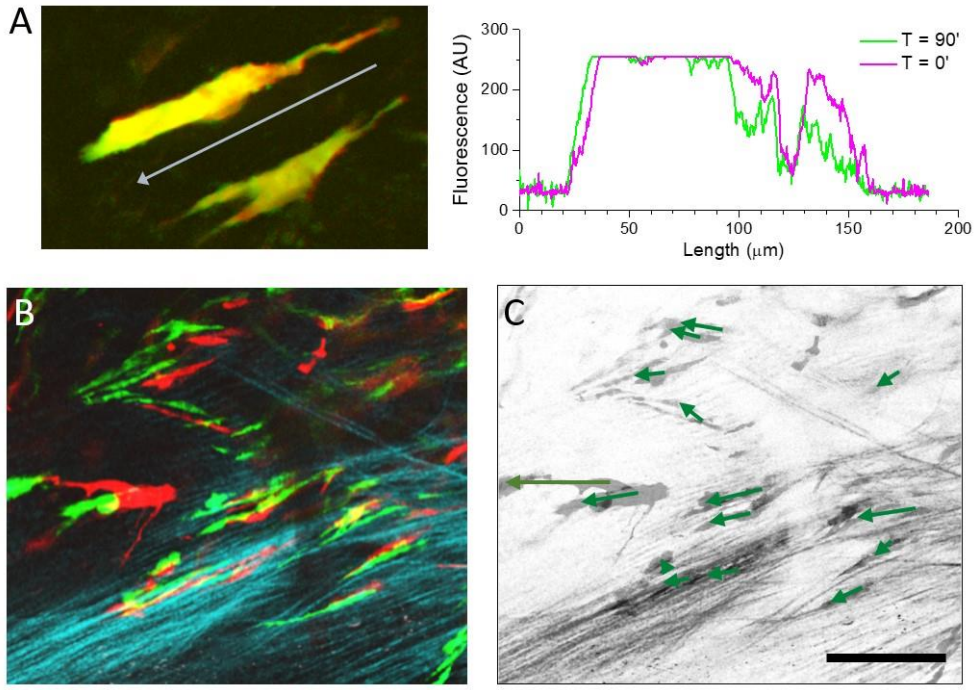

Figure 3.5: Stably transfected GL261-TF cells in the mouse cortex A) Acute *in vivo* time lapse imaging showing the migration of tumor cells. Two images were acquired at 90 min of distance with the first image displayed in red. Both cells are migrating in the direction indicated by the arrow. The plot shows the profile of the fluorescence along the direction of motion of the upper cells. The distribution of fluorescence reveals that the cell is advancing with its left pole and retracting on the right edge. **B)** Chronic imaging of a migrating cell stream *in vivo*. Two images of the same field have been collected 8 and 9 days after tumor implant (red and green respectively) at about 50 µm from the brain surface. The blue signal originates due to SHG from extracellular collagen fibers. The structure of the collagen fibers has been used to align the time lapse images. **C)** The center of gravity of all cells identifiable in the two images have been connected by the arrows that indicate the motion of the cell stream (calibration bar 100 µm).

3.2.3 Global *in vivo* calcium events in the GL261 fluorescent tumor model

Next, to evaluate cellular communication in the developing GL261-TF tumor, we characterized the global $(Ca^{2+})_i$ activity of tumor cells regardless of the position of the cells at different days. Figure 3.6A illustrates a graphical scheme of example tumor volumes at 4 time points post tumor implantation. *In vivo* calcium imaging was done at 4 time windows after tumor implantation: 7-8 days, 11-14 days, 15-21 days and 22-28 days. The earliest imaging was done one week after implantation to allow malignant cells to expand in the neocortex forming small-sized colonies of tumor cells. These time ranges were chosen to fit the approximate progression of tumor growth as it is variable from animal to animal. Contribution to this variability could be due to the tumor implantation technique, where there

might be a spill-over of cells caused by positive pressure exerted during intracortical injection procedure. Another possible contributing factor could be the tumor pathobiology itself, allowing different growth rates in each individual animals. We quantified the duration and frequency of $(Ca^{2+})_i$ events as shown in Figure 3.6B and Figure 3.6C, respectively, using custom made Matlab code. The computation of these parameters are explained in Methods Section 3.4.12. Our data suggests that the average duration of global $(Ca^{2+})_i$ events is significantly different only during the initial tumor development stage (1st week post implantation). Whereas, the frequency of $(Ca^{2+})_i$ events is significantly different during the 1st and 2nd week of tumor growth compared to the 3rd and 4th week. This might suggest a possible involvement of $(Ca^{2+})_i$ signaling in tumor growth where tumor cells tend to exhibit higher $(Ca^{2+})_i$ activity during early developmental stages to initiate crosstalk between malignant cells for rapid growth. However, we have seen that the GL261-TF tumor possesses distinct morphological features of component cells located at different regions (i.e. the peripheral region and tumor mass). Example Ca^{2+} traces of cells located in these two regions are shown in Figure 3.6D. Therefore, the reported global $(Ca^{2+})_i$ events represents contribution from these two distinct population of cells, that will be analysed separately henceforth.

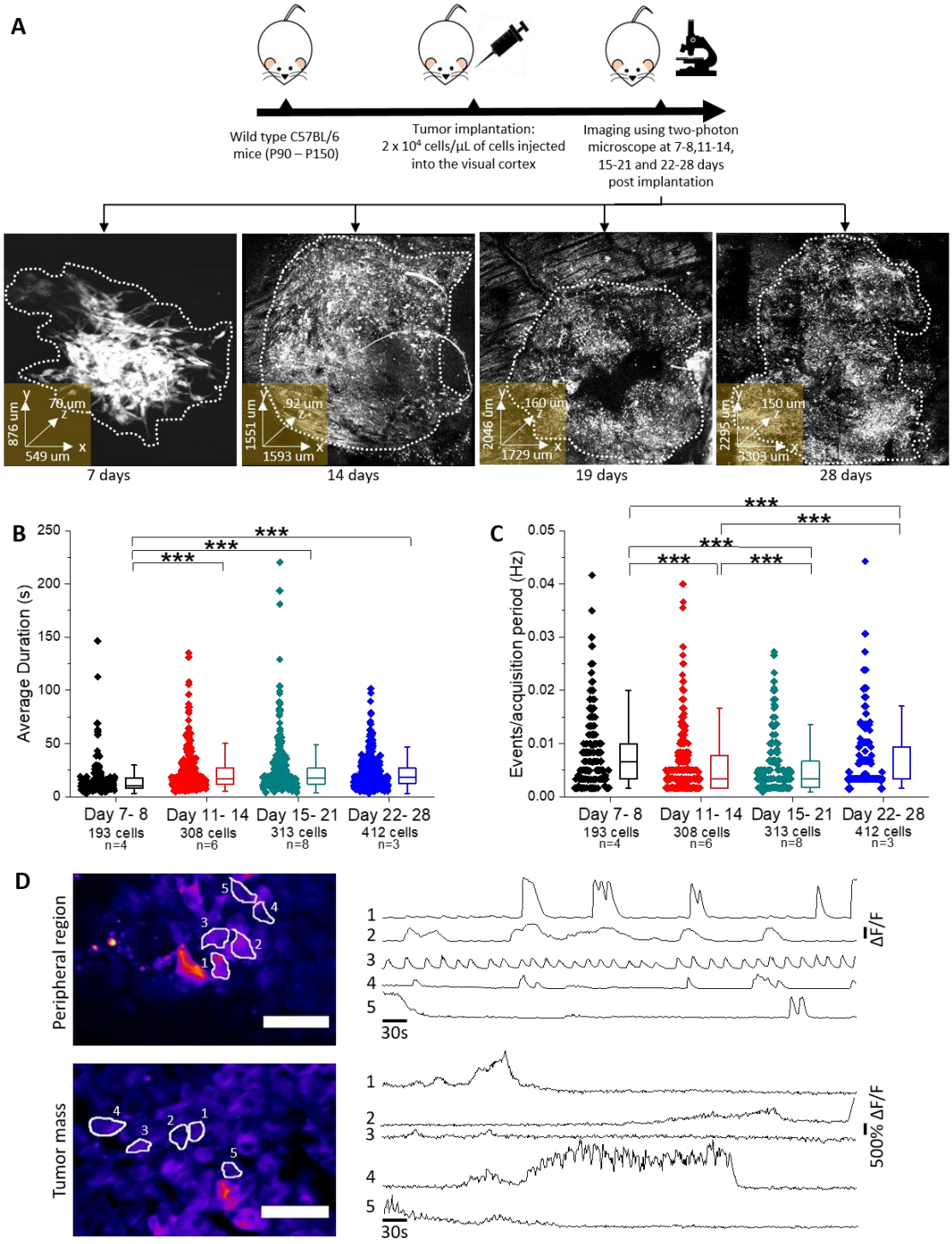

Figure 3.6: Quantification of global *in vivo* calcium events of GL261-TF tumor cells up to 4 weeks post implantation. A) Graphical scheme representing tumor implantation protocol and mosaic images of approximated tumor size at 7, 14, 19 and 28 days post GL261-TF cell injection. Maximum projection of z-stack images collected along the extension in depth of the tumor is represented for different time point during chronic acquisition. The values of x, y and z axis represented on each image are in µm. **B)** and **C)** Plots representing mean duration and frequency of $(Ca^{2+})_i$ events, respectively, as a function of time (days post injection). Data shows that during the initial stages of tumor development, i.e. 1 week post implantation, the tumor cells exhibit shorter duration and higher frequency of $(Ca^{2+})_i$ events. **D)** Example Ca^{2+} traces of cells located at two different regions of the tumor. Images are an average projection of a 10 minutes' movie sequence with sampling period of 1.07s (scale bar 50 µm). Peripheral region was imaged at 100 µm from the surface of a tumor 14 days post implantation while tumor mass was imaged at 230 µm from the surface of a tumor 20 days post implantation. Statistical significance

determined by Kolmogorov-Smirnov test (***p<0.001; n=9 mice, where some mice were chronically imaged at different time points).

3.2.4 *In vivo* calcium dynamics at distinct tumor regions

Next, we focused on characterizing the $(Ca^{2+})_i$ dynamics of tumor cells in two different regions: core and periphery. The $(Ca^{2+})_i$ activity of cells in these two regions were distinguished from the previously obtained global $(Ca^{2+})_i$ activity. Since the aspect ratio of the tumor cells were significantly distinct in these two regions, we expect to observe different pattern of (Ca2+)i oscillations. Figure 3.7A shows representative images of what constitutes as the peripheral region and tumor mass. Cells located at the edges/border of the tumor, where the location is in close proximity with the host brain tissue, are referred to as the peripheral region and cell located at the dense core, i.e. center of the tumor, are referred to as tumor mass. Identification of the edges of the tumor is a rather qualitative matter and there is no published work that has defined uniformly the borders of a tumor. Here we defined the edge of the tumor as the contour that encloses all cells that we can certainly define of tumor origin, on the basis of size, fluorescence and morphology. The green signal comes from the calcium sensor, GCaMP6s and the red signal comes from actin DsRed2. We calculated the percentage of active cells in both regions by counting the number of cells that exhibits $(Ca^{2+})_i$ fluctuations divided by the total number of cells in the region of acquisition (Figure 3.7B). We found that, the peripheral region hosts a higher percentage of active cells than the tumor mass. Besides, when we quantified the $(Ca^{2+})_i$ activity of cells in both the regions, $(Ca^{2+})_i$ events at the periphery are shorter in duration and higher in frequency. Based on the obtained data, we hypothesize that cells at the invading front of the tumor have higher active $(Ca^{2+})_i$ activity that prompts infiltrative phenotype of the component cells.

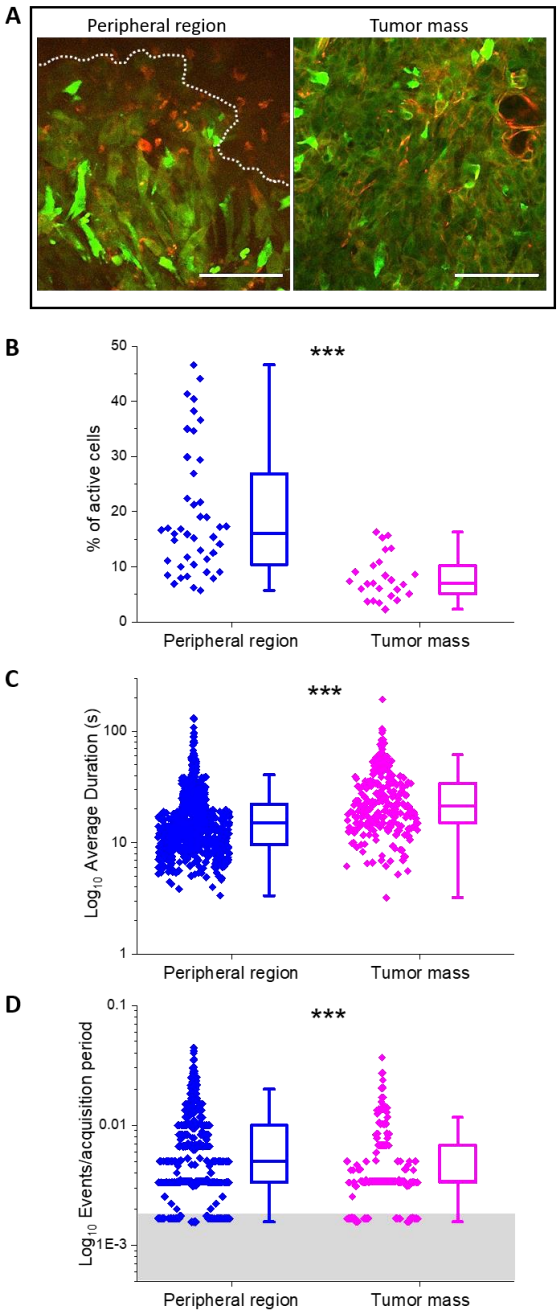

Figure 3.7: ***In vivo*** **calcium dynamics during chronic imaging up to four weeks post implantation is higher in the periphery respect to the tumor mass. A)** Representative images of two tumor regions of interest in which it is evident the difference between a peripheral region and the tumor mass (in green GCaMP6s signal, while in red LifeAct-DsRed2 marking actin cytoskeleton). Images are an average projection of a 10 minutes' movie sequence with 1.07s sampling period. The field width is about 305 µm and the calibration bar is 100 µm. Image at the peripheral region was taken 12 days post tumor implantation at 50 µm depth from the surface while image at tumor mass was taken 18 days post tumor implantation at 90 µm depth from the surface. Tumor border is indicated by the white dashed line. The red-stained cell bodies located beyond the white dashed line are likely to be microglia cells activated by the inflammatory response caused to the tumor. Microglia cells are considerably smaller and more spherical in shape than the GL261 cells. The red fluorescence emitted by the microglia is caused by phagocytosis which occurs as part of the inflammatory response in which microglia digests the fluorescently tagged-tumor cells. **B)** Quantification of percentage of active cells at both tumor regions. Active cells are calculated by counting cells that exhibits calcium fluctuation over the total number of cells in the acquisition field. This parameter was measured over 43 fields at the peripheral region and 25 fields at tumor mass. **C)** and **D)** Log representations of average duration of calcium events at different tumor regions and its frequency (number of events per acquisition period), respectively. The shaded grey area of plot **D** represents rare events where there is only one calcium transient during the imaging period. Statistical significance was determined by the Mann-Whitney test (***p<0.001). A total of 9 mice were used and results represent pooled data from cells that were imaged at different time points, 1-4 weeks post tumor implantation (788 cells in peripheral region and 247 cells in tumor mass).

3.2.5 Importance of *in vivo* studies

In GBM research, both *in vitro* and *in vivo* models play an important role in providing insights into cellular and molecular mechanisms involved in its progression. Advances have been made in *in vitro* models to mimic the biology of human organs, by fine tuning different conditions of the microenvironment to meet experimental needs (142, 143). However, it still does not recapitulate the complexity and natural environment of the brain (143). In contrast,

in vivo studies allow scope for exploration of intrinsic and extrinsic signals regulating GBM growth and invasion, such as tumor-host interactions (105).

For this reason, we compared our *in vitro* data of cultured GL261-TF cells with the data obtained *in vivo*. Figure 3.8A shows a representative image of cultured GL261-TF cells. The cells display distinct difference in cellular morphology compared the *in vivo* phenotype. Cultured GL261-TF cells appear to exhibit a low aspect ratio, i.e. cells are very spherical in shape as shown in Figure 3.8B. However, these cells are more active than cells in the core of the tumor (Figure 3.8C). In addition, we observed that $(Ca^{2+})_i$ activity of cultured GL261-TF cells are significantly lower in duration compared to cells from the mass of the tumor (Figure 3.8D), while exhibiting no significant difference in its frequency between these two population of cells (Figure 3.8E). On the other hand, cells at the periphery hosts a sub population of cells that has higher number of $(Ca^{2+})_i$ events compared to cultured cells. Overall, this data shows the importance of *in vivo* experimentation as it highlights the impact of physiological interaction in $(Ca^{2+})_i$ signaling of GL261-TF cells.

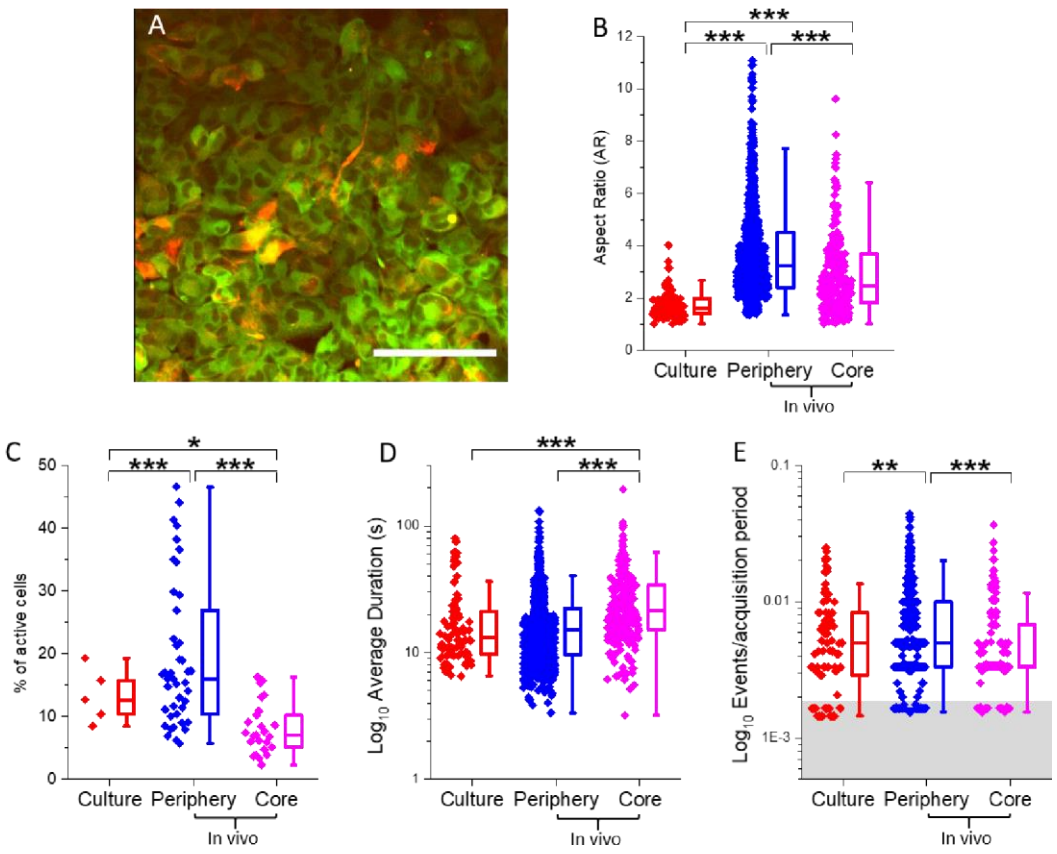

Figure 3.8: Comparison of calcium activity imaged *in vitro* **and** *in vivo*. **A)** Representative image of cultured GL261-TF cells (in green GCaMP6s signal, while in red actin DsRed2). Image is an average projection of a 10 minutes' movie sequence with 1.07s sampling period. The field width is about 305 µm and the calibration bar is 100 µm. **B)** Aspect ratio measurements of *in vitro* and *in vivo* cells. **C**, **D** and **E)** Box plots representing quantification of *in vitro* $(Ca^{2+})_i$ activity and its comparison with *in vivo* data: percentage of active cells, average duration of $(Ca^{2+})_i$ events and the number of events per unit of time, respectively (culture: n = 5 plates, 102 cells; *in vivo*: n = 9 mice, 788 cells in peripheral region and 247 cells in tumor mass). Quantification was done on culture plates with 80-90% confluency. Shaded area in **E** represents an area where there is only one $(Ca^{2+})_i$ transient during the imaging period. Statistical significance was determined by Mann-Whitney test (*p=0.02, **p=0.009, ***p<0.001).

3.2.6 Correlation between *in vivo* calcium activity and short-term migrational potential

Owing to *in vivo* time-lapse microscopy recordings, we were able to image cell behavior that helps us gain biological insights extracted from the obtained quantitative information. In cancer, cells' ability to migrate and metastasize is a hallmark of tumor progression. Since we hypothesized that there is a correlation between $(Ca^{2+})_i$ activity and cellular migration, we first evaluated the migrational pattern of tumor cells from the periphery and tumor mass for a period of 10 minutes' and 60 minutes', using two sets of experiments (n= 5 mice each, respectively). Migration data of the 10 minutes' acquisition period were obtained from the previous set of experiments that were used to evaluate pooled $(Ca^{2+})_i$ activity of cells from different regions of the tumor, taking into account only a sub-population of cells that could be tracked throughout the experiment. The plots in Figure 3.9 shows migratory tracks of each cell at both tumor regions. Cell trajectories are represented starting from the origin (0,0) at

time 0 minute to visualize trajectories of each cell. The displacement of the center of mass of each cell were then recorded every minute over time. We were able to clearly observe the diffusivity of cell tracks, where cells at the peripheral region exhibits a more dispersed trajectory.

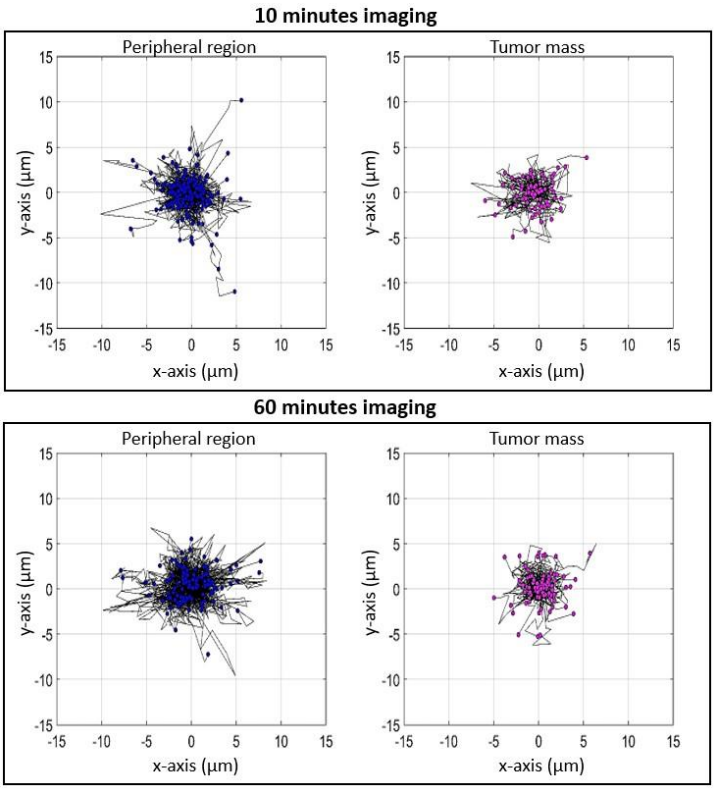

Figure 3.9: Short-term *in vivo* **cell tracks of malignant cells at two different regions of GL261-TF tumor**. **A** and **B)** Representative cell track plots for peripheral region (left) and tumor mass (right). Tumor cells were imaged *in vivo* using two photon microscopy for 10 minutes' **A** and 60 minutes' **B**. The plot describing the diffusivity of cell trajectories are represented starting from the axis origin (0,0). The invasive front which is the peripheral region of the tumor exhibits higher cell motility for both observed duration (peripheral region: 157 cells and tumor mass: 74 cells for 10 minutes' acquisition; peripheral region: 114 cells and tumor mass: 98 cells for 60 minutes' acquisition).

To assess the total displacement of the cells, we quantified the accumulated distance traveled by these cells (Figure 3.10). Cumulative distances were obtained simply by summing up the total displacement of the cells. Our data shows that the accumulated distance of cells at the peripheral region are higher than cells at the tumor mass indicating that they have higher motility and migrated further.

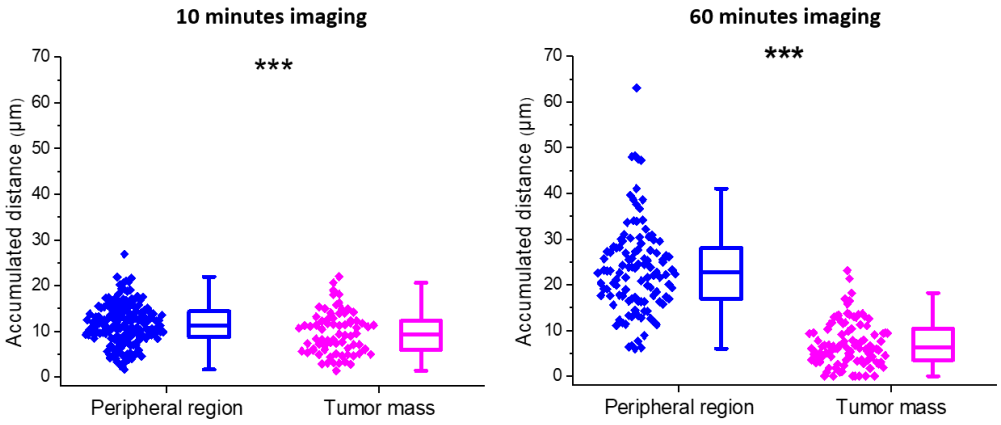

Figure 3.10: Distinct cell motility at different regions of the tumor. Box plots shows the quantification of cell motility by measuring the accumulated distance traveled by cells for a duration of 10 minutes' (left) and 60 minutes' (right). The mean velocity of cells that were acquired for a duration 10 minutes' are 1.29 µm/min at peripheral region and 1.07 µm/min at tumor mass while mean velocity of the cells that were acquired for a duration 60 minutes' are 0.67 µm/min at peripheral region and 0.20 µm/min at tumor mass. P value determined by Mann-Whitney test, ***p<0.001.

Knowing that cells can bias their motility by coupling to signaling cues, we went on to test our hypothesis by evaluating $(Ca^{2+})_i$ activity of these migrating cells (Figure 3.11). In the case of 10 minutes' imaging, $(Ca^{2+})_i$ activity of the chosen sub-population of cells (as previously mentioned) were re-plotted. We observed that the $(Ca^{2+})_i$ activity at the peripheral region are more frequent and shorter in duration for both observed acquisition time supporting our hypothesis that there is a correlation between $(Ca^{2+})_i$ activity and cellular migration, where active $(Ca^{2+})_i$ activity correlates with increased migration capacity. The relationship observed between GBM cell migration and $(Ca^{2+})_i$ dynamics of peripheral region and tumor mass is determined at the level of the cell population while it is rather elusive at the level of individual cells (Supplementary Figure 2). To show that there was no indication of phototoxicity in the 60 minutes' imaging, cell motility plot was split to every consecutive 10 minutes' as shown in Supplementary Figure 3. No distinct slowing down of cells over time were seen in cells from both tumor regions proving that there was no sign of phototoxicity due to microscope illumination.

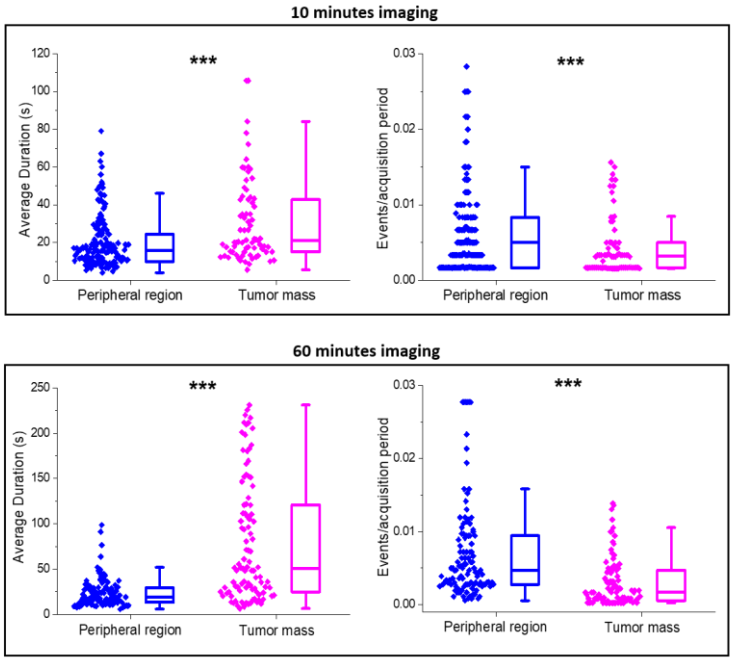

Figure 3.11: Quantification of intracellular calcium events of migratory cells at both tumor regions. **Panel A** and **B): Left** shows the duration of $(Ca^{2+})_i$ transients while **Panel A** and **B): Right** represents the frequency of these events. As expected, cells in the tumor mass, exhibit longer duration and lower frequency of $(Ca^{2+})_i$ activity. Longer duration of $(Ca^{2+})_i$ transient in cells located at the core of the tumor may suggest that these cells require prolonged periods of signaling for them to migrate or proliferate. P value determined by Mann-Whitney test, ***p<0.001.

3.2.7 Calcium imaging of cellular cluster

Here, we report a novel observation of an *in vivo* phenomenon exhibited by GL261-TF cells. This phenomenon was first unraveled when we observed $(Ca^{2+})_i$ transient dynamics of an active ensemble of cells as shown in the exemplificative color coded map in Figure 3.12A, where the color codifies the frequency of $(Ca^{2+})_i$ activity. The map was obtained as follows: from the time lapse data, we computed the fluctuation of fluorescence (ΔF/F) around its median for each pixel. Then, we measured the statistics of the stochastic process associated to each pixel, and we determined that the ΔF/F values are characterized by a bimodal distribution: a quasi-Gaussian mode that corresponds to time points of low or no $(Ca^{2+})_i$ activity and a secondary mode associated to time points of large $(Ca^{2+})_i$ fluctuations. The image stack is then binarized by retaining only the pixels far away from the Gaussian mode by a simple thresholding. The image has been obtained by computing for each pixel the probability that $(Ca^{2+})_i$ is fluctuating over the threshold (144). Interestingly, when the time series of this activity is closely observed, it identifies clusters of cells that display synchronization in their $(Ca^{2+})_i$ activity. To highlight this feature, we present a binarized sequence of images as shown in Figure 3.12B representing temporal evolution of $(Ca^{2+})_i$ transients. The yellow and red arrowheads points to two cellular ensembles that show strong co-activation. $(Ca^{2+})_i$ activity starts from one cell and triggers activity in nearby cells. We refer this high synchronization as cluster activation.

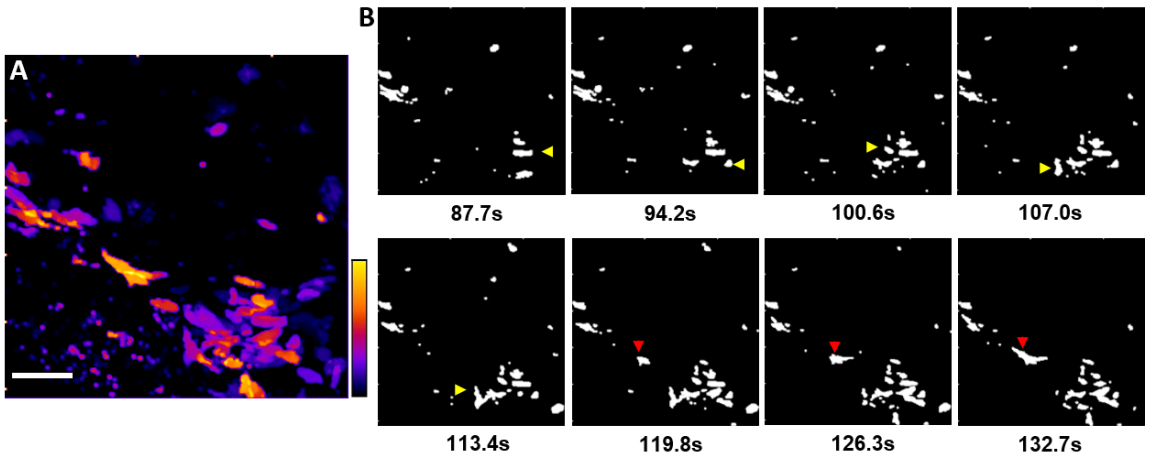

Figure 3.12: Cluster activation. **A)** Color coded map that represent the frequency of $(Ca^{2+})_i$ fluctuation of each pixel of the image. Imaging was performed 26 days after grafting in the host cortex. The movie sequence is about 5 minutes' long and the sampling period is 1.07s. $(Ca^{2+})_i$ transient are far more frequent in small groups of cells. **B)** Sequence of the binarized images showing the temporal evolution of the spatial domains invaded by $(Ca^{2+})_i$ transients (time in seconds). The yellow and red arrowheads point to cell ensembles that show strong co-activation.

We then transformed this observation to a quantitative data. We used an example mouse in Figure 3.13A-E to present this analysis. First, we performed wide field (WF) imaging to visualize Ca^{2+} activity of the GL261-TF tumor at a mesoscale level. Next we selected an area with high activity and zoomed in using the two photon microscope to closely observe this activity at a cellular level (Figure 3.13A). The temporal evolution of a selected cluster (white box) is shown in Figure 3.13B for better visualization. Region of interests (ROIs) were drawn around cells belonging to clusters and random cells around the clusters (i.e. remote cells). Figure 3.13C shows the ΔF/F of $(Ca^{2+})_i$ activity of 111 ROIs, where a total of 4 clusters showing high degree of synchronization could be seen. We then calculated Pearson's correlation of all possible pairs of $(Ca^{2+})_i$ traces and plotted its distribution as shown in Figure 3.13D (blue bars). According to our data, the distribution shows a peak on the right side of the histogram (right tail) that demonstrates the existence of cell clusters endowed with highly correlated $(Ca^{2+})_i$ activity. The red shaded area represents pairs of traces that has a correlation coefficient of $R \geq 0.9$. To show that the temporal organization of the $(Ca^{2+})_i$ activity of GL261-TF cells underlies the existence of highly correlated cells clusters, we performed random temporal permutations on each of these traces for n = 1000 times (see Methods, section 3.4.12 for details). Next, we calculated the linear correlation of all possible pairs and plotted the averaged distribution curve that is overlaid (gray shaded area) over the original correlation distribution in Figure 3.13D. The disappearance of the right tail and the leftward shift of the curve after permutation, shows that the right most population is due to correlated activity. This strong co-activation can be seen distinctly from the connectivity map in Figure 3.13E, where the red lines indicates connectivity at correlation coefficient of $R \geq 0.9$. Subsequently, we plotted a global distribution of correlation coefficients from 715 cells obtained from 7 mice

(11 acquisition fields) (Figure 3.13F). The evident right tail that could be seen from the distribution, supports our observation of high synchronization in clusters of cell.

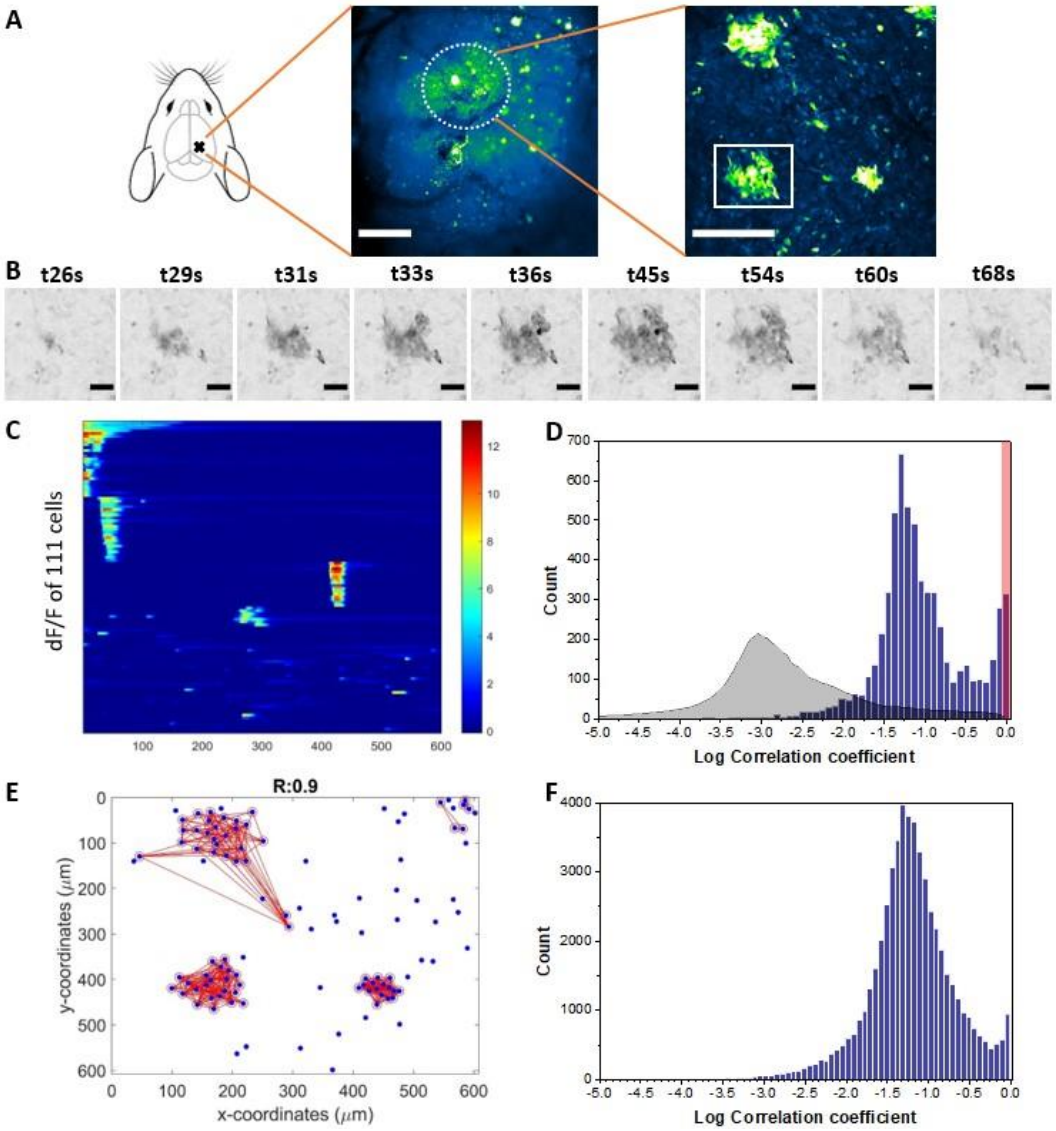

Figure 3.13: Quantification of GL261-TF cell cluster activation. **A)** Calcium imaging was done on the right hemisphere of a GL261-TF mouse 18 days' post implantation using wide field microscopy and two photon microscopy. Image in middle represents a standard deviation projection of a 10 minutes' movie sequence acquired from a wide field (WF) microscope (scale bar: 500 μm). Image on the right represents a standard deviation projection of a 10 minutes' movie sequence, 80 μm depth from the surface, acquired from a two photon microscope, estimated around the area of the dotted circle in the WF image (scale bar: 200 μm). The two photon image from this example mouse shows clusters of cells (bright group of cells) that activates almost simultaneously. **B)** Sequence of images showing temporal evolution of $(Ca^{2+})_i$ transients in one cell cluster represented by a white square in **A** (time in seconds) (scale bar: 50 μm). **C)** Raster plot corresponding to $\Delta F/F$ of $(Ca^{2+})_i$ fluctuations of 111 cells belonging to clusters and remote cells acquired from two photon imaging. ROIs from clusters were arranged together manually by the experimenter in the raster plot for better visualization of $\Delta F/F$ activation. **D)** Distribution of Pearson's correlation coefficient of $(Ca^{2+})_i$ computed on pairs of traces from the selected ROIs (blue bars). The large right tail in the histogram shows that there are groups of cells that exhibits high correlation. The distribution curve represented as the gray shaded area on the plot shows the paired correlation of traces after permutation. Data that falls in the red shaded area represents pairs of traces that has a correlation of R≥0.9. **E)** Functional connectivity map of cells (red lines) at correlation threshold, R≥0.9. Centroid of all 111 ROIs are represented in blue with the exact coordinates as in the two photon imaging field in **A)**. **F)** Distribution of correlation coefficients of $(Ca^{2+})_i$ traces of 715 cells obtained from 7 mice. Once again, a clear peak at the right tail of the histogram suggests that there are a groups of cells that has high synchronization in their $(Ca^{2+})_i$ activity.

Next, we wanted to evaluated if there is a correlation between cluster activation and cellular migrational potential. Therefore, we assessed the migration pattern from the same cells of the example mouse in Figure 3.13. This analysis was done on 3 mice that presented the best clustering activity. Data of the other 2 mice are included in the Appendix section (Supplementary Figure 4-7). Centroids of cells belonging to clusters are represented by red dots and remote cells are represented by green dots (Figure 3.14A). Trajectories of cells are plotted starting from the xy (0,0) coordinates at time 0 minutes' and their end point coordinates at time 10 minutes' (Figure 3.14B). Interestingly, the averaged euclidean distance of cells in clusters seem to have a preferred direction compared to remote cells. It will be worthwhile to investigate further what are the factors contributing to this migration behavior such as gap junctions, and specifically connexin43 (Cx43) that can play a significant role in these processes, impacting adhesion and cytoskeletal rearrangements (145).

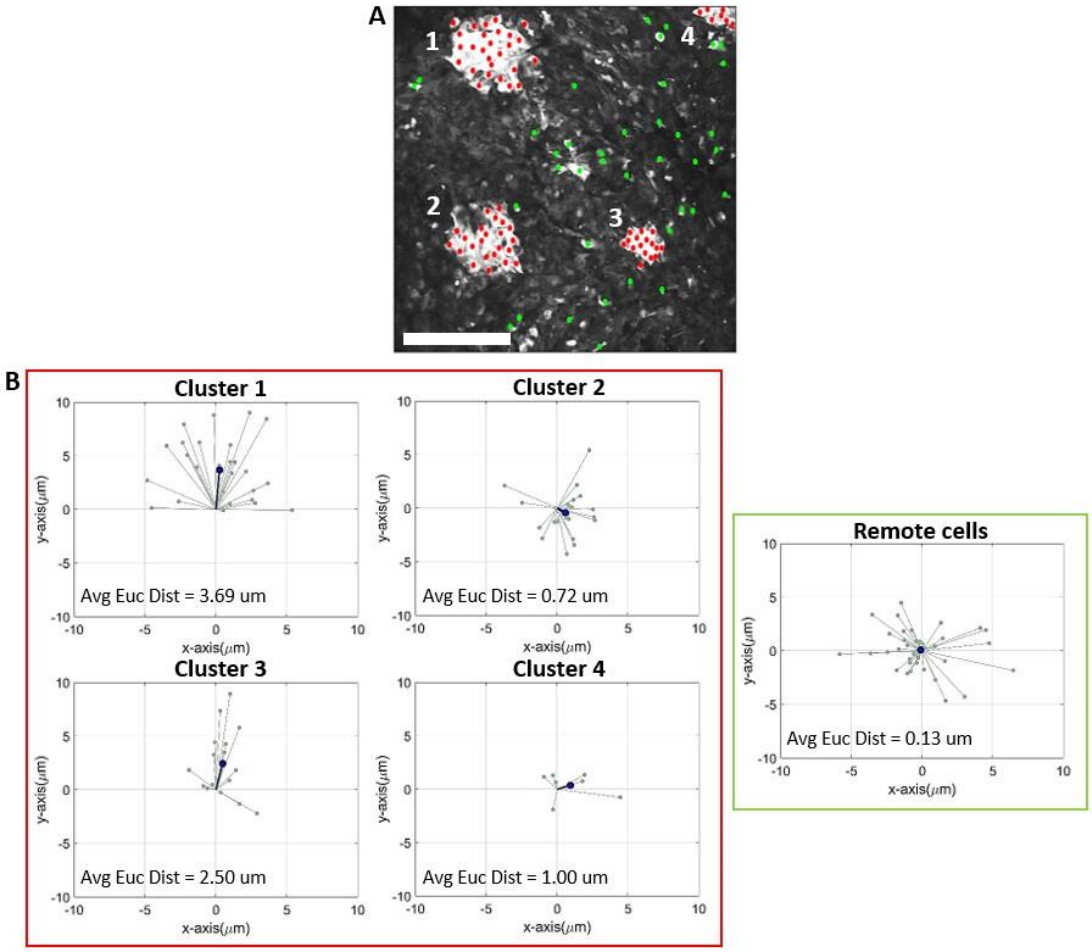

Figure 3.14: Migrational pattern of cell clusters. **A)** Two photon image as in Figure 3.13A (scale bar: 200 μm). Red dots represent centroid of cells that belong to clusters while green dots represent random cells that does not belong to a cluster (i.e. remote cells). **B)** Cell tracks of clusters (in red square) and remote cells (in green square) observed over a period of 10 minutes'. Cell trajectories were plotted starting from xy coordinated (0,0) at time 0 minutes' and the end coordinates. The euclidean distance each cell is represented with a gray marker-line and the weighted average is represented by blue marker-line. Our data shows that the cell clusters have preferred direction of migration compared to remote cells (Cluster 1: 27 cells; Cluster 2: 23 cells; Cluster 3: 16 cells; Cluster 4: 7 cells; Remote cells: 38 cells) (Avg Euc Dist = average euclidean distance).

3.3 Discussion

Research on intratumoral heterogeneity in GBM is a growing field and yet to be extensively studied. Although there is no single experimental model that can recapitulate the diverseness of human GBM pathobiology, insights into intrinsic signaling patterns of the tumor can provide new potential therapeutic target for the treatment and management of GBM. Here, we developed a fluorescent orthotopic GBM model with a genetically encoded calcium sensor and exploited time-lapse *in vivo* microscopy technique to analyse the intrinsic intratumoral calcium dynamics and its correlation with tumor cell migration. Prior to utilizing our model further down the experimental pipeline, we validated it with respect to the conventional non-fluorescent GL261 model. By validating our model, we examined the effect of transfection, cell sorting and the expression of GCaMP6s-DsRed2 on GL261 cell properties. We sought to address the aggressive phenotype of GL261-TF tumor when translated *in vivo* for downstream experiments. We found that in *in vitro* assays, GL261-WT cells harbors a more elongated morphological phenotype and marginally higher migrational potential than the stably transfected cells. However, there were no differences in the survival curves of mice implanted with GL261-WT and GL261-TF cells, thus demonstrating that both cell lines behave similarly in the complex environment of the brain. Therefore, our fluorescent cell line has a similar *in vivo* growth and aggressive phenotype of GL261 murine glioma cells.

Intratumoral cell morphology.

In vivo, the protrusive force of actin polymerization drives malignant cells into an elongated morphology enabling these cells to break away from primary cell mass and invade into the extracellular matrix of the brain (146, 147). Using our fluorescent model, we were able to clearly define two distinct regions of the tumor characterizing its heterogeneity. Similar regions have been distinguished in a study by Alieva et al. (102), where they quantified cell motility of patient derived tumor cells *in vivo* at different areas of the tumor border. In our study, we found that cells at the periphery exhibit an elongated morphological phenotype compared to cells at the tumor mass. Cells at the periphery are composed of tumor cells that are invading into the brain parenchyma. Regulation of traction forces at the cell front and rear could be the main contributing factor to the shape of the tumor cells at the invading front. This highlights that cellular morphological feature is a signature of cancer cell state (148).

Intratumoral calcium dynamics.

Calcium plays an important role in tumor biology and regulation of malignant characteristics in tumor cells (41). Despite having a pivotal role in GBM progression, intratumoral calcium dynamics have never been explored. Here, we first report global *in vivo* $(Ca^{2+})_i$ activity at 4 different time points post cortical tumor cell implantation. Tumor cells tend to exhibit higher overall $(Ca^{2+})_i$ activity during early developmental stages (1st and 2nd week). This suggests that at early developmental stages, tumor cells initiate active crosstalk that triggers and produce rapid growth cues (149). Even so, we can't ignore that the contribution

to this disperse global $(Ca^{2+})_i$ activity are from cells located in different tumor regions. Therefore, we analysed separately the $(Ca^{2+})_i$ dynamics of cells at the peripheral region and in the tumor mass. Cells at periphery not only differ in morphology, but they also display higher $(Ca^{2+})_i$ activity. Changes in temporal properties of $(Ca^{2+})_i$ signaling results in distinct cellular function modification. Therefore, we postulate that peripheral tumor cells mediate short and frequent $(Ca^{2+})_i$ transients that possibly establishes a signaling network that propagates information to establish and coordinate neighboring malignant cells to an enhanced infiltration and migration phenotype (39, 42).

Importance of tumor-host interaction.

The bidirectional communication between tumor cells and host environment is crucial in sustaining malignant growth and progression (150). The complex environment of the brain provides heterogeneous interactions that influences tumor intracellular signaling and promotes required adaption that aids tumor cells to invade and proliferate into the tissue (151, 152). In line with this, we show that the cultured GL261 tumor cells exhibit marked differences in cellular morphology and $(Ca^{2+})_i$ activity when compared to our *in vivo* data. *In vitro* GL261 cells are significantly less active and they portray different $(Ca^{2+})_i$ dynamics where the duration of $(Ca^{2+})_i$ events are comparable to *in vivo* peripheral cells while the frequency of events are closer to GL261 cells located at the tumor core. Our study highlights the importance of *in vivo* experimentation on the grounds that *in vitro* studies lack the involvement of host physiological conditions that do not fully recapitulate GBM intratumoral heterogeneity.

Correlation between intratumoral calcium activity and migration pattern.

A benefit of combining time-lapse microscopy and our fluorescent tumor model, is that tumor cell behavior can be longitudinally studied in an immunocompetent mouse. We correlated the total distance traveled by tumor cells at the two defined regions and their $(Ca^{2+})_i$ activity. Interestingly, we found a positive correlation between the migratory potential and $(Ca^{2+})_i$ activity. Cells located at the periphery migrated further and exhibited higher $(Ca^{2+})_i$ signaling compared to the cells at the tumor mass. Our data underline the importance of intracellular Ca^{2+} oscillations within different regions of the tumor, particularly in the frequency and duration of oscillations, in composing specific $(Ca^{2+})_i$ codes for tumor cell proliferation and migration (149, 153).

Synchronized calcium activation in clusters: A novel observation.

To adapt to changing environment such as the brain, cells need to communicate and establish mutual cooperation. Therefore, cells must signal, and signaling requires messenger molecules that are specifically activated in time and space. Ca^{2+} is an important secondary messenger participating in the regulation of most cellular processes (30). This notion leads to an emerging concept based on glioma crosstalk, i.e. between glioma-glioma and glioma-host interactions. Therefore, we are led to ask how modulation of $(Ca^{2+})_i$ activity affect GBM proliferation and infiltration. Recently, Venkatesh et al. (154) and Venkataramani et al. (155) studied functional neurogliomal interactions and observed synchronized patterns of Ca^{2+}

activity in connected glioma cells when stimulated, suggesting that calcium waves might spread through gap junction-linked glioma cell networks. In addition to this study, Montgomery et al. reported desynchronization of neuronal $(Ca^{2+})_i$ activity between the glioma region and contralateral cortex, as well as disruptions in the synchrony of both neuronal and hemodynamic activity across the brain (156). However, intrinsic synchronization of $(Ca^{2+})_i$ activity in GBM cells have not yet been reported. Our study disclose a novel observation of high synchronization of $(Ca^{2+})_i$ activity in clusters of GBM cells. The distribution plot presenting correlation of $(Ca^{2+})_i$ traces as shown in Figure 3.13D and F, reveals a peak at the right hand of the histogram highlighting a high correlation of $(Ca^{2+})_i$ activity in a group cells. We also demonstrated that cells in these clusters display a bias in their migratory direction. The existence of this phenomenon could be due to that GBM cells creates a small intrinsic network of cells possibly via gap junctions to modulate synchronized $(Ca^{2+})_i$ activity and provide directional infiltration signals within the clusters of cells. However, further investigation is necessary to characterize this observation.

In conclusion, our work is the first to analytically study intratumoral calcium activity and its correlation in the migration pattern of cells located at different regions of the tumor. Data from this study highlights the importance of intratumoral signaling in understanding GBM invasion pattern. Moreover, we reported a novel observation that could identify a new potential target for the treatment of GBM. Future work should be directed to characterizing cells at different regions of the tumor and cells belonging to the highly correlated clusters, by using new state of the art molecular techniques like RNA sequencing to decode its gene expression patterns particularly in genes encoding for calcium channels.

3.4 Methods

3.4.1 Plasmid

Stably transfected GL261 cell line was produced from pPBC-G6s plasmid, which was kindly donated to us by Karen Wilcox (University of Utah). pBC-G6s is based on a pSP72 backbone and it expresses calcium sensor GCaMP6s under the constitutive promoter CAG. The GCaMP6s gene, together with the promoter, is flanked by *piggyBac* ITRs, that allow its insertion in a target cell genome in the presence of the helper plasmid, *piggyBac* transposase (PBase). We modified this plasmid by adding at the C-terminal of GCaMP6s an autocleavable linker P2A, followed by the red fluorescent protein (RFP) DsRed2 which was modified by adding an N-terminal actin-staining peptide (LifeAct). The RFP was added using a standard digestion-ligation procedure, by using pBC-G6s as vector and inserting the LifeAct-RFP from a custom plasmid synthesized by a gene synthesis facility (Aurogene), using PstI and NotI restriction enzymes. the subsequent final structure was used in all experiments of the GL261 model. Transformations have been performed in One Shot Stbl3 chemically competent *E. coli* cell line

(Thermo Fisher Scientific) while the final plasmid used for transfection was produced using the QIAGEN Plasmid Plus Maxi Kit.

3.4.2 Cell culture transfection

GL261 wild-type (GL261-WT) cell line was given to us by Matteo Caleo, CNR Pisa. Cells were cultured in Dulbecco's modified Eagle's medium (DMEM, Gibco) containing 10% fetal bovine serum, 1% penicillin-streptomycin (100 units/mL of penicillin and 100 µg/mL of streptomycin, Gibco), 1 mM sodium pyruvate (Gibco) and 10mM HEPES (Gibco). Transfections were performed through electroporation on cell suspension. Cells cultured on P60 Petri dishes (60 mm diameter) at 80% confluency were detached using 0.05% Trypsin-EDTA (Gibco), washed with 5 mL of Dulbecco's Phosphate-Buffered Saline (PBS) and centrifuged at 1200 rpm for 5 minutes'. Pelleted cells were re-suspended in 120 µL of electrolytic buffer (Invitrogen) with 5 µL of plasmidic DNA. Resuspended cells were electroporated using MicroPorator MP-100 (Digital Bio, 2 pulses at 1200 V with a duration of 20 ms). The amount of DNA used is approximately 10-20 µg. Transfected cells (GL261-TF) were then plated and maintained in the prepared culture medium, replaced 2-3 times per week, in a humidified atmosphere of 5% CO_2 at 37 °C. To achieve a 100% stably transfected fluorescent cell line, electroporated cells were sorted using Bio-Rad S3e Cell Sorter. For injection, sorted cells were grown up to 90% confluency in a P60 petri dish and harvested using 0.05% Trypsin-EDTA. Cells were then pelleted by centrifugation at 1200 rpm for 5 minutes', re-suspended to cell concentration of 20 000 cells/µL with PBS.

3.4.3 Cell proliferation assay

GL261 cells (GL261-WT and GL261-TF) were detached using 0.05% Trypsin-EDTA (Gibco), washed with culture medium, centrifuged at 1200 rpm for 5 minutes' and resuspended with culture medium. Centrifugation was done to minimize the number of dead cells and cell debris. Then, 10 μL of cell suspension was added to 10 μL of Trypan Blue stain 0.4% (Invitrogen) and loaded into cell counting chamber slides (Invitrogen). Counts were performed using the benchtop Countess Automated Cell Counter (Invitrogen). Cells were seeded on a P60 petri dish at starting density of 1 x 10^4 cells. Cells were detached and counted using the automated cell counter for a period of 6 days, where one petri dish per day was used (6 petri dishes/cell line each trial). A total of 3 trials were done.

3.4.4 Wound healing assay

In vitro cell migration assay was done by preparing cell suspension in culture medium and counting the cells as described in 3.4.3. Cell suspension then was adjusted to a cell concentration of 4 x 10^5 cells/mL to obtain a confluent cell layer after 24 hours. 70 μL of cell suspension was applied to each well of the Culture-Insert Well (Ibidi) that was place in P35

petri dish (35 mm diameter) and incubated at 37 ° C in 5% CO_2 for 24 hours. Once a confluent layer is formed, Culture-Insert Well was gently removed with sterile tweezers. Petri dish was then washed and filled with fresh culture medium to remove dead cells, non-attached cells and cell debris. Cells was imaged with Zeiss LSM-800 Airyscan confocal microscope under brightfield mode. Images were acquired using a 20X air objective (NA 0.5) for 2-3 consecutive days until gap closure. Images are at a resolution of 1024X1024 pixels, with a field of about 638.9 μm and a linear pixel size of 0.624 μm per pixel.

3.4.5 Animals

C57BL6/J mice strain were obtained from The Jackson Laboratory (stock number #000664) and maintained at Istituto di Neuroscienze (CNR, Pisa) animal house on a 12 h light cycle and fed *ad libitum*. For all experiments, mouse of either sex were studied unless stated otherwise. All animal care and experimental procedures were performed in strict accordance with the recommendations of the Italian Ministry of Health (Dlg. 26/14) and according to protocol 143-2017 PR approved by the Ministry of Health on February 13, 2017.

3.4.6 Intracortical injections of GL261 cell line

Mice were anesthetized with 2,2,2-tribromoethanol (Avertin) (0.02 mL/g body weight) intraperitoneally and mounted on a stereotactic stage. The head was secured using two metal ear bars and a nose clamp. The hair on the head was removed using a hair depilatory cream and a single skin cut of approximately 0.5-1 cm was made using a pair of scissors and the exposed sub-cutaneous tissue was gently removed. A small needle-size hole around the visual area was made using a hand drill and washed with few drops of PBS to clean the injection area. Next, 4 x 10^4 GL261 cells suspended in 2 µL of PBS were injected stereotactically using a glass capillary in the middle of the drilled grove at a depth of 0.3 mm. A total of 5 minutes' were spent for the injection and an additional 2 minutes' before removing the glass capillary to avoid spill overs. The surface of the injection site was then washed with PBS before closing the skin with simple stitches. Iodine antiseptic cream was applied on the stitches to prevent infection. A single dose of antipyretic, i.e. 5 drops of paracetamol (100 mg/mL) per 100 mL of drinking water was provided for the animals after surgery. Mice were closely monitored for behavior, reactivity and appearance.

3.4.7 Survival analysis

C57BL6/J mice were divided into 2 groups and implanted with tumor cells, GL261-WT and GLL261-TF, respectively (6 mice/group). Tumor implantation was carried as described in section 3.2.4. Animals were maintained on a 12 h light cycle and fed *ad libitum*. Animals were closely monitored and body weights were recorded daily. Endpoint of the experimental

duration is achieved when the mice has reduced 20% of its initial body weight. All animals were sacrificed with an overdose of anesthesia at the end of the experiment.

3.4.8 Cranial window surgery

Cranial window surgeries were performed at different time points according to experimental requirements, earliest being 1-week post tumor implantation. Mice were anesthetized with Avertin (0.02 mL/10g) and mounted on a stereotactic stage as described in section 3.2.4. During the experiment, the body temperature of mice was monitored and held constant at 37 °C with a feedback-controlled heating blanket (Harvard Instruments). Using a pair of scissors, a longitudinal incision of the skin was performed between the occiput and the forehead, followed by skin and sub-cutaneous tissue removal around the injected site. A custom-made steal head post with a central imaging chamber was then glued with cyanoacrylate in a plane approximately parallel with the skull over the cortical region of interest and cemented in place with white dental cement (Paladur). Using a hand drill, the skull was thinned to open a 5 mm diameter window. Forceps were used to break and remove the skull gently. The dura mater was continuously rinsed with sterile artificial cerebrospinal fluid (ACSF; 126 mM NaCl, 26 mM $NaHCO_3$, 1.3 mM $MgSO_4$, 3 mM KCl, 1.25 KH_2PO_4, 2.4 mM $CaCl_2$, 15 mM glucose and 1.2 mM HEPES in distilled H_2O, pH 7.4). A 5 mm cover glass was used to cover the craniotomy and secured with cyanoacrylate glue.

3.4.9 *In vivo* two-photon microscopy

High resolution *in vivo* imaging was performed with a Prairie Ultima Multiphoton microscope (Bruker) equipped with a mode-locked Ti: Sapphire laser (Chameleon Ultra II, Coherent) through a 20X Olympus XLUMPLFLN water immersion objective (numerical aperture 1.0). The power at the sample surface during acquisitions was maintained under 50 mW. The tumor is extremely scattering and such power was required to perform any significative imaging. It should be pointed out that, due to scattering of the excitation beam, only a fraction of this power reaches the focal plane contributing to fluorescence emission. Fluorescent cells were imaged at various depth in the cortex. All imaging experiments were performed at the excitation wavelength of 980 nm. This wavelength was chosen for two reasons: 1. to be able to excite both GCaMP6s and LifeAct-DsRed2; 2. to enable acquisitions into deeper cortical tissue. The emission filters band-pass used were 490-560 nm for the green channel and 584-680 nm for the red channel. Time lapse imaging of 10 minutes' was acquired at a resolution of 512X512 pixels at zoom 2, leading to a field of about 304.1 μm and a linear resolution of 0.59 μm per pixel. Time lapse imaging of 5 minutes' was acquired at a resolution of 512X512 pixels at zoom 1, leading to a field of about 608.3 μm and a linear resolution of 1.19 μm per pixel. Image reconstruction was done by acquiring a set of Z-stacks in the tumor regions at a resolution of 512X512 pixels at zoom 1, leading to a field of about 608.3 μm and a linear resolution of 1.19 μm per pixel. Stack step size was 2 μm.

3.4.10 Tumor volume

Tumor volume was measured *in vivo* at different time points post tumor implantation. The subcutaneous volume was estimated by determining the x, y and z measurement of the tumor under two-photon microscope. Tumor volume was calculated assuming an ellipsoid shape, where l is length, w is width and h is height (157):

$$V = \frac{4}{3}.\pi.\frac{l}{2}.\frac{w}{2}.\frac{h}{2} \tag{3.4.1}$$

3.4.11 Wide-field imaging

In vivo wide-field calcium imaging was performed on anesthetized animal being placed on a stereotactic frame under a customized imaging setup (Figure 2.3). The cortex was illuminated with a blue emitting diode (LED) of 445 nm wavelength with a constant current controller. The light source (Solis-3C, Thorlabs) was reflected by a dichroic mirror through the objective lens pass the chronic window and into the cortex. The emitted GCaMP6s fluorescence was filtered with 515 nm longpass filter and acquired using a sCMOS compact camera (sCMOS pco.edge 4.2 LT HQ). Spontaneous cortical activity was acquired at 5 Hz with 195 ms exposure. Time lapse imaging was acquired for a period of 10 minutes' at a resolution of 512X512 pixels at zoom 5, leading to a field of about 2381.2 μm and a linear resolution of 4.651 μm per pixel.

3.4.12 Two-photon imaging analysis

In vivo data obtained from two photon microscopy were composed of 12-bit images. Acquisitions were corrected for motion using NoRMCorre Matlab code (158). ImageJ (NIH) was used to manually draw regions of interest (ROIs) and extract measurements. These measurements were then analysed using custom made Matlab code that computes fluorescence fluctuation of each cell. Briefly, the raw fluorescent trace, F, of each cell extracted using ImageJ was smoothed by calculating its moving mean over a sliding window of 3s across the whole trace and the minimum value was determined, Fmin (unless otherwise mentioned). Then the change of fluorescence over time, Δ F/F, was calculated using the following formula:

$$\Delta F/F = \frac{(F - Fmin)}{Fmin} \tag{3.4.2}$$

Once the fluorescence fluctuation has been calculated, the distribution of the Δ F/F of each ROI is computed and fitted with a normal distribution to extract its mean (μ) and standard deviation (std, σ). A threshold is set at $\mu + \sigma$. Segments of traces that are higher than the threshold and longer than 3s are considered as events. Two events are considered as separate if they are >1s apart, otherwise they are merged. Duration is defined as time over the threshold. Frequency refers to the number of events per duration of acquisition in each cell.

Pearson's correlation analysis was performed on calcium traces to evaluate how similar two traces were on a temporal scale. This analysis was done on every possible unique pairs of calcium traces (i.e. unique pairs of cells) in an acquisition field. Therefore, the total number of pairs (counts) is given by the following equation:

$$Total\ number\ of\ pairs = \sum_{i=1}^{N} \frac{x_i(x_i - 1)}{2} \tag{3.4.3}$$

where x_i= number of traces for i^{th} field of acquisition and N = number of acquired fields. Permutation test was computed to evaluate the temporal dependency of $(Ca^{2+})_i$ transients while maintaining its temporal structure. It is done as a resampling-based method, where calcium traces were permutated at random positions on a temporal scale. Briefly, a random number between 0 and 1 was generated and multiplied with the total duration of the trace. Then, the trace is disconnected at the computed random time point and flipped, where this random time point will be the new origin.

3.4.13 Statistics

Data were placed in Origin Pro 9.0 to generate graphs. Where appropriate, data have been represented as box plots. Boxes indicate the 25 and 75 percentiles while whiskers indicate the 5 and 95 percentiles. All data were analysed using the non-parametric Mann-Whitney test.

Chapter 4

Spontaneous GBM Model

In this chapter I will describe a spontaneous GBM mouse model that is being currently explored. This tumor model is not obtained after injection of extraneous cells, but it is induced by transfecting the astrocyte progenitors with mutations of high oncogenic capacity. Preliminary results presented in this chapter is a proof of concept for future research mainly focusing on testing the oncogenic potential of specific mutations, calcium signaling and its involvement in GBM cellular migration.

4.1 Introduction

Development of the neocortex relies on coordinated regulation of a pre-determined developmental program. It begins from stem cells to progenitors, which then generates differentiated cells to form functional organs and tissues (159). Many human diseases including cancers are caused by perturbation to this natural development program (160, 116). Therefore, to understand tumor etiology and heterogeneity in the cerebral cortex, it important to study them from a developmental point of view.

In the effort to unravel GBM intra- and intertumoral heterogeneity especially in terms of invasiveness, several models have been explored (161). However, the best comprehension of mechanisms and signaling events that drives GBM invasion should be conducted in *in vivo* models, where the brain physiological environment is maintained intact. In recent years, genetically engineered mouse models (GEMMs) particularly via somatic mutations, have been used to assess GBM biology. Somatic transgenesis of oncogenes or deletion of tumor suppressor genes by both viral and non-viral techniques are being used to target specific endogenous cell populations (109). There are two widely used viral techniques: retrovirus and RCAS-tva system (replication-competent avian sarcoma-leukosis virus long terminal repeat with splice acceptor/tumor virus A (TVA)), where the RCAS virus can only infect cell lines or transgenic mouse lines that expresses the TVA avian retroviral cell surface receptor (162). However, these viral-based techniques present few limitations such as cargo limit, some require transgenic animals, labor and cost intensive. Conversely, the non-viral technique using *in utero* electroporation (IUE) of DNA transposons is cheaper, faster and allows multigene delivery with no species dependency. Table 4.1 summarizes the difference in existing labeling techniques.

Methods	Advantages	Limitations
Retrovirus	Time control, Permanent	Differential infectivity of cells, Potential integration site effects, Cargo Limit
RCAS-tva system	Permanent	Dependent on gene/promoter expression, Require transgenic animals, Labor and cost intensive, Species dependent
Tissue-specific recombinase	Noninvasive, Permanent	Dependent on gene/promoter expression, Require transgenic animals, Labor and cost intensive, Species dependent
Mosaic Analysis With Double Marker (MADM)	Non invasive, Multicolor, Permanent, Sparse labeling	Require transgenic animals, Labor and cost intensive, Species dependent
In utero electroporation of DNA transposon	Simultaneously labeling and manipulation, Time control, Cheaper and faster, Not species dependent	Invasive, Accessibility to cells

Table 4.1: Comparison of existing methods for neural progenitor labeling. Adapted from Chen and LoTurco. (163).

DNA transposon system integrates DNA sequences into the genome via cut and paste mechanism in the presence of an enzyme called transposase. There are 3 types of transposons, i.e. *Tol2*, *Sleeping Beauty* and *piggyBac* (164, 165, 166). Among these 3 transposons, *piggyBac* transposon system is particularly useful because it preferentially integrates into the TTAA site of the genome for precise excision and has a unique ability to leave no 'footprints' after excision from an insertion site. It also has larger cargo capacity and no overproduction inhibition has been reported. Therefore, *piggyBac* transposon system is widely used for insertion of mutagenesis, lineage tracing and gene therapy studies (167).

In oncology research, Ras mutations have been extensively studied. Active Ras pathway have been found in patients with glioma and therefore used in various glioma animal models (111, 113). Among the isoforms of Ras GTPase, H-Ras accounts for a small proportion of mutant Ras cancers (Table 4.1). In recent years, there have been renewed efforts to study this isoform, especially in H-Ras driven central nervous system cancers. Important advances have therefore been made not only in the understanding of H-Ras structural biology but also in approaches designed to inhibit and impair its signaling activity (168).

Cancer Types	% Mutation		
	H-ras	K-Ras	N-ras
Glioblastoma	0.5	0.8	0.6
Lower Grade Glioma	0.1	1.0	0.6

Table 4.2: Ras mutation frequency in glioma

The MAPK/ERK pathway (mitogen-activated protein kinases/extracellular signal-regulated kinases), also known as the Raf-MEK-ERK pathway is a chain of proteins that carries signal from cell surface receptor to the DNA in the nucleus (168). H-Ras activates this Raf-MEK ERK chain that carries growth receptor signals where transcription factors such as Myc initiate transcription of genes in the nucleus related to cell proliferation, epithelial to mesenchymal transition and cell survival. Additionally, PI3K/AKT (phosphoinositide 3-kinase/protein kinase B) signaling has also been linked to H-Ras. This pathway carries signals that results in the activation of mTOR (mammalian target of rapamycin), which then facilitates protein synthesis, cell migration and cell proliferation (168, 169) (Figure 4.1).

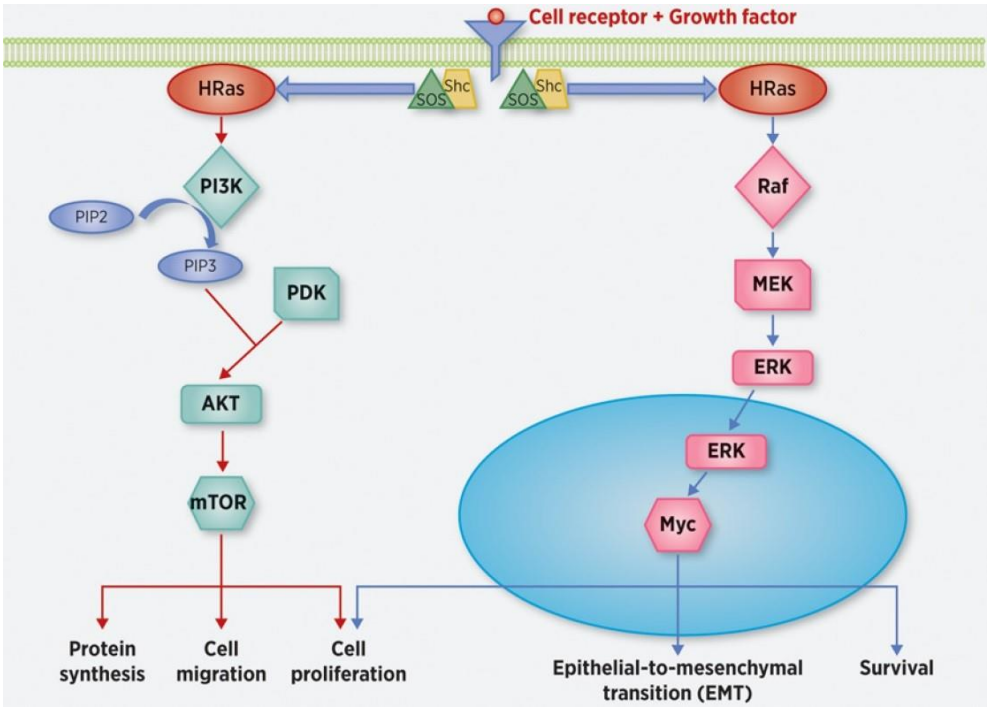

Figure 4.1: H-Ras signaling pathways (Adapted from Shu et al. (168))

Hence, in this study, we generated an on demand glioma model (i.e. spontaneous GBM model) by exploiting a construct that allows the knock in of a constitutively active mutant of Ras (HRasV12) (163) flanked by the consensus sequence for the *piggyBac* transposase using IUE technique. This preliminary study would be a proof of concept for future research on evaluating GBM intratumoral calcium activity, its involvement in tumor cell migration

properties and on the effect of specific mutation on the invasive phenotype and tumor severity.

4.2 Preliminary Results and Discussion

We produced a spontaneous GBM tumor model via non-viral somatic transgenesis from endogenous mice neural progenitors *in vivo*. The oncogene HRasV12 was introduced into radial glial progenitors by IUE technique of the occipital cortex of embryonic mice. We used the helper plasmid that expresses *piggyBac* transposase through the glutamate aspartate transporter, GLAST promoter (GLAST-PBase) to drive donor plasmid integration into the genome of radial glial progenitors. The donor plasmids consist of fluorescent reporters (genetically encoded calcium indicator GCaMP6s (green) and LifeAct-DsRed2 (red)) and the active mutant of Ras (HRasV12) (Figure 4.2A). Electroporation of these plasmids were done at embryonic age 15 (E15) to target a higher percentage of astrocytes because GBM tumors are of astrocytic origin (115). Pups were then imaged at postnatal age 10 to 14 using two photon microscopy (Figure 4.2B-D). The resulting tumor appears to be an aggressive type related to short survival of pups, since generally they do not survive after postnatal age 20 (P20). All experiments were done acutely because the treated pups could survive only up to approximately 9 hours post anesthesia.

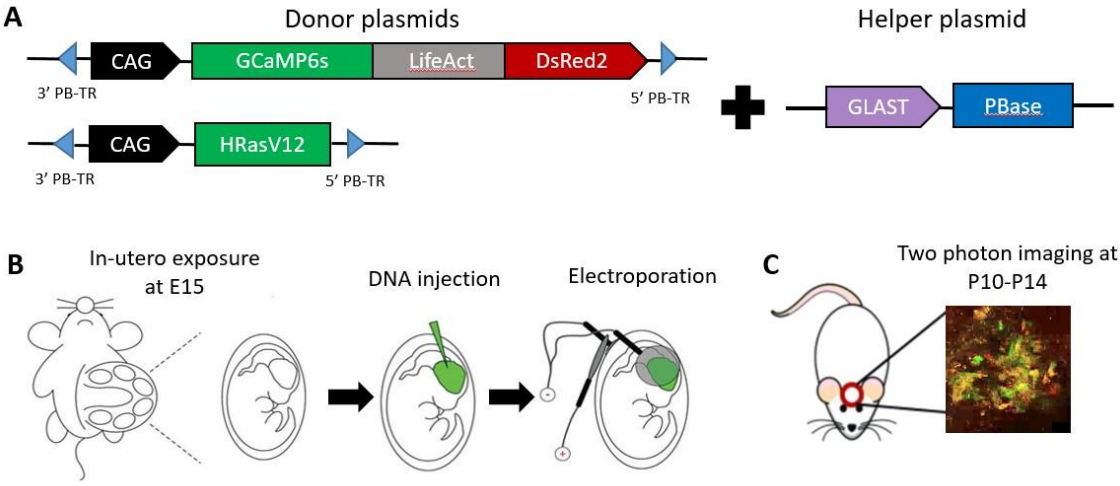

D

IUE Day	Neurons	Astrocytes
E13	79.8 ± 3.3 %	20.2 ± 3.3 %
E15	**26.6 ± 2.7 %**	**73.4 ± 2.7 %**

Figure 4.2: Spontaneous GBM mouse model. **A)** Plasmid constructs with two donor plasmids (a plasmid with two fluorescent reporters and a plasmid with the oncogene, HRasV12) and a helper plasmid, GLAST-PBase. The fluorescent reporters are composed of a genetically encoded calcium indicator GCaMP6s (green) and LifeAct-DsRed2 (red), staining the actin cytoskeleton. **B)** Graphical representation of *in utero* electroporation (IUE) protocol. Plasmids were injected into the visual cortex of the fetus at embryonic age 15 (E15) and electroporated. **C)** Two photon imaging were done on pups at postnatal day 10 to 14 (P10-P14). **D)** Table showing the percentage of neuron and astrocytes targeted when IUE is performed at E13 and E15. Text in red represents the preferred age for IUE in our spontaneous GBM model.

Clinical evidence has shown that different genetic mutations results in different types of tumor including central nervous system (CNS) tumor types. According to the study published by Hertwig and colleagues, 2 out of 3 animals that were transduced with HRasV12 alone resulted in the formation of tumors that are very aggressive and resembles the human giant cell glioblastoma (170). This is in line with the results obtained from our tumor model. We successfully generated an aggressive and invasive tumor phenotype, which can be seen from the infiltration of the tumor up to 300 µm into the cortex (Figure 4.3). Figure 4.4A shows tumor cells in red that were imaged at two different depths of a P10 pup. Collagen fibers in green could be seen more prominently at the superficial layer of the brain. These images unravel an elongated or 'mesenchymal' morphological phenotype of the tumor cells. It is known that metastasis and infiltration potential highly depends on the morphological characteristics of tumor cells. Tumor cells may regulate between rounded to elongated shape in response to the microenvironment (146). In a study published by Lyons et al., it is reported that highly metastatic osteosarcoma cells are 19% more elongated than the low metastatic cells (171). This characteristics of tumor cells are also supported by our previous data on GL261 model, where cells at the peripheral region are more elongated in shape and portray

higher migratory capability compared to the rounded GL261 cells that populates the tumor mass.

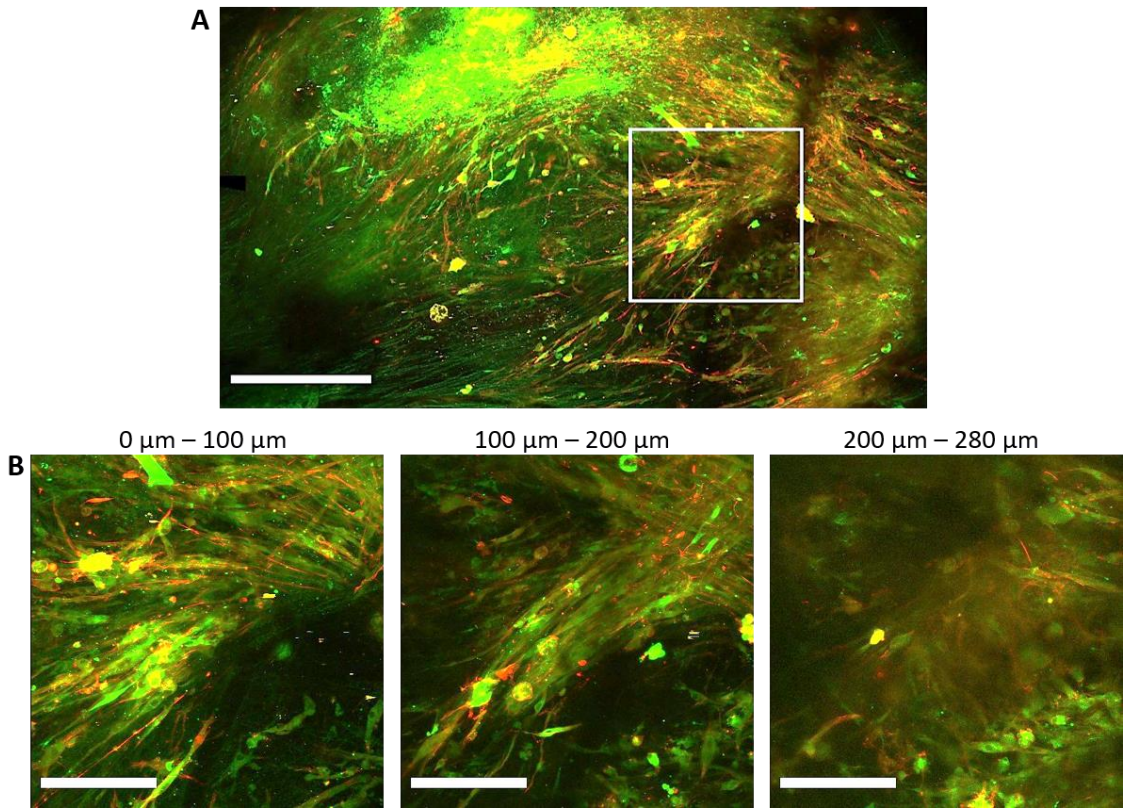

Figure 4.3: *In vivo* **spontaneous GBM tumor**. **A)** Mosaic image showing entire tumor area of a pup imaged at P13. Maximum projection of a stack imaged every 2 µm from the surface down to about 300 µm depth (scale bar 500 µm). Tumor cells can be seen in both green and red signals. Collagen fibers in green can be visualized at the bottom left corner of the image. The intense green signal at the top left side of the image is an artefact that could be due to high concentration of DNA at the electroporated site. **B)** Standard deviation projection of z-stack images collected along the extension in depth of an area of the tumor represented by the white square in A. Z-stack images were acquired with 2 µm step size (scale bar 200 µm).

Next, we performed intravital two photon $(Ca^{2+})_i$ imaging on our spontaneous GBM model. The functional versatility of Ca^{2+} ions in the brain has been extensively reviewed over the years, particularly in their involvement in cell-cell communication. This communication is secured by $(Ca^{2+})_i$ oscillation and waves (172). Our aim is observe *in vivo* $(Ca^{2+})_i$ activity of a developmental tumor and to prove that our spontaneous GBM model could be used for this purpose. In Figure 4.4B, we represented an example of $(Ca^{2+})_i$ traces of a group of 6 cells. The identified cells especially cell 2 to 6, seem to have $(Ca^{2+})_i$ waves propagating within cells producing synchronicity. This data looks promising for future work because similar coordinated $(Ca^{2+})_i$ activity was also observed in our GL261 model. We postulate that these tumor cells represent the infiltrating component of the tumor.

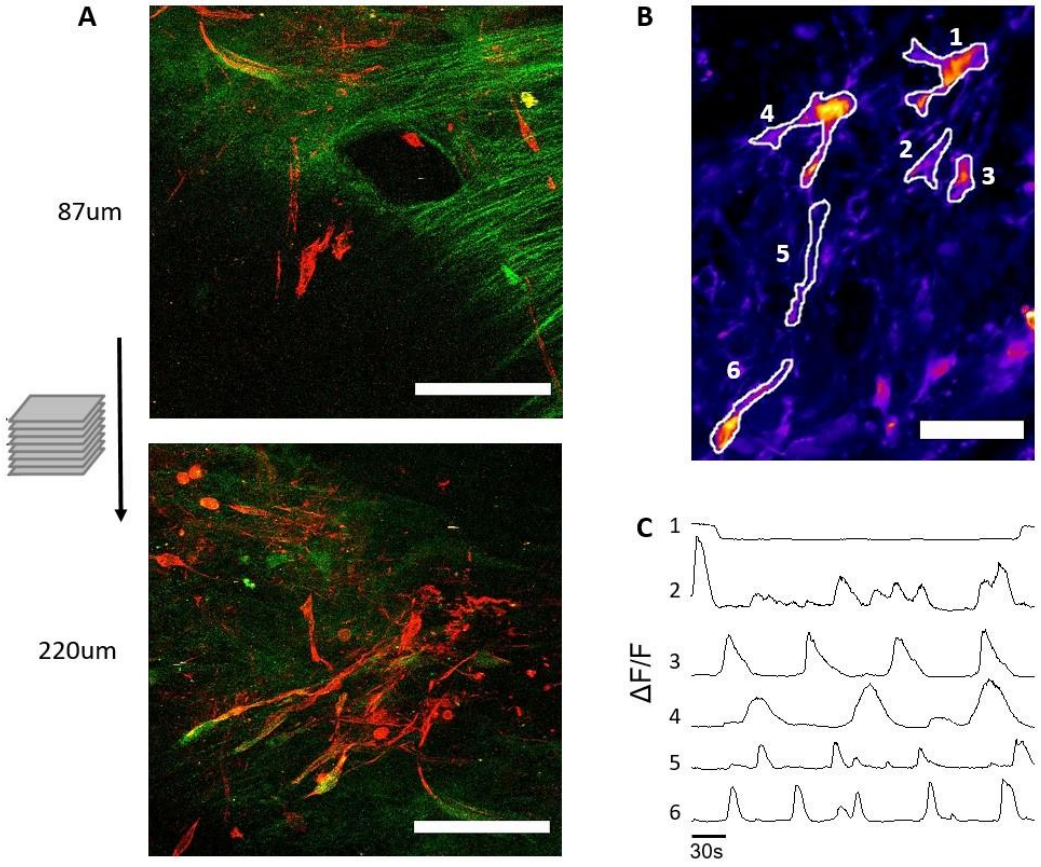

Figure 4.4: *In vivo* **two photon imaging**. **A)** Representative images of tumor cells at two different depths from the cortical surface (87 µm and 220 µm) taken at P10. Images are a maximum projection of a z-stack imaged every 5 µm from the surface down (scale bar 200 µm). The green fluorescent signal is due to second harmonic back scattering of collagen fibers (SHG) and in red are the tumor cells. **B)** Standard deviation projection of a 10 minutes' movie sequence at 47 µm depth from the surface with sampling period of 1.07s (scale bar 100 µm). **C)** Example traces of $(Ca^{2+})_i$ fluctuation for 6 tumor cells corresponding to white numbers in the image. Cells 2 to 6 appears to display a certain degree of co-activation.

Glioma cells infiltrate into the healthy brain through different mechanisms. The cells mainly migrate using preexisting structures like blood vessels or mylineated nerve fibers of white matter tracts (173). However, it is also known that fascin in filopodia and actin-based potrusions have been implicated in tumor infiltration and metastasis (174). Studies suggests that fascin promotes tumor invasiveness via its up-regulation when the tumor undergo epithelial to mesenchymal transition. However, the *in vivo* role of filopodia-based infiltration is yet to be fully understood (175, 176, 177). To better understand this mechanism, our tumor model allows us to temporally observe tumor cell migration especially via blood vessels and filopodia-based infiltration of tumor cells (Figure 4.5 and Figure 4.6). In Figure 4.5 our model shows a couple of tumor cells migrating along a blood vessel and these cells portray different migration patterns associated with their morphology. Elongated cells tend to migrate through 'arm-like' protrusions while circular tumor cells move as a whole with fewer protrusions. Figure 4.6 demonstrates how the tumor protrusions senses the surrounding environment and modifies its structure in an extending manner.

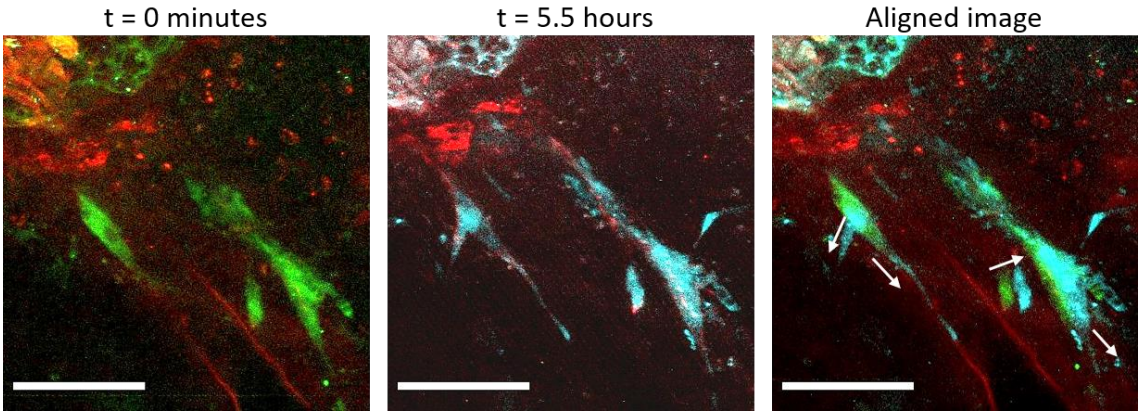

Figure 4.5: Tumor cell migration. Images on the left and middle represent maximum projection of a short z-stack (10 µm, with 2 µm step size) collected at 60–70 µm depth from the surface of a pup imaged chronically at P12. The acquisition area is focused on a few tumor cells to follow its migration over time. At time 0 minutes', tumor cells are represented in green and at time 5.5 hours, tumor cells are represented in cyan. Image on the right shows the aligned image of the two time points. Tumor cells exhibit different migration patterns and direction (white arrows) (scale bar 100 µm).

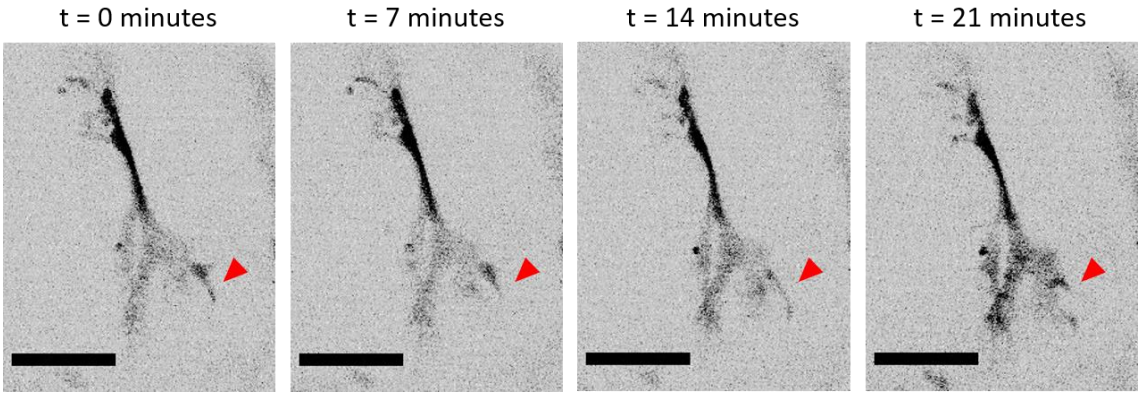

Figure 4.6: Observation of motility of tumor cell protrusions. Sequence of images representing the temporal evolution of protrusions of a tumor cell. The tumor cell modifies its protrusive structure (red arrows) projection at its leading edge over time while exploring its surrounding environment (scale bar 50 µm).

Finally, we did exploratory immunohistochemistry staining on the brain slices to characterize the type of tumor we produced in our model. We tested three different areas of the brain, which are the tumoral area, the edge of the tumor and the contralateral hemisphere. Fluorescence signals from GCaMP6s and DsRed2 were used to as a reference to make the area of the tumor. Since, glial fibrillary acidic protein, GFAP is a classical marker of astrocytomas and the loss of neuronal marker, NeuN expression is often associated with high grade gliomas, we tested the brain slices of a P13 treated pup against these two antibodies. Figure 4.7 demonstrates loss of NeuN expression and a higher percentage of GFAP positive staining in tumoral area. This difference can be seen clearly at the images taken at the border of the tumor. There is no NeuN expression at the tumor region, but across the border, positive NeuN expression can be seen. Additionally, GFAP positive staining seem to be higher in the tumoral

area and weaker in the tumor-free region. This results, is the initial validation that our spontaneous model resembles the GBM tumor.

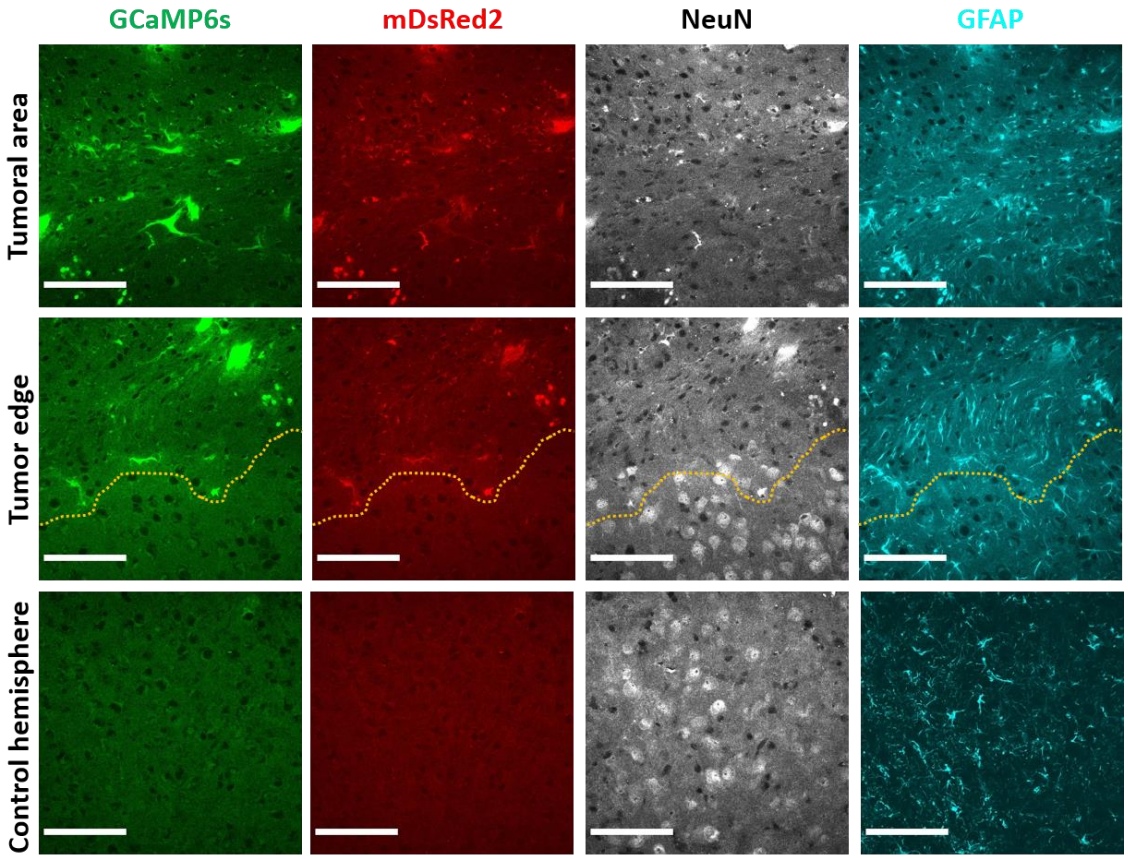

Figure 4.7: Immunohistochemistry of spontaneous GBM tumor. GCaMP6s and mDsRed2 signals from tumor cells are used as a reference to indicate regions of the tumor. Yellow line represents the edge of the tumor. Positive immunohistochemical stains of NeuN and GFAP were done on the tumoral region, tumor edge and the contralateral hemisphere (control hemisphere). NeuN staining demonstrates neuron loss and higher GFAP-positive staining indicates reactive astrocytes in the tumor regions. In the control cortical hemisphere, there is positive NeuN and relatively weaker GFAP immunostaining.

4.3 Conclusion

The genetic and epigenetic understanding of GBM are steadily expanding especially due to increased appreciation of intratumoral heterogeneity that is often responsible for differential treatment responses of the different tumor districts. Here we demonstrated a model that allows us to follow the development of GBM from its endogenous state and our hypothesis on the correlation between calcium signaling and tumor invasiveness could be a new target for therapeutic advancement. We are optimistic that future work in this direction will strengthen our hypothesis and probably demonstrate new *in vivo* discoveries.

4.4 Method

4.4.1 Plasmids

A system of piggyBac transposon donor and helper plasmids were used in this study. The donor plasmids were PBCAG-HRasV12 and GCaMP6s-P2A-mDsRed2 while the helper plasmid was GLAST-PBase. Plasmids were used at 1:1:1 ratio. PBCAG-HRasV12 and GLAST-PBase was given to us by LoTurco Lab, University of Connecticut, USA (163).

4.4.2 Animals

See Chapter 3, Section 3.4.5.

4.4.3 *In utero* electroporation

Tripolar *in utero* electroporation targeting radial glial cells of the visual cortex was performed as previously described (178, 179). The day of mating (limited to 4 h in the morning) was defined as the embryonic day zero (E0) and the day of birth was defined as postnatal day zero (P0). Timed-pregnant C57BL/6 mice at E15 were anesthetized with isoflurane (induction, 4%; surgery, 2%), and the uterine horns were exposed by laparotomy. DNA (2 μg/μL in water) was mixed with the dye Fast Green (0.3 mg/mL Sigma, St Louis, MO, USA) and was injected (~ 5 μL) through the uterine wall into one of the lateral ventricles of each embryos by a 30-gauge needle (Pic indolor, Grandate, Italy). After soaking the uterine horn with a pre-warmed phosphate-buffered saline (PBS) solution, the embryo's head was carefully held between tweezer-type circular electrodes (10 mm diameter), while a third electrode (7×6×1 mm, gold-plated copper) was positioned at 90°, targeting the visual cortex. Electroporation was conducted with five electrical pulses (amplitude, 50 V; duration, 50 ms; intervals, 150 ms) using a square-wave electroporation generator (CUY21EDIT, Nepa Gene; ECM 830, BTX, Harvard Apparatus). The uterine horns were returned into the abdominal cavity, and embryos continued their normal development until delivery.

Survival rate after electroporation was 69% and electroporation was effective in more than 83% of the surviving treated animals.

4.4.4 Cranial window surgery

See Chapter 3, Section 3.4.8.

4.4.5 *In-vivo* two-photon microscopy

See Chapter 3, Section 3.4.9.

4.4.6 Immunohistochemistry

Brains of animals were removed and fixed with 4% paraformaldehyde/PBS (4% PFA). Prior to sectioning, samples were treated 30% sucrose solution for one week. The day of sectioning, isopentane was cooled at -80 ◦C for 30 minutes'. Then samples were frozen by placing them directly into the cold isopentane and refrigerated for 5-10 minutes'. Once samples were frozen, they were fixed in an optimal cutting temperature compound (Tissue-Tek; Sakura Finetek USA) and kept at -20 ◦C to equilibrate for an hour. Brains were then sectioned at 60 µm thickness on a cryostat (Leica CM1520). Sections were processed as free-floating sections and stained with, 1:100 αGFAP (Abcam, ab7260) and 1:100 αNeuN (Sigma-Aldrich, MAB377) antibodies. Secondary immunostainings were performed using 1:500 Alexa Fluor conjugates secondary antibodies (Abcam AF405, AF647).

4.4.7 Confocal image acquisition of brain slices

Fixed tissue was imaged with the Zeiss LSM-800 Airyscan confocal microscope with 405/ 488/ 561/ 640 nm lasers according to the secondary antibody and fluorescent reporters of the sample. Images were acquired using a 40X oil objective (NA 1.3).

Chapter 5

Summary and Future Perspectives

5.1 Summary

This dissertation is focused in two main parts: First, I evaluated *in vivo* $(Ca^{2+})_i$ activity and its correlation with tumor migration in a well-established GBM animal model (GL261 model); Second, I started moving towards a more human-like GBM mouse model (i.e. developmental model) using current molecular techniques. Results of this study are divided into two chapters:

Chapter 3. Here, I first produced a GL261 fluorescent animal model with genetically encoded calcium sensor (GCaMP6s). Exploiting two photon imaging technique, I managed to characterized the $(Ca^{2+})_i$ activity of tumor cells populating two different regions of the tumor. Then, I established a positive correlation between $(Ca^{2+})_i$ activity and tumor cell migration capability. While performing the experiments, I made a novel observation of cellular cluster activation. I briefly analyzed this group of highly synchronized cells for its migrational properties and found that cells in these clusters display a direction-biased motility. Data from this study, to my knowledge, is the first quantitative evaluation of *in vivo* intratumoral Ca^{2+} signaling.

Chapter 4. I utilized the *piggyBac* IUE approach to induce spontaneous brain tumor by over expressing the oncogene HRasV12. Expression of HRasV12 controlled by ubiquitous CAG promoter in *piggyBac* donor plasmids, induced GBM in mice. Resulting tumor displays an aggressive and infiltrative phenotype that closely resembles the human GBM. Preliminary results shows promising potential to study intratumoral $(Ca^{2+})_i$ activity and migration patterns in a developmental tumor.

5.2 Unsolved issues

GL261 Model

1. We quantified intratumoral Ca^{2+} activity and established its correlation with tumor cell migration. However, these experiments do not provide information regarding the Ca^{2+} channels involved. Identifying and interfering with these channels using pharmacological or genetic manipulation while observing its involvement in cellular migration would be the next step.

2. The observed highly synchronized cluster activation could be a new unexplored phenomenon that highlights possible and promising directions for future therapeutic target in treating GBM. Therefore, further characterization and evaluation is required in this direction.

Spontaneous GBM Model

1. The developmental tumor model displays distinct differences in aggressiveness, tumor growth pattern and cellular morphology compared to the GL261 model. Preliminary results presents as a proof of concept that this model is functional as an experimental model. Additional work is needed to characterize and analyse this animal model.

2. Since the resulting tumor grows rapidly and is very aggressive, mortality rate of the animals is very low. Furthermore, treated animals were unable to recover from anesthesia. This is a limitation of this model and a new strategy for inducing oncogenesis at a later age could be employed to overcome this issue.

5.3 Future perspectives

Tracking intratumoral heterogeneity using RNA sequencing. Current state of the art molecular techniques such as RNA sequencing enables us to reveal and quantify level of gene expression in the continuously changing cellular transcriptome. It is particularly useful in the study of tumor heterogeneity in GBM (180). In our study, this technique enables an unbiased gene expression profile of GBM cell population coming from different regions of the tumor. We postulate that cells from peripheral region and tumor mass have heterogeneous expression of Ca^{2+} channels and other regulator of Ca^{2+} homeostasis that contributes to their differential $(Ca^{2+})_i$ activity. This profiling, if done, will help us to identify and interfere with the Ca^{2+} channels involved in GBM cell proliferation and migration.

ddGCaMP: A new tool for intracellular calcium imaging. Ca^{2+} imaging is a powerful tool to study changes in intracellular signaling at a single cell level. In oncology, it proves to be instrumental in providing information that drives tumor progression. However, Ca^{2+} sensors like GCaMP6s binds with Ca^{2+} ions to tranduce changes in cellular Ca^{2+} into changes in fluorescence. By binding with Ca^{2+} ions, the sensor acts as a buffer, that could reduce magnitude of actual Ca^{2+} changes and producing a proportional slowing of the rates of change (181). Prolonged expression of GCaMP is harmful especially during development (182). Thus, to overcome this issue, our lab produced a version of GCaMP that is fused with a destabilization domain causing rapid degradation of the protein. The expression of the sensor can be activated by introducing trimethoprim (TMP) to suppress the protein degradation (Figure 5.1). TMP is an antibiotic molecule that penetrates the blood brain barrier (183). In this way, we are able to switch 'on' the Ca^{2+} sensor by providing TMP via intraperitoneal

injection an hour before imaging sessions. The expression of the sensor returns to basal level a few hours post TMP. This tool can be used to reduce the side effects of Ca^{2+} buffering because it limits the expression of the sensor to a small time window, which is critical in our developmental tumor model where Ca^{2+} plays a crucial role in the development of the cortex. However, suitable control experiments must be performed, such as evaluating brain activity by performing electrophysiology experiments on animals with and without TMP, to exclude potential side effects of TMP on the signaling system under study.

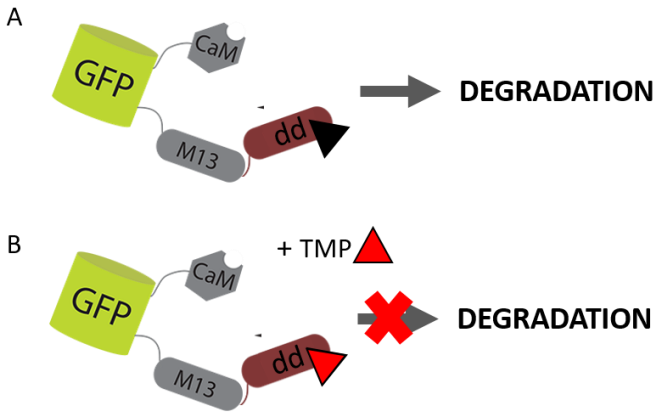

Figure 5.1: ddGCaMP: GCaMP with a destabilization domain. **A)** A destabilization domain (dd) is introduced to the M13 peptide of myosin light chain kinase. This dd domain causes degradation of the protein and therefore the sensor does not bind with calcium ions and go through conformational changes that activates the sensor. **B)** Addition of an antibiotic, trimethoprim (TMP, red triangle) neutralizes the dd domain and rapidly stops degradation of the protein and allows the expression of the sensor.

Induce oncogenesis at different time points. A major disadvantage of our spontaneous GBM model is that tumor initiation and growth cannot be controlled. *Beatrix* is a tool that has been designed in our lab for the study of mosaicism in neurodevelopmental diseases. This tool when electroporated *in utero* allows the creation of focal mosaic of expression (184). By modifying *Beatrix* as shown in Figure 5.2, oncogenesis in electroporated mice can be induced at later age after birth (its mechanism of action is briefly explained in the following paragraph). Animal model generated with this modified tool, will be the ideal representation of GBM animal model that closely resembles the human pathology.

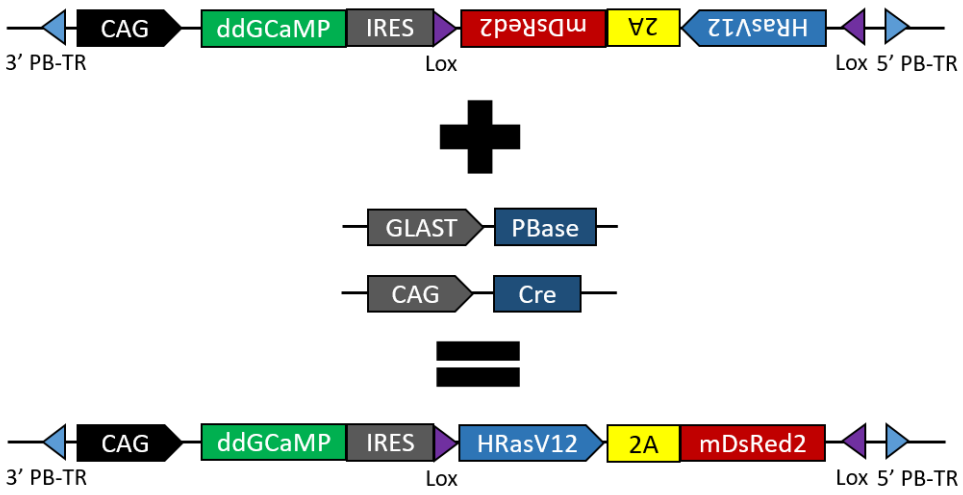

Figure 5.2: Modified Beatrix sensor with piggyBac integration system (simplified). The donor plasmid expresses the calcium sensor, ddGCaMP in sense configuration and oncogene, HRasV12 and red fluorescent protein, mDsRed2 in antisense configuration. The IRES and 2A sequence are needed for the simultaneous expression of the proteins flanking them. GLAST-PBase (helper plasmid) is necessary for stable integration of the donor sequence into radial glial progenitors. CAG-Cre plasmid is the activator and upon administration, drives oncogenesis by changing the antisense configuration of HRasV12 and mDsRed2 to sense configuration.

Mechanism of action: *In utero* electroporation of donor and helper plasmid at embryonic age 15 (E15) will integrate the plasmid system into the genome of the fetus. Oncogenesis can be introduced, for example at postnatal day 30 (P30), by intracortical injection of Cre recombinase. In this model, administration of Cre will be in a diluted concentration so that only a subset of cells will receive the Cre activator. Imaging experiments can be done ideally, as early as 1 week after tumor induction and ddGCaMP sensor can be activated (by administrating TMP) during experimental procedures. In this way, the mutated cells will express: 1) ddGCaMP, 2) HRasV12 and 3) DsRed2 resulting a yellow fluorescence signal. By contrast, non-mutated cells will express green fluorescence signal due to the calcium sensor, ddGCaMP. In this way we will monitor intracellular signaling in both mutated and normal astrocytes.

Bibliography

[1] J. C. Buckner, P. D. Brown, B. P. O'Neill, F. B. Meyer, C. J. Wetmore, and J. H. Uhm, "Central nervous system tumors," in *Mayo Clinic Proceedings*, vol. 82, no. 10. Elsevier, 2007, pp. 1271–1286, doi: 10.4065/82.10.1271.

[2] D. N. Louis, P. Wesseling, K. Aldape, D. J. Brat, D. Capper, I. A. Cree, C. Eberhart, D. Figarella-Branger, M. Fouladi, G. N. Fuller *et al.*, "cimpact-now update 6: new entity and diagnostic principle recommendations of the cimpact-utrecht meeting on future cns tumor classification and grading," *Brain Pathology*, 2020, doi: 10.1111/ bpa.12832.

[3] A. Gupta and T. Dwivedi, "A simplified overview of world health organization classification update of central nervous system tumors 2016," *Journal of neurosciences in rural practice*, vol. 8, no. 4, p. 629, 2017, doi: 10.4103/jnrp.jnrp 168 17.

[4] J. Bai, J. Varghese, and R. Jain, "Adult glioma who classification update, genomics, and imaging: What the radiologists need to know," *Topics in Magnetic Resonance Imaging*, vol. 29, no. 2, pp. 71–82, 2020, doi: 10.1097/RMR.0000000000000234.

[5] Q. T. Ostrom, G. Cioffi, H. Gittleman, N. Patil, K. Waite, C. Kruchko, and J. S. Barnholtz-Sloan, "Cbtrus statistical report: primary brain and other central nervous system tumors diagnosed in the united states in 2012–2016," *Neuro-oncology*, vol. 21, no. Supplement 5, pp. v1–v100, 2019, doi: 10.1093/neuonc/noz150.

[6] D. N. Louis, A. Perry, G. Reifenberger, A. Von Deimling, D. Figarella-Branger, W. K. Cavenee, H. Ohgaki, O. D. Wiestler, P. Kleihues, and D. W. Ellison, "The 2016 world health organization classification of tumors of the central nervous system: a summary," *Acta neuropathologica*, vol. 131, no. 6, pp. 803–820, 2016, doi: 10.1007/ s00401-016-1545-1.

[7] O. G. Taylor, J. S. Brzozowski, and K. A. Skelding, "Glioblastoma multiforme: An overview of emerging therapeutic targets," *Frontiers in oncology*, vol. 9, p. 963, 2019, doi: 10.3389/fonc.2019.00963.

[8] M. D. Prados, S. A. Byron, N. L. Tran, J. J. Phillips, A. M. Molinaro, K. L. Ligon, P. Y. Wen, J. G. Kuhn, I. K. Mellinghoff, J. F. De Groot *et al.*, "Toward precision medicine in glioblastoma: the promise and the challenges," *Neuro-oncology*, vol. 17, no. 8, pp. 1051–1063, 2015, doi: 10.1093/neuonc/nov031.

[9] K. Kallenberg, T. Goldmann, J. Menke, H. Strik, H. Bock, F. Stockhammer, J. Buhk, J. Frahm, P. Dechent, and M. Knauth, "Glioma infiltration of the corpus callosum: early signs detected by dti," *Journal of Neuro-Oncology*, vol. 112, no. 2, pp. 217–222, 2013, doi: 10.1007/s11060-013-1049-y.

[10] M. Preusser, S. De Ribaupierre, A. W¨ohrer, S. C. Erridge, M. Hegi, M. Weller, and R. Stupp, "Current concepts and management of glioblastoma," *Annals of neurology*, vol. 70, no. 1, pp. 9–21, 2011, doi: 10.1002/ana.22425.

[11] T. Chouleur, M. L. Tremblay, and A. Bikfalvi, "Mechanisms of invasion in glioblastoma," *Current Opinion in Oncology*, vol. 32, no. 6, pp. 631–639, 2020, doi: 10.1097/CCO.0000000000000679.

[12] H. Scherer, "Structural development in gliomas," *The American Journal of Cancer*, vol. 34, no. 3, pp. 333–351, 1938, doi: 10.1158/ajc.1938.333.

[13] G. S. Stoyanov, L. Petkova, and D. L. Dzhenkov, "Hans joachim scherer and his impact on the diagnostic, clinical, and modern research aspects of glial tumors," *Cureus*, vol. 11, no. 11, 2019, doi: 10.7759/cureus.6148.

[14] P. G. Gritsenko, O. Ilina, and P. Friedl, "Interstitial guidance of cancer invasion," *The Journal of pathology*, vol. 226, no. 2, pp. 185–199, 2012, doi: 10.1002/path.3031.

[15] T. Simon, E. Jackson, and G. Giamas, "Breaking through the glioblastoma microenvironment via extracellular vesicles," *Oncogene*, pp. 1–14, 2020, doi: 10.1038/s41388-020-1308-2.

[16] A. Vollmann-Zwerenz, V. Leidgens, G. Feliciello, C. A. Klein, and P. Hau, "Tumor cell invasion in glioblastoma," *International Journal of Molecular Sciences*, vol. 21, no. 6, p. 1932, 2020, doi: 10.3390/ijms21061932.

[17] A. Yekula, A. Yekula, K. Muralidharan, K. Kang, B. S. Carter, and L. Balaj, "Extracellular vesicles in glioblastoma tumor microenvironment," *Frontiers in immunology*, vol. 10, p. 3137, 2020, doi: 10.3389/fimmu.2019.03137.

[18] S. C. Lee, C. Deutsch, and W. T. Beck, "Comparison of ion channels in multidrugresistant and-sensitive human leukemic cells," *Proceedings of the National Academy of Sciences*, vol. 85, no. 6, pp. 2019–2023, 1988, doi: 10.1073/pnas.85.6.2019.

[19] S. Batra and J. Alenfall, "Effect of diverse categories of drugs on human colon tumour cell proliferation." *Anticancer research*, vol. 11, no. 3, pp. 1221–1224, 1991, pmid: 10.1073/pnas.85.6.2019.

[20] J. Pancrazio, I. Tabbara, and Y. Kim, "Voltage-activated k+ conductance and cell proliferation in small-cell lung cancer." *Anticancer research*, vol. 13, no. 4, pp. 1231–1234, 1993, pmid: 8394676.

[21] N. Prevarskaya, R. Skryma, and Y. Shuba, “Ion channels and the hallmarks of cancer,” *Trends in molecular medicine*, vol. 16, no. 3, pp. 107–121, 2010, doi: 10.1016/j.molmed.2010.01.005.

[22] D. J. Blackiston, K. A. McLaughlin, and M. Levin, “Bioelectric controls of cell proliferation: ion channels, membrane voltage and the cell cycle,” *Cell cycle*, vol. 8, no. 21, pp. 3527–3536, 2009, doi: 10.4161/cc.8.21.9888.

[23] T. J. Jentsch, “Vracs and other ion channels and transporters in the regulation of cell volume and beyond,” *Nature Reviews Molecular Cell Biology*, vol. 17, no. 5, pp. 293–307, 2016, doi: 10.1038/nrm.2016.29.

[24] J. Kulbacka, A. Choroman´ska, J. Rossowska, J. Wez˙gowiec, J. Saczko, and M.-P. Rols, “Cell membrane transport mechanisms: ion channels and electrical properties of cell membranes,” in *Transport across natural and modified biological membranes and its implications in physiology and therapy*. Springer, 2017, pp. 39–58, doi: 10.1007/ 978-3-319-56895-9 _3.

[25] F. Lang and C. Stournaras, “Ion channels in cancer: future perspectives and clinical potential,” *Philosophical Transactions of the Royal Society B: Biological Sciences*, vol. 369, no. 1638, p. 20130108, 2014, doi: 10.1098/rstb.2013.0108.

[26] M. Nakada, S. Nakada, T. Demuth, N. Tran, D. Hoelzinger, and M. Berens, “Molecular targets of glioma invasion,” *Cellular and molecular life sciences*, vol. 64, no. 4, p. 458, 2007, doi: 10.1007/s00018-007-6342-5.

[27] C. Leclerc, M. Moreau, and I. N´eant, “The calcium: an early signal that initiates the formation of the nervous system during embryogenesis,” *Frontiers in molecular neuroscience*, vol. 5, p. 64, 2012, doi: 10.3389/fnmol.2012.00064.

[28] M. J. Berridge, P. Lipp, and M. D. Bootman, “The versatility and universality of calcium signalling,” *Nature reviews Molecular cell biology*, vol. 1, no. 1, pp. 11–21, 2000, doi: 10.1038/35036035.

[29] M. J. Berridge, M. D. Bootman, and H. L. Roderick, “Calcium signalling: dynamics, homeostasis and remodelling,” *Nature reviews Molecular cell biology*, vol. 4, no. 7, pp. 517–529, 2003, doi: 10.1038/nrm1155.

[30] D. E. Clapham, “Calcium signaling,” *Cell*, vol. 131, no. 6, pp. 1047–1058, 2007, doi: 10.1016/j.cell.2007.11.028.

[31] K. Mikoshiba, “Ip3 receptor/ca2+ channel: from discovery to new signaling concepts,” *Journal of neurochemistry*, vol. 102, no. 5, pp. 1426–1446, 2007, doi: 10.1111/ j.1471-4159.2007.04825.x.

[32] J. Parkash and K. Asotra, “Calcium wave signaling in cancer cells,” *Life sciences*, vol. 87, no. 19-22, pp. 587–595, 2010, doi: 10.1016/j.lfs.2010.09.013.

[33] O. Rey, S. H. Young, R. Jacamo, M. P. Moyer, and E. Rozengurt, “Extracellular calcium sensing receptor stimulation in human colonic epithelial cells induces intracellular calcium oscillations and proliferation inhibition,” *Journal of cellular physiology*, vol. 225, no. 1, pp. 73–83, 2010, doi: 10.1002/jcp.22198.

[34] N. Prevarskaya, R. Skryma, and Y. Shuba, “Targeting ca2+ transport in cancer: close reality or long perspective?” *Expert opinion on therapeutic targets*, vol. 17, no. 3, pp. 225–241, 2013, doi: 10.1517/14728222.2013.741594.

[35] A. Maklad, A. Sharma, and I. Azimi, “Calcium signaling in brain cancers: roles and therapeutic targeting,” *Cancers*, vol. 11, no. 2, p. 145, 2019, doi: 10.3390/ cancers11020145.

[36] W. A. Catterall and A. P. Few, “Calcium channel regulation and presynaptic plasticity,” *Neuron*, vol. 59, no. 6, pp. 882–901, 2008, doi: 10.1016/j.neuron.2008.09.005.

[37] S. S. Rosenberg and N. C. Spitzer, “Calcium signaling in neuronal development,” *Cold Spring Harbor perspectives in biology*, vol. 3, no. 10, p. a004259, 2011, doi: 10.1101/cshperspect.a004259.

[38] R. D. Burgoyne and L. P. Haynes, “Understanding the physiological roles of the neuronal calcium sensor proteins,” *Molecular brain*, vol. 5, no. 1, p. 2, 2012, doi: 10.1186/1756-6606-5-2.

[39] G. Zu¨ndorf and G. Reiser, “Calcium dysregulation and homeostasis of neural calcium in the molecular mechanisms of neurodegenerative diseases provide multiple targets for neuroprotection,” *Antioxidants & redox signaling*, vol. 14, no. 7, pp. 1275–1288, 2011, doi: 10.1089/ars.2010.3359.

[40] P. Marambaud, U. Dreses-Werringloer, and V. Vingtdeux, “Calcium signaling in neurodegeneration,” *Molecular neurodegeneration*, vol. 4, no. 1, pp. 1–15, 2009, doi: 10.1186/1750-1326-4-20.

[41] V. A. Cuddapah and H. Sontheimer, “Ion channels and transporters (corrected) in cancer. 2. ion channels and the control of cancer cell migration.” *American journal of physiology. Cell physiology*, vol. 301, no. 3, pp. C541–9, 2011, doi: 10.1152/ajpcell. 00102.2011.

[42] J. Haiech, E. Audran, M. F`eve, R. Ranjeva, and M.-C. Kilhoffer, “Revisiting intracellular calcium signaling semantics,” *Biochimie*, vol. 93, no. 12, pp. 2029–2037, 2011, doi: 10.1016/j.biochi.2011.05.003.

[43] N. Robil, F. Petel, M.-C. Kilhoffer, and J. Haiech, “Glioblastoma and calcium signaling-analysis of calcium toolbox expression,” *Int. J. Dev. Biol*, vol. 59, pp. 407– 415, 2015, doi: 10.1387/ijdb.150200jh.

[44] F. B. Morrone, M. P. Gehring, and N. F. Nicoletti, “Calcium channels and associated receptors in malignant brain tumor therapy,” *Molecular pharmacology*, vol. 90, no. 3, pp. 403–409, 2016, doi: 10.1124/mol.116.103770.

[45] H. A. Dbouk, R. M. Mroue, M. E. El-Sabban, and R. S. Talhouk, “Connexins: a myriad of functions extending beyond assembly of gap junction channels,” *Cell Communication and signaling*, vol. 7, no. 1, pp. 1–17, 2009, doi: 10.1186/1478-811X-7-4.

[46] D. W. Laird, “Life cycle of connexins in health and disease,” *Biochemical Journal*, vol. 394, no. 3, pp. 527–543, 2006, doi: 10.1042/BJ20051922.

[47] M. Mesnil, S. Crespin, J.-L. Avanzo, and M.-L. Zaidan-Dagli, “Defective gap junctional intercellular communication in the carcinogenic process,” *Biochimica et Biophysica Acta (BBA)-Biomembranes*, vol. 1719, no. 1-2, pp. 125–145, 2005, doi: 10.1016/j.bbamem.2005.11.004.

[48] S. Cottin, P. Gould, L. Cantin, and M. Caruso, “Gap junctions in human glioblastomas: implications for suicide gene therapy,” *Cancer gene therapy*, vol. 18, no. 9, pp. 674–681, 2011, doi: 10.1038/cgt.2011.38.

[49] E. Dere and A. Zlomuzica, “The role of gap junctions in the brain in health and disease,” *Neuroscience & Biobehavioral Reviews*, vol. 36, no. 1, pp. 206–217, 2012, doi: 10.1016/j.neubiorev.2011.05.015.

[50] W. Zhang, W. T. Couldwell, M. F. Simard, H. Song, J. H. Lin, and M. Nedergaard, “Direct gap junction communication between malignant glioma cells and astrocytes,” *Cancer research*, vol. 59, no. 8, pp. 1994–2003, 1999, pmid: 10213512.

[51] V. Nimmrich and G. Gross, “P/q-type calcium channel modulators,” *British journal of pharmacology*, vol. 167, no. 4, pp. 741–759, 2012, doi: 10.1111/j.1476-5381.2012. 02069.x.

[52] H. Dong, X.-W. Zhou, X. Wang, Y. Yang, J.-W. Luo, Y.-H. Liu, and Q. Mao, “Complex role of connexin 43 in astrocytic tumors and possible promotion of gliomaassociated epileptic discharge,” *Molecular medicine reports*, vol. 16, no. 6, pp. 7890– 7900, 2017, doi: 10.3892/mmr.2017.7618.

[53] Z. Sheng, “Connexin 43 peptidic medicine for glioblastoma stem cells,” *EBioMedicine*, vol. 64, 2021, doi: 10.1016/j.ebiom.2020.103205.

[54] G. Santoni, M. Santoni, and M. Nabissi, “Functional role of t-type calcium channels in tumour growth and progression: prospective in cancer therapy,” *British journal of pharmacology*, vol. 166, no. 4, pp. 1244–1246, 2012, doi: 10.1111/j.1476-5381.2012.01908.x.

[55] Y. Zhang, J. Zhang, D. Jiang, D. Zhang, Z. Qian, C. Liu, and J. Tao, “Inhibition of t-type ca2+ channels by endostatin attenuates human glioblastoma cell proliferation and migration,” *British journal of pharmacology*, vol. 166, no. 4, pp. 1247–1260, 2012, doi: 10.1111/j.1476-5381.2012.01852.x.

[56] N. C. Valerie, B. Dziegielewska, A. S. Hosing, E. Augustin, L. S. Gray, D. L. Brautigan, J. M. Larner, and J. Dziegielewski, “Inhibition of t-type calcium channels disrupts akt signaling and promotes apoptosis in glioblastoma cells,” *Biochemical pharmacology*, vol. 85, no. 7, pp. 888–897, 2013, doi: 10.1016/j.bcp.2012.12.017.

[57] Y. Zhang, N. Cruickshanks, F. Yuan, B. Wang, M. Pahuski, J. Wulfkuhle, I. Gallagher, A. F. Koeppel, S. Hatef, C. Papanicolas *et al.*, “Targetable t-type calcium channels drive glioblastoma,” *Cancer research*, vol. 77, no. 13, pp. 3479–3490, 2017, doi: 10.1158/0008-5472.CAN-16-2347.

[58] A. Visa, M. C. Sall´an, O. Maiques, L. Alza, E. Talavera, R. L´opez-Ortega, M. Santacana, J. Herreros, and C. Cant´ı, “T-type cav3. 1 channels mediate progression and chemotherapeutic resistance in glioblastoma,” *Cancer research*, vol. 79, no. 8, pp. 1857–1868, 2019, doi: 10.1158/0008-5472.CAN-18-1924.

[59] J. Chen, Y. Luan, R. Yu, Z. Zhang, J. Zhang, and W. Wang, “Transient receptor potential (trp) channels, promising potential diagnostic and therapeutic tools for cancer,” *Bioscience trends*, vol. 8, no. 1, pp. 1–10, 2014, doi: 10.5582/bst.8.1.

[60] Y. R. Park, J. N. Chun, I. So, H. J. Kim, S. Baek, J.-H. Jeon, and S.-Y. Shin, “Data-driven analysis of trp channels in cancer: linking variation in gene expression to clinical significance,” *Cancer Genomics-Proteomics*, vol. 13, no. 1, pp. 83–90, 2016, pmid: 26708603.

[61] C. Amantini, M. Mosca, M. Nabissi, R. Lucciarini, S. Caprodossi, A. Arcella, F. Giangaspero, and G. Santoni, “Capsaicin-induced apoptosis of glioma cells is mediated by trpv1 vanilloid receptor and requires p38 mapk activation,” *Journal of neurochemistry*, vol. 102, no. 3, pp. 977–990, 2007, doi: 10.1111/j.1471-4159.2007.04582.x.

[62] K. Stock, J. Kumar, M. Synowitz, S. Petrosino, R. Imperatore, E. S. J. Smith, P. Wend, B. Purfu¨rst, U. A. Nuber, U. Gurok *et al.*, “Neural precursor cells induce cell death of high-

grade astrocytomas through stimulation of trpv1," *Nature medicine*, vol. 18, no. 8, pp. 1232–1238, 2012, doi: 10.1038/nm.2827.

[63] M. Nabissi, M. B. Morelli, M. Santoni, and G. Santoni, "Triggering of the trpv2 channel by cannabidiol sensitizes glioblastoma cells to cytotoxic chemotherapeutic agents," *Carcinogenesis*, vol. 34, no. 1, pp. 48–57, 2013, doi: 10.1093/carcin/bgs328.

[64] M. Nabissi, M. B. Morelli, C. Amantini, V. Farfariello, L. Ricci-Vitiani, S. Caprodossi, A. Arcella, M. Santoni, F. Giangaspero, R. De Maria *et al.*, "Trpv2 channel negatively controls glioma cell proliferation and resistance to fas-induced apoptosis in erk-dependent manner," *Carcinogenesis*, vol. 31, no. 5, pp. 794–803, 2010, doi: 10.1093/carcin/bgq019.

[65] M. B. Morelli, M. Nabissi, C. Amantini, V. Farfariello, L. Ricci-Vitiani, S. Di Martino, R. Pallini, L. M. Larocca, S. Caprodossi, M. Santoni *et al.*, "The transient receptor potential vanilloid-2 cation channel impairs glioblastoma stem-like cell proliferation and promotes differentiation," *International journal of cancer*, vol. 131, no. 7, pp. E1067–E1077, 2012, doi: 10.1002/ijc.27588.

[66] V. C. Bomben and H. Sontheimer, "Disruption of transient receptor potential canonical channel 1 causes incomplete cytokinesis and slows the growth of human malignant gliomas," *Glia*, vol. 58, no. 10, pp. 1145–1156, 2010, doi: 10.1002/glia.20994.

[67] V. C. Bomben, K. L. Turner, T.-T. C. Barclay, and H. Sontheimer, "Transient receptor potential canonical channels are essential for chemotactic migration of human malignant gliomas," *Journal of cellular physiology*, vol. 226, no. 7, pp. 1879–1888, 2011, doi: 10.1002/jcp.22518.

[68] S. Li, J. Wang, Y. Wei, Y. Liu, X. Ding, B. Dong, Y. Xu, and Y. Wang, "Crucial role of trpc6 in maintaining the stability of hif-1α in glioma cells under hypoxia," *Journal of Cell Science*, vol. 128, no. 17, pp. 3317–3329, 2015, doi: 10.1242/jcs.173161.

[69] R. Wondergem and J. W. Bartley, "Menthol increases human glioblastoma intracellular ca 2+, bk channel activity and cell migration," *Journal of biomedical science*, vol. 16, no. 1, p. 90, 2009, doi: 10.1007/s10571-019-00776-3.

[70] T.-D. Leng, M.-H. Li, J.-F. Shen, M.-L. Liu, X.-B. Li, H.-W. Sun, D. Branigan, Z. Zeng, H.-F. Si, J. Li *et al.*, "Suppression of trpm 7 inhibits proliferation, migration, and invasion of malignant human glioma cells," *CNS neuroscience & therapeutics*, vol. 21, no. 3, pp. 252–261, 2015, doi: 10.1111/cns.12354.

[71] M. Alptekin, S. Eroglu, E. Tutar, S. Sencan, M. Geyik, M. Ulasli, A. Demiryurek, and C. Camci, "Gene expressions of trp channels in glioblastoma multiforme and relation with

survival," *Tumor Biology*, vol. 36, no. 12, pp. 9209–9213, 2015, doi: 10.1007/s13277-015-3577-x.

[72] G. Burnstock and F. Di Virgilio, "Purinergic signalling and cancer," *Purinergic signalling*, vol. 9, no. 4, pp. 491–540, 2013, doi: 10.1007/s11302-013-9372-5.

[73] W. Wei, J. K. Ryu, H. B. Choi, and J. G. McLarnon, "Expression and function of the p2x7 receptor in rat c6 glioma cells," *Cancer letters*, vol. 260, no. 1-2, pp. 79–87, 2008, doi: 10.1016/j.canlet.2007.10.025.

[74] J. Fang, X. Chen, L. Zhang, J. Chen, Y. Liang, X. Li, J. Xiang, L. Wang, G. Guo, B. Zhang *et al.*, "P2x7r suppression promotes glioma growth through epidermal growth factor receptor signal pathway," *The International Journal of Biochemistry & Cell Biology*, vol. 45, no. 6, pp. 1109–1120, 2013, doi: 10.1016/j.biocel.2013.03.005.

[75] M. P. Gehring, T. C. B. Pereira, R. F. Zanin, M. C. Borges, A. Braga Filho, A. M. O. Battastini, M. R. Bogo, G. Lenz, M. M. Campos, and F. B. Morrone, "P2x7 receptor activation leads to increased cell death in a radiosensitive human glioma cell line," *Purinergic signalling*, vol. 8, no. 4, pp. 729–739, 2012, doi: 10.1007/s11302-012-9319-2.

[76] M. P. Gehring, F. Kipper, N. F. Nicoletti, N. D. Sperotto, R. Zanin, A. S. Tamajusuku, D. G. Flores, L. Meurer, R. Roesler, B. Aroldo Filho *et al.*, "P2x7 receptor as predictor gene for glioma radiosensitivity and median survival," *The international journal of biochemistry & cell biology*, vol. 68, pp. 92–100, 2015, doi: 10.1016/j.biocel.2015.09. 001.

[77] E. Decrock, E. De Vuyst, M. Vinken, M. Van Moorhem, K. Vranckx, N. Wang, L. Van Laeken, M. De Bock, K. D'Herde, C. Lai *et al.*, "Connexin 43 hemichannels contribute to the propagation of apoptotic cell death in a rat c6 glioma cell model," *Cell Death & Differentiation*, vol. 16, no. 1, pp. 151–163, 2009, doi: 10.1038/cdd.2008.138.

[78] D. Buratto, V. Donati, F. Zonta, and F. Mammano, "Harnessing the therapeutic potential of antibodies targeting connexin hemichannels," *Biochimica et Biophysica Acta (BBA)-Molecular Basis of Disease*, vol. 1867, no. 4, p. 166047, 2021, doi: 10. 1016/j.bbadis.2020.166047.

[79] M. L. Cotrina, J. H.-C. Lin, A. Alves-Rodrigues, S. Liu, J. Li, H. Azmi-Ghadimi, J. Kang, C. C. Naus, and M. Nedergaard, "Connexins regulate calcium signaling by controlling atp release," *Proceedings of the National Academy of Sciences*, vol. 95, no. 26, pp. 15735–15740, 1998, doi: 10.1073/pnas.95.26.15735.

[80] W. Sin, Q. Aftab, J. Bechberger, J. Leung, H. Chen, and C. Naus, "Astrocytes promote glioma invasion via the gap junction protein connexin43," *Oncogene*, vol. 35, no. 12, pp. 1504–1516, 2016, doi: 10.1038/onc.2015.210.

[81] X.-Y. Ye, Q.-H. Jiang, T. Hong, Z.-Y. Zhang, R.-J. Yang, J.-Q. Huang, K. Hu, and Y.-P. Peng, "Altered expression of connexin43 and phosphorylation connexin43 in glioma tumors," *International journal of clinical and experimental pathology*, vol. 8, no. 5, p. 4296, 2015, pmid: 26191122.

[82] J. Wang, Z.-Y. Yang, Y.-F. Guo, J.-Y. Kuang, X.-W. Bian, and S.-C. Yu, "Targeting different domains of gap junction protein to control malignant glioma," *Neurooncology*, vol. 20, no. 7, pp. 885–896, 2018, doi: 10.1093/neuonc/nox207.

[83] G. Yusubalieva, V. Baklaushev, O. Gurina, M. Gulyaev, Y. A. Pirogov, and V. Chekhonin, "Antitumor effects of monoclonal antibodies to connexin 43 extracellular fragment in induced low-differentiated glioma," *Bulletin of experimental biology and medicine*, vol. 153, no. 1, pp. 163–169, 2012, doi: 10.1007/s10517-012-1667-y.

[84] S. G. Pelaz, M. Jara´ız-Rodr´ıguez, A. Alvarez-V´azquez, R. Talaver´on, L. Garc´ıa-´ Vicente, R. Flores-Hern´andez, M. G. de Cedr´on, M. Tabernero, A. R. de Molina, C. Lillo *et al.*, "Targeting metabolic plasticity in glioma stem cells in vitro and in vivo through specific inhibition of c-src by tat-cx43266-283," *EBioMedicine*, vol. 62, p. 103134, 2020, doi: 10.1016/j.ebiom.2020.103134.

[85] M. Jara´ız-Rodr´ıguez, M. D. Tabernero, M. Gonz´alez-Tablas, A. Otero, A. Orfao, J. M. Medina, and A. Tabernero, "A short region of connexin43 reduces human glioma stem cell migration, invasion, and survival through src, pten, and fak," *Stem cell reports*, vol. 9, no. 2, pp. 451–463, 2017, doi: 10.1016/j.stemcr.2017.06.007.

[86] S. Lamouille, J. W. Smyth, L. O'Rourke, P. Kanabur, S. Guo, J. Jourdan, Z. Sheng, and R. G. Gourdie, "Targeting glioblastoma cancer stem cells with a novel connexin43 mimetic peptide," 2017, doi: 10.1158/1538-7445.AM2017-4765.

[87] T. Mikkelsen, R. Lush, S. A. Grossman, K. A. Carson, J. D. Fisher, J. B. Alavi, and S. Rosenfeld, "Phase ii clinical and pharmacologic study of radiation therapy and carboxyamido-triazole (cai) in adults with newly diagnosed glioblastoma multiforme," *Investigational new drugs*, vol. 25, no. 3, pp. 259–263, 2007, doi: 10.1007/s10637-006-9023-6.

[88] D. Mahalingam, G. Wilding, S. Denmeade, J. Sarantopoulas, D. Cosgrove, J. Cetnar, N. Azad, J. Bruce, M. Kurman, V. Allgood *et al.*, "Mipsagargin, a novel thapsigarginbased psma-activated prodrug: results of a first-in-man phase i clinical trial in patients with refractory, advanced or metastatic solid tumours," *British journal of cancer*, vol. 114, no. 9, pp. 986–994, 2016, doi: 10.1038/bjc.2016.72.

[89] M. Holdhoff, X. Ye, J. G. Supko, L. B. Nabors, A. S. Desai, T. Walbert, G. J. Lesser, W. L. Read, F. S. Lieberman, M. A. Lodge *et al.*, "Timed sequential therapy of the selective t-

type calcium channel blocker mibefradil and temozolomide in patients with recurrent high-grade gliomas," *Neuro-oncology*, vol. 19, no. 6, pp. 845–852, 2017, doi: 10.1093/neuonc/nox020.

[90] A. Omuro, K. Beal, K. McNeill, R. J. Young, A. Thomas, X. Lin, R. Terziev, T. J. Kaley, L. M. DeAngelis, M. Daras *et al.*, "Multicenter phase ib trial of carboxyamidotriazole orotate and temozolomide for recurrent and newly diagnosed glioblastoma and other anaplastic gliomas," *Journal of clinical oncology*, vol. 36, no. 17, p. 1702, 2018, doi: 10.1200/JCO.2017.76.9992.

[91] M. Das, "Carboxyamidotriazole orotate in glioblastoma," *The Lancet Oncology*, vol. 19, no. 6, p. e292, 2018, doi: 10.1016/S1470-2045(18)30347-4.

[92] M. Griffin, R. Khan, S. Basu, and S. Smith, "Ion channels as therapeutic targets in high grade gliomas," *Cancers*, vol. 12, no. 10, p. 3068, 2020, doi: 10.3390/ cancers12103068.

[93] Y.-H. Kim, T. Kim, J.-D. Joo, J. H. Han, Y. J. Kim, I. A. Kim, C.-H. Yun, and C.-Y. Kim, "Survival benefit of levetiracetam in patients treated with concomitant chemoradiotherapy and adjuvant chemotherapy with temozolomide for glioblastoma multiforme," *Cancer*, vol. 121, no. 17, pp. 2926–2932, 2015, doi: 10.1002/cncr.29439.

[94] S. Moriguchi, N. Shioda, Y. Yamamoto, H. Tagashira, and K. Fukunaga, "The t-type voltage-gated calcium channel as a molecular target of the novel cognitive enhancer st101: enhancement of long-term potentiation and camkii autophosphorylation in rat cortical slices," *Journal of neurochemistry*, vol. 121, no. 1, pp. 44–53, 2012, doi: 10.1111/j.1471-4159.2012.07667.x.

[95] L. S. Hu, A. Hawkins-Daarud, L. Wang, J. Li, and K. R. Swanson, "Imaging of intratumoral heterogeneity in high-grade glioma," *Cancer letters*, vol. 477, pp. 97– 106, 2020, doi: 10.1016/j.canlet.2020.02.025.

[96] J.-L. Yan, C. Li, A. van der Hoorn, N. R. Boonzaier, T. Matys, and S. J. Price, "A neural network approach to identify the peritumoral invasive areas in glioblastoma patients by using mr radiomics," *Scientific reports*, vol. 10, no. 1, pp. 1–10, 2020, doi: 10.1038/s41598-020-66691-6.

[97] M. Qazi, P. Vora, C. Venugopal, S. Sidhu, J. Moffat, C. Swanton, and S. Singh, "Intratumoral heterogeneity: pathways to treatment resistance and relapse in human glioblastoma," *Annals of Oncology*, vol. 28, no. 7, pp. 1448–1456, 2017, doi: 10.1093/ annonc/mdx169.

[98] J.-M. Lem´ee, A. Clavreul, and P. Menei, "Intratumoral heterogeneity in glioblastoma:

don't forget the peritumoral brain zone," *Neuro-oncology*, vol. 17, no. 10, pp. 1322–1332, 2015, doi: 10.1093/neuonc/nov119.

[99] J. M. Kampa, U. Kellner, C. Marsching, C. Ramallo Guevara, U. J. Knappe, M. Sahin, M. Giamp`a, K. Niehaus, and H. Bednarz, "Glioblastoma multiforme: Metabolic differences to peritumoral tissue and idh-mutated gliomas revealed by mass spectrometry imaging," *Neuropathology*, vol. 40, no. 6, pp. 546–558, 2020, doi: 10.1111/neup.12671.

[100] A. D'Alessio, G. Proietti, G. Sica, and B. M. Scicchitano, "Pathological and molecular features of glioblastoma and its peritumoral tissue," *Cancers*, vol. 11, no. 4, p. 469, 2019, doi: 10.3390/cancers11040469.

[101] J. D. Bernstock, J. H. Mooney, A. Ilyas, G. Chagoya, D. Estevez-Ordonez, A. Ibrahim, and I. Nakano, "Molecular and cellular intratumoral heterogeneity in primary glioblastoma: clinical and translational implications," *Journal of neurosurgery*, vol. 133, no. 3, pp. 655–663, 2019, doi: 10.3171/2019.5.JNS19364.

[102] M. Alieva, V. Leidgens, M. J. Riemenschneider, C. A. Klein, P. Hau, and J. van Rheenen, "Intravital imaging of glioma border morphology reveals distinctive cellular dynamics and contribution to tumor cell invasion," *Scientific reports*, vol. 9, no. 1, pp. 1–11, 2019, doi: 10.1038/s41598-019-38625-4.

[103] A. Hatcher, K. Yu, J. Meyer, I. Aiba, B. Deneen, J. L. Noebels *et al.*, "Pathogenesis of peritumoral hyperexcitability in an immunocompetent crispr-based glioblastoma model," *The Journal of clinical investigation*, vol. 130, no. 5, 2020, doi: 10.1172/JCI133316.

[104] M. Miyai, H. Tomita, A. Soeda, H. Yano, T. Iwama, and A. Hara, "Current trends in mouse models of glioblastoma," *Journal of neuro-oncology*, vol. 135, no. 3, pp. 423–432, 2017, doi: 10.1007/s11060-017-2626-2.

[105] F. L. Robertson, M.-A. Marqu´es-Torrej´on, G. M. Morrison, and S. M. Pollard, "Experimental models and tools to tackle glioblastoma," *Disease models & mechanisms*, vol. 12, no. 9, 2019, doi: 10.1242/dmm.040386.

[106] T. S. Jones and E. C. Holland, "Animal models for glioma drug discovery," *Expert Opinion on Drug Discovery*, vol. 6, no. 12, pp. 1271–1283, 2011, doi: 10.1517/17460441.2011.632628.

[107] M. Candolfi, J. F. Curtin, W. S. Nichols, A. G. Muhammad, G. D. King, G. E. Pluhar, E. A. McNiel, J. R. Ohlfest, A. B. Freese, P. F. Moore *et al.*, "Intracranial glioblastoma models in preclinical neuro-oncology: neuropathological characterization and tumor

progression," *Journal of neuro-oncology*, vol. 85, no. 2, pp. 133–148, 2007, doi: 10.1007/s11060-007-9400-9.

[108] T. Szatm´ari, K. Lumniczky, S. D´esaknai, S. Trajcevski, E. J. H´ıdv´egi, H. Hamada, and G. S´afr´any, "Detailed characterization of the mouse glioma 261 tumor model for experimental glioblastoma therapy," *Cancer science*, vol. 97, no. 6, pp. 546–553, 2006, doi: 10.1111/j.1349-7006.2006.00208.x.

[109] S. R. A. Llaguno, X. Xie, and L. F. Parada, "Cell of origin and cancer stem cells in tumor suppressor mouse models of glioblastoma," in *Cold Spring Harbor symposia on quantitative biology*, vol. 81. Cold Spring Harbor Laboratory Press, 2016, pp. 31–36, doi: 10.1101/sqb.2016.81.030973.

[110] Y. Zhu, F. Guignard, D. Zhao, L. Liu, D. K. Burns, R. P. Mason, A. Messing, and L. F. Parada, "Early inactivation of p53 tumor suppressor gene cooperating with nf1 loss induces malignant astrocytoma," *Cancer cell*, vol. 8, no. 2, pp. 119–130, 2005, doi: 10.1016/j.ccr.2005.07.004.

[111] E. C. Holland, J. Celestino, C. Dai, L. Schaefer, R. E. Sawaya, and G. N. Fuller, "Combined activation of ras and akt in neural progenitors induces glioblastoma formation in mice," *Nature genetics*, vol. 25, no. 1, pp. 55–57, 2000, doi: 10.1038/75596.

[112] Q. Wei, L. Clarke, D. K. Scheidenhelm, B. Qian, A. Tong, N. Sabha, Z. Karim, N. A. Bock, R. Reti, R. Swoboda *et al.*, "High-grade glioma formation results from postnatal pten loss or mutant epidermal growth factor receptor expression in a transgenic mouse glioma model," *Cancer research*, vol. 66, no. 15, pp. 7429–7437, 2006, doi: 10.1158/ 0008-5472.CAN-06-0712.

[113] T. Marumoto, A. Tashiro, D. Friedmann-Morvinski, M. Scadeng, Y. Soda, F. H. Gage, and I. M. Verma, "Development of a novel mouse glioma model using lentiviral vectors," *Nature medicine*, vol. 15, no. 1, pp. 110–116, 2009, doi: 10.1038/nm.1863.

[114] M. Pathania, N. De Jay, N. Maestro, A. S. Harutyunyan, J. Nitarska, P. Pahlavan, S. Henderson, L. G. Mikael, A. Richard-Londt, Y. Zhang *et al.*, "H3. 3k27m cooperates with trp53 loss and pdgfra gain in mouse embryonic neural progenitor cells to induce invasive high-grade gliomas," *Cancer cell*, vol. 32, no. 5, pp. 684–700, 2017, doi: 10. 1016/j.ccell.2017.09.014.

[115] F. Chen, A. J. Becker, and J. J. LoTurco, "Contribution of tumor heterogeneity in a new animal model of cns tumors," *Molecular Cancer Research*, vol. 12, no. 5, pp. 742–753, 2014, doi: 10.1158/1541-7786.MCR-13-0531.

[116] F. Chen, “Development of novel tools for radial glia lineage tracing and modeling central nervous system tumor,” 2014, url: https://citeseerx.ist.psu.edu/viewdoc/download?doi=10.1.1.907.8036&rep=rep1&type=pdf.

[117] P. A. M. Dirac, “The quantum theory of dispersion,” *Proceedings of the Royal Society of London. Series A, Containing Papers of a Mathematical and Physical Character*, vol. 114, no. 769, pp. 710–728, 1927, doi: 10.1098/rspa.1927.0071.

[118] M. G. Mayer, “Uber elementarakte mit zwei quantenspru¨ngen,”¨ *Annalen der Physik*, vol. 401, no. 3, pp. 273–294, 1931, doi: 10.1002/andp.19314010303.

[119] C. J. Sheppard, “Multiphoton microscopy: a personal historical review, with some future predictions,” *Journal of biomedical optics*, vol. 25, no. 1, p. 014511, 2020, doi: 10.1117/1.JBO.25.1.014511.

[120] W. Denk, J. H. Strickler, and W. W. Webb, “Two-photon laser scanning fluorescence microscopy,” *Science*, vol. 248, no. 4951, pp. 73–76, 1990, doi: 10.1126/science.2321027.

[121] L. Gibb and D. Matthews, “Two photon microscopy and second harmonic generation,” *Report*, 2002, url: https://neurophysics.ucsd.edu/courses/physics 173 273/Nonlinear _optics.pdf.

[122] M. Carter and J. C. Shieh, *Guide to research techniques in neuroscience*. Academic Press, 2015, url: https://zu.edu.jo/UploadFile/Library/E Books/Files/LibraryFile _91258 7.pdf.

[123] F. Helmchen and W. Denk, “Deep tissue two-photon microscopy,” *Nature methods*, vol. 2, no. 12, pp. 932–940, 2005, doi: 10.1038/nmeth818.

[124] “Multiphoton laser fluorescence microscopy,” http://candle.am/microscopy/, accessed: 2021-01-28.

[125] J. I. Ausman, W. R. Shapiro, and D. P. Rall, “Studies on the chemotherapy of experimental brain tumors: development of an experimental model,” *Cancer research*, vol. 30, no. 9, pp. 2394–2400, 1970, pmid: 5475483.

[126] G. E. Plautz, J. E. Touhalisky, and S. Shu, “Treatment of murine gliomas by adoptive transfer ofex vivoactivated tumor-draining lymph node cells,” *Cellular immunology*, vol. 178, no. 2, pp. 101–107, 1997, doi: 10.1006/cimm.1997.1140.

[127] A. Natsume, M. Mizuno, Y. Ryuke, and J. Yoshida, “Antitumor effect and cellular immunity activation by murine interferon-β gene transfer against intracerebral glioma in mouse,” *Gene therapy*, vol. 6, no. 9, pp. 1626–1633, 1999, doi: 10.1038/sj.gt.3300990.

[128] R. P. Glick, R. P. Glick, T. Lichtor, T. Lichtor, T. S. Kim, S. Ilangovan, and E. P. Cohen, "Fibroblasts genetically engineered to secrete cytokines suppress tumor growth and induce antitumor immunity to a murine glioma in vivo: Case report," *Neurosurgery*, vol. 36, no. 3, pp. 548–555, 1995, doi: 10.1227/00006123-199503000-00014.

[129] J. L. Bos, "Ras oncogenes in human cancer: a review," *Cancer research*, vol. 49, no. 17, pp. 4682–4689, 1989, pmid: 2547513.

[130] D. Sidransky, T. Mikkelsen, K. Schwechheimer, M. L. Rosenblum, and B. Vogelstein, "Clonal expansion of p53 mutant cells is associated with brain tumour progression," *Nature*, vol. 355, no. 6363, pp. 846–847, 1992, doi: 10.1038/355846a0.

[131] N. Ishii, M. Tada, M.-F. Hamou, R. C. Janzer, K. Meagher-Villemure, O. D. Wiestler, N. De Tribolet, and E. G. Van Meir, "Cells with tp53 mutations in low grade astrocytic tumors evolve clonally to malignancy and are an unfavorable prognostic factor," *Oncogene*, vol. 18, no. 43, pp. 5870–5878, 1999, doi: 10.1038/sj.onc.1203241.

[132] R. Boyd, "Chapter 1-the nonlinear optical susceptibility nonlinear optics (pp. 1-67)," 2008, url: https://booksite.elsevier.com/samplechapters/9780123694706/ Sample_Chapters/02~Chapter 1.pdf.

[133] X. Jiang, J. Zhong, Y. Liu, H. Yu, S. Zhuo, and J. Chen, "Two-photon fluorescence and second-harmonic generation imaging of collagen in human tissue based on multiphoton microscopy," *Scanning*, vol. 33, no. 1, pp. 53–56, 2011, doi: 10.1002/sca.20219.

[134] J. E. P´erez, J. Kopecky, E. Visse, A. Darabi, and P. Siesj¨o, "Convection-enhanced delivery of temozolomide and whole cell tumor immunizations in gl261 and kr158 experimental mouse gliomas," *BMC cancer*, vol. 20, no. 1, pp. 1–12, 2020, doi: 10. 1186/s12885-019-6502-7.

[135] C.-A. Liu, C.-Y. Chang, K.-W. Hsueh, H.-L. Su, T.-W. Chiou, S.-Z. Lin, and H.J. Harn, "Migration/invasion of malignant gliomas and implications for therapeutic treatment," *International journal of molecular sciences*, vol. 19, no. 4, p. 1115, 2018, doi: 10.3390/ijms19041115.

[136] T. Oh, S. Fakurnejad, E. T. Sayegh, A. J. Clark, M. E. Ivan, M. Z. Sun, M. Safaee, O. Bloch, C. D. James, and A. T. Parsa, "Immunocompetent murine models for the study of glioblastoma immunotherapy," *Journal of translational medicine*, vol. 12, no. 1, pp. 1–10, 2014, doi: 10.1186/1479-5876-12-107.

[137] K. J. McKelvey, A. L. Hudson, R. Prasanna Kumar, J. S. Wilmott, G. H. Attrill, G. V. Long, R. A. Scolyer, S. J. Clarke, H. R. Wheeler, C. I. Diakos *et al.*, "Temporal and spatial

modulation of the tumor and systemic immune response in the murine gl261 glioma model," *PloS one*, vol. 15, no. 4, p. e0226444, 2020, doi: 10.1371/journal.pone. 0226444.

[138] E. W. Newcomb and D. Zagzag, "The murine gl261 glioma experimental model to assess novel brain tumor treatments," in *CNS cancer*. Springer, 2009, pp. 227–241, doi: 10.1007/978-1-60327-553-8 12.

[139] D. Zagzag, D. C. Miller, L. Chiriboga, H. Yee, and E. W. Newcomb, "Green fluorescent protein immunohistochemistry as a novel experimental tool for the detection of glioma cell invasion in vivo," *Brain pathology*, vol. 13, no. 1, pp. 34–37, 2003, doi: 10.1111/j. 1750-3639.2003.tb00004.x.

[140] E. Tantillo, E. Vannini, C. Cerri, C. Spalletti, A. Colistra, C. M. Mazzanti, M. Costa, and M. Caleo, "Differential roles of pyramidal and fast-spiking, gabaergic neurons in the control of glioma cell proliferation," *Neurobiology of Disease*, vol. 141, p. 104942, 2020, doi: 10.1016/j.nbd.2020.104942.

[141] G. Seano, H. T. Nia, K. E. Emblem, M. Datta, J. Ren, S. Krishnan, J. Kloepper, M. C. Pinho, W. W. Ho, M. Ghosh *et al.*, "Solid stress in brain tumours causes neuronal

loss and neurological dysfunction and can be reversed by lithium," *Nature biomedical engineering*, vol. 3, no. 3, pp. 230–245, 2019, doi: 10.1038/s41551-018-0334-7.

[142] T. Stankovic, T. Ranjelovic, M. Dragoj, S. S. Buric, L. Fernandez, I. Ochoa, V. M. Perez-Garcia, and M. Pesic, "In vitro biomimetic models for glioblastoma-a promising tool for drug response studies," *Drug Resistance Updates*, vol. 55, p. 100753, 2021, doi: 10.1016/j.drup.2021.100753.

[143] M. E. Katt, A. L. Placone, A. D. Wong, Z. S. Xu, and P. C. Searson, "In vitro tumor models: advantages, disadvantages, variables, and selecting the right platform," *Frontiers in bioengineering and biotechnology*, vol. 4, p. 12, 2016, doi: 10.3389/fbioe. 2016.00012.

[144] O. Cozzolino, F. Sicca, E. Paoli, F. Trovato, F. M. Santorelli, G. M. Ratto, and M. Marchese, "Evolution of epileptiform activity in zebrafish by statistical-based integration of electrophysiology and 2-photon ca2+ imaging," *Cells*, vol. 9, no. 3, p. 769, 2020, doi: 10.3390/cells9030769.

[145] C. C. Naus, Q. Aftab, and W. C. Sin, "Common mechanisms linking connexin43 to neural progenitor cell migration and glioma invasion," in *Seminars in cell & developmental biology*, vol. 50. Elsevier, 2016, pp. 59–66, doi: 10.1016/j.semcdb.2015.12.008.

[146] D. R. Croft and M. F. Olson, “Regulating the conversion between rounded and elongated modes of cancer cell movement,” *Cancer cell*, vol. 14, no. 5, pp. 349–351, 2008, doi: 10.1016/j.ccr.2008.10.009.

[147] K. Wolf, I. Mazo, H. Leung, K. Engelke, U. H. Von Andrian, E. I. Deryugina, A. Y. Strongin, E.-B. Broocker, and P. Friedl, “Compensation mechanism in tumor cell migration: mesenchymal–amoeboid transition after blocking of pericellular proteolysis,” *The Journal of cell biology*, vol. 160, no. 2, pp. 267–277, 2003, doi: 10.1083/jcb.200209006.

[148] E. Alizadeh, J. Castle, A. Quirk, C. D. Taylor, W. Xu, and A. Prasad, “Cellular morphological features are predictive markers of cancer cell state,” *Computers in Biology and Medicine*, vol. 126, p. 104044, 2020, doi: 10.1016/j.compbiomed.2020. 104044.

[149] C. Cui, R. Merritt, L. Fu, and Z. Pan, “Targeting calcium signaling in cancer therapy,” *Acta pharmaceutica sinica B*, vol. 7, no. 1, pp. 3–17, 2017, doi: 10.1016/j.apsb.2016. 11.001.

[150] S. Deaglio and T. N. Hartmann, “The importance of tumor–host interactions in adult b-cell leukemias and lymphomas,” 2020, doi: 10.3390/ijms21186915.

[151] F. P. Caruso, L. Garofano, F. D’Angelo, K. Yu, F. Tang, J. Yuan, J. Zhang, L. Cerulo, S. M. Pagnotta, D. Bedognetti *et al.*, “A map of tumor–host interactions in glioma at single-cell resolution,” *GigaScience*, vol. 9, no. 10, p. giaa109, 2020, doi: 10.1093/ gigascience/giaa109.

[152] L. Leiss, E. Mutlu, M. A. Rahman, and P. Ø. Enger, “Tumor-host interactions in malignant gliomas,” in *Biomarkers of the Tumor Microenvironment*, 2017, pp. 465– 479, doi: 10.1007/978-3-319-39147-2 20.

[153] A. B. Parekh, “Decoding cytosolic ca2+ oscillations,” *Trends in biochemical sciences*, vol. 36, no. 2, pp. 78–87, 2011, doi: 10.1016/j.tibs.2010.07.013.

[154] H. S. Venkatesh, W. Morishita, A. C. Geraghty, D. Silverbush, S. M. Gillespie, M. Arzt, L. T. Tam, C. Espenel, A. Ponnuswami, L. Ni *et al.*, “Electrical and synaptic integration of glioma into neural circuits,” *Nature*, vol. 573, no. 7775, pp. 539–545, 2019, doi: 10.1038/s41586-019-1563-y.

[155] V. Venkataramani, D. I. Tanev, C. Strahle, A. Studier-Fischer, L. Fankhauser, T. Kessler, C. K¨orber, M. Kardorff, M. Ratliff, R. Xie *et al.*, “Glutamatergic synaptic input to glioma cells drives brain tumour progression,” *Nature*, vol. 573, no. 7775, pp. 532–538, 2019, doi: 10.1038/s41586-019-1564-x.

[156] M. K. Montgomery, S. H. Kim, A. Dovas, H. T. Zhao, A. R. Goldberg, W. Xu, A. J. Yagielski, M. K. Cambareri, K. B. Patel, A. Mela *et al.*, “Glioma-induced alterations in neuronal

activity and neurovascular coupling during disease progression," *Cell reports*, vol. 31, no. 2, p. 107500, 2020, doi: 10.1016/j.celrep.2020.03.064.

[157] J. S´api, L. Kov´acs, D. A. Drexler, P. Kocsis, D. Gaj´ari, and Z. S´api, "Tumor volume estimation and quasi-continuous administration for most effective bevacizumab therapy," *PLoS One*, vol. 10, no. 11, p. e0142190, 2015, doi: 10.1371/journal.pone.0142190.

[158] E. A. Pnevmatikakis and A. Giovannucci, "Normcorre: An online algorithm for piecewise rigid motion correction of calcium imaging data," *Journal of neuroscience methods*, vol. 291, pp. 83–94, 2017, doi: 10.1016/j.jneumeth.2017.07.031.

[159] J. E. Visvader, "Cells of origin in cancer," *Nature*, vol. 469, no. 7330, pp. 314–322, 2011, doi: 10.1038/nature09781.

[160] U. Oleksiewicz and M. Machnik, "Causes, effects, and clinical implications of perturbed patterns within the cancer epigenome," in *Seminars in Cancer Biology*, 2020, doi: 10.1016/j.semcancer.2020.12.014.

[161] R. G. Verhaak, K. A. Hoadley, E. Purdom, V. Wang, Y. Qi, M. D. Wilkerson, C. R. Miller, L. Ding, T. Golub, J. P. Mesirov *et al.*, "Integrated genomic analysis identifies clinically relevant subtypes of glioblastoma characterized by abnormalities in pdgfra,

idh1, egfr, and nf1," *Cancer cell*, vol. 17, no. 1, pp. 98–110, 2010, doi: 10.1016/j.ccr. 2009.12.020.

[162] S. Orsulic, "An rcas-tva-based approach to designer mouse models," *Mammalian genome*, vol. 13, no. 10, pp. 543–547, 2002, doi: 10.1007/s00335-002-4003-4.

[163] F. Chen and J. LoTurco, "A method for stable transgenesis of radial glia lineage in rat neocortex by piggybac mediated transposition," *Journal of neuroscience methods*, vol. 207, no. 2, pp. 172–180, 2012, doi: 10.1016/j.jneumeth.2012.03.016.

[164] A. Koga, M. Suzuki, H. Inagaki, Y. Bessho, and H. Hori, "Transposable element in fish," *Nature*, vol. 383, no. 6595, pp. 30–30, 1996, doi: 10.1038/383030a0.

[165] Z. Ivics, P. B. Hackett, R. H. Plasterk, and Z. Izsv´ak, "Molecular reconstruction of sleeping beauty, a tc1-like transposon from fish, and its transposition in human cells," *Cell*, vol. 91, no. 4, pp. 501–510, 1997, doi: 10.1016/s0092-8674(00)80436-5.

[166] M. J. Fraser, L. Cary, K. Boonvisudhi, and H.-G. H. Wang, "Assay for movement of lepidopteran transposon ifp2 in insect cells using a baculovirus genome as a target dna," *Virology*, vol. 211, no. 2, pp. 397–407, 1995, doi: 10.1006/viro.1995.1422.

[167] I. Laptev, N. Raevskaya, N. Filimonova, and S. Sineoky, "The piggybac transposon as a tool in genetic engineering," *Applied biochemistry and microbiology*, vol. 53, no. 9, pp. 874–881, 2017, doi: 10.1134/S000368381709006X.

[168] L. Shu, D. Wang, N. F. Saba, and Z. G. Chen, "A historic perspective and overview of h-ras structure, oncogenicity, and targeting," *Molecular cancer therapeutics*, vol. 19, no. 4, pp. 999–1007, 2020, doi: 10.1158/1535-7163.MCT-19-0660.

[169] I. A. Prior, F. E. Hood, and J. L. Hartley, "The frequency of ras mutations in cancer," *Cancer research*, vol. 80, no. 14, pp. 2969–2974, 2020, doi: 10.1158/0008-5472. CAN-19-3682.

[170] F. Hertwig, K. Meyer, S. Braun, S. Ek, R. Spang, C. V. Pfenninger, I. Artner, G. Prost, X. Chen, J. A. Biegel *et al.*, "Definition of genetic events directing the development of distinct types of brain tumors from postnatal neural stem/progenitor cells," *Cancer research*, vol. 72, no. 13, pp. 3381–3392, 2012, doi: 10.1158/0008-5472.CAN-11-3525.

[171] S. M. Lyons, E. Alizadeh, J. Mannheimer, K. Schuamberg, J. Castle, B. Schroder, P. Turk, D. Thamm, and A. Prasad, "Changes in cell shape are correlated with metastatic potential in murine and human osteosarcomas," *Biology open*, vol. 5, no. 3, pp. 289–299, 2016, doi: 10.1242/bio.013409.

[172] F. Aguado, J. F. Espinosa-Parrilla, M. A. Carmona, and E. Soriano, "Neuronal activity regulates correlated network properties of spontaneous calcium transients in astrocytes in situ," *Journal of Neuroscience*, vol. 22, no. 21, pp. 9430–9444, 2002, doi: 10.1523/JNEUROSCI.22-21-09430.2002.

[173] J. S. Rao, "Molecular mechanisms of glioma invasiveness: the role of proteases," *Nature Reviews Cancer*, vol. 3, no. 7, pp. 489–501, 2003, doi: 10.1038/nrc1121.

[174] A. Li, J. C. Dawson, M. Forero-Vargas, H. J. Spence, X. Yu, I. K¨onig, K. Anderson, and L. M. Machesky, "The actin-bundling protein fascin stabilizes actin in invadopodia and potentiates protrusive invasion," *Current biology*, vol. 20, no. 4, pp. 339–345, 2010, doi: 10.1016/j.cub.2009.12.035.

[175] W. Yang, P.-f. Wu, J.-x. Ma, M.-j. Liao, L.-s. Xu, and L. Yi, "Trpv4 activates the cdc42/n-wasp pathway to promote glioblastoma invasion by altering cellular protrusions," *Scientific reports*, vol. 10, no. 1, pp. 1–15, 2020, doi: 10.1038/ s41598-020-70822-4.

[176] M. Portela and S. Casas-Tint´o, "New cellular dimensions on glioblastoma progression," *Neuroscience insights*, vol. 15, p. 2633105520923076, 2020, doi: 10.1177/ 2633105520923076.

[177] M. Takkunen, M. Hukkanen, M. Liljestr¨om, R. Grenman, and I. Virtanen, “Podosomelike structures of non-invasive carcinoma cells are replaced in epithelial-mesenchymal transition by actin comet-embedded invadopodia,” *Journal of cellular and molecular medicine*, vol. 14, no. 6b, pp. 1569–1593, 2010, doi: 10.1111/j.1582-4934.2009.00868.x.

[178] M. Dal Maschio, D. Ghezzi, G. Bony, A. Alabastri, G. Deidda, M. Brondi, S. S. Sato, R. P. Zaccaria, E. Di Fabrizio, G. M. Ratto *et al.*, “High-performance and site-directed in utero electroporation by a triple-electrode probe,” *Nature communications*, vol. 3, no. 1, pp. 1–11, 2012, doi: 10.1038/ncomms1961.

[179] J. Szczurkowska, A. W. Cwetsch, M. Dal Maschio, D. Ghezzi, G. M. Ratto, and L. Cancedda, “Targeted in vivo genetic manipulation of the mouse or rat brain by in utero electroporation with a triple-electrode probe,” *Nature Protocols*, vol. 11, no. 3, p. 399, 2016, doi: 10.1038/nprot.2016.014.

[180] Q. Cheng, J. Li, F. Fan, H. Cao, Z.-Y. Dai, Z.-Y. Wang, and S.-S. Feng, “Identification and analysis of glioblastoma biomarkers based on single cell sequencing,” *Frontiers in bioengineering and biotechnology*, vol. 8, p. 167, 2020, doi: 10.3389/fbioe.2020.00167.

[181] S. M. McMahon and M. B. Jackson, “An inconvenient truth: calcium sensors are calcium buffers,” *Trends in neurosciences*, vol. 41, no. 12, pp. 880–884, 2018, doi: 10.1016/j.tins.2018.09.005.

[182] P. Wahle, I. Gasterst¨adt, A. Jack, T. Stahlhut, L.-M. Rennau, and S. Gonda, “Genetically encoded calcium indicators can impair dendrite growth of cortical neurons,” *Frontiers in cellular neuroscience*, vol. 14, p. 307, 2020, doi: 10.3389/fncel.2020. 570596.

[183] R. Sando, K. Baumgaertel, S. Pieraut, N. Torabi-Rander, T. J. Wandless, M. Mayford, and A. Maximov, “Inducible control of gene expression with destabilized cre,” *Nature methods*, vol. 10, no. 11, pp. 1085–1088, 2013, doi: 10.1038/nmeth.2640.

[184] F. Trovato, R. Parra, E. Pracucci, S. Landi, O. Cozzolino, G. Nardi, F. Cruciani, V. Pillai, L. Mosti, A. W. Cwetsch *et al.*, “Modelling genetic mosaicism of neurodevelopmental disorders in vivo by a cre-amplifying fluorescent reporter,” *Nature communications*, vol. 11, no. 1, pp. 1–13, 2020, doi: 10.1038/s41467-020-19864-w.

APPENDIX

Supplementary material for Chapter 3, Section 3.2.3

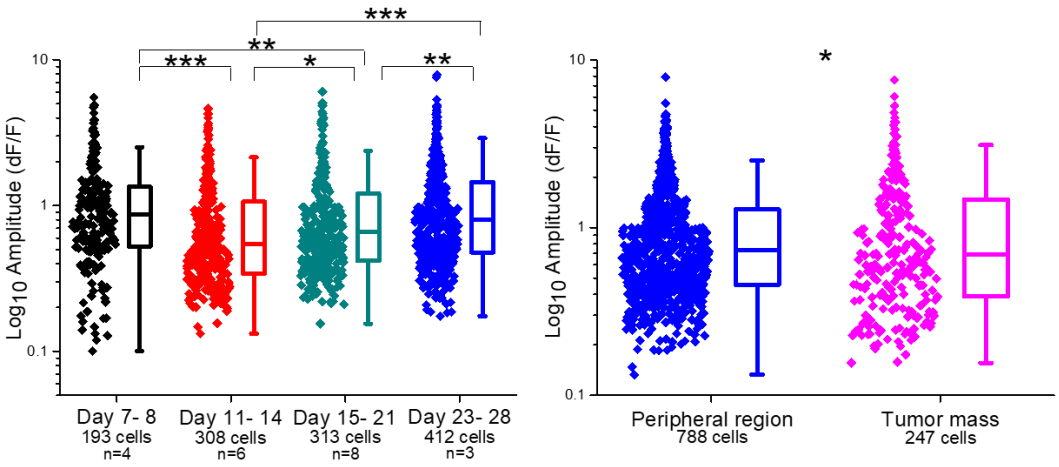

Supplementary Figure 1: Amplitude of calcium events of GL261-TF tumor cells. Box plot on the right represents amplitude of $(Ca^{2+})_i$ events as a function of time (days post injection) while the box plot on the left represents amplitude of $(Ca^{2+})_i$ events at different tumor regions. This data shows that the amplitude of $(Ca^{2+})_i$ events of the tumor cells are very similar and the population are not very different. It can be seen clearly from the plot on the left, where the level of significance is very low. This is possibly due to the fact that, given the strong cooperativity of GCaMP6 its transfer function is very steep and responses tend to be binarized. P value determined by Mann-Whitney test, ***p<0.001; **p<0.01; *p<0.05.

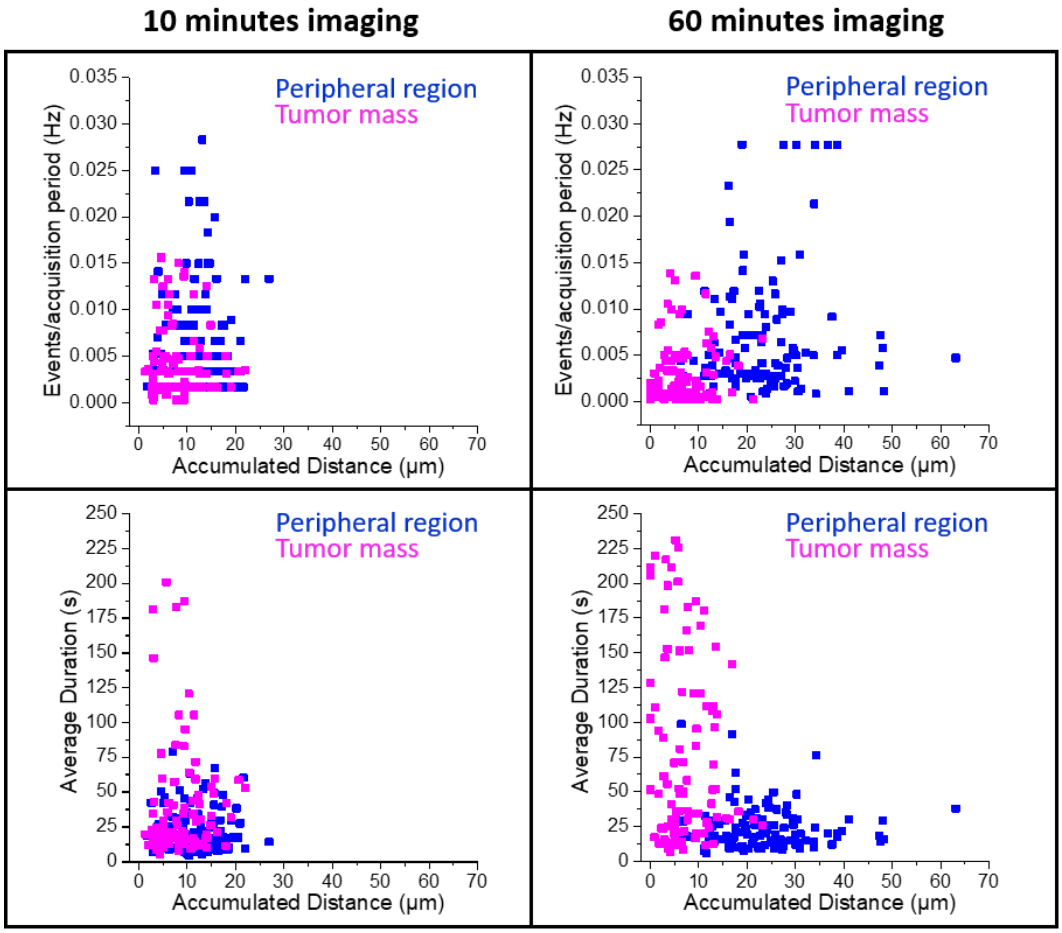

Supplementary Figure 2: Relationship between GBM cell migration and $(Ca^{2+})_i$ dynamics. Figure represents plots of frequency and average duration of $(Ca^{2+})_i$ events as a function of accumulated distance traveled by GL261 cells. In the 10 minutes' recording, we can observe a population of cells that has higher number of $(Ca^{2+})_i$ events in the peripheral region, while another population of cells that has higher average duration of $(Ca^{2+})_i$ events in the tumor mass. However, in the 60 minutes' recording, the two previously mentioned population can be seen distinctly with cells in the periphery migrated further compared to the cells in the tumor mass. This shows that the relationship observed between GBM cell migration and $(Ca^{2+})_i$ dynamics are from the contribution of population of cells rather than individual cells.

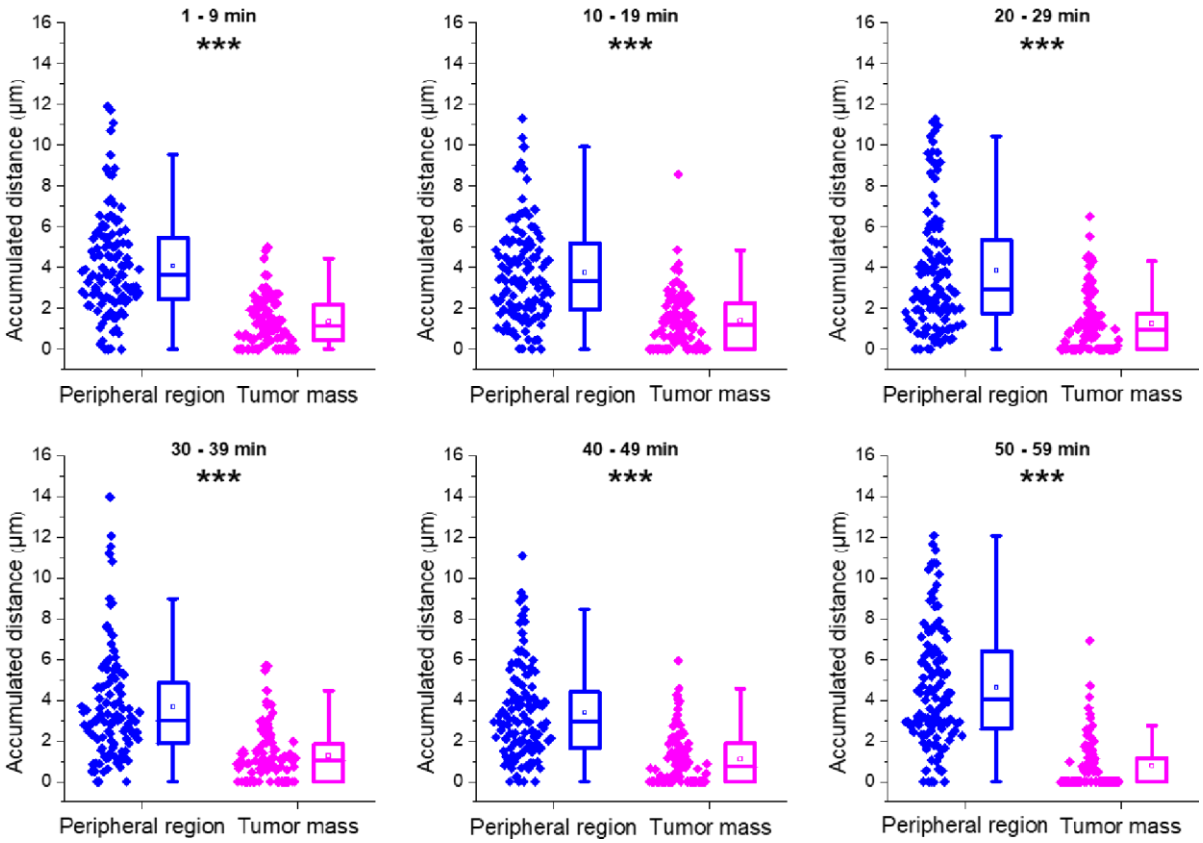

Supplementary Figure 3: 60 minutes' cell motility at different regions of the tumor. Box plots shows the quantification of cell motility of a 60 minutes' acquisition that is broken down to every consecutive 10 minutes' sequences. Motility of cells were computed by measuring the accumulated distance traveled by the cells. These plots show no distinct reduction of cell motility for both tumor regions throughout the duration of acquisition which stands as a proof that there was no indication of phototoxicity. P value determined by Mann-Whitney test, ***p<0.001.

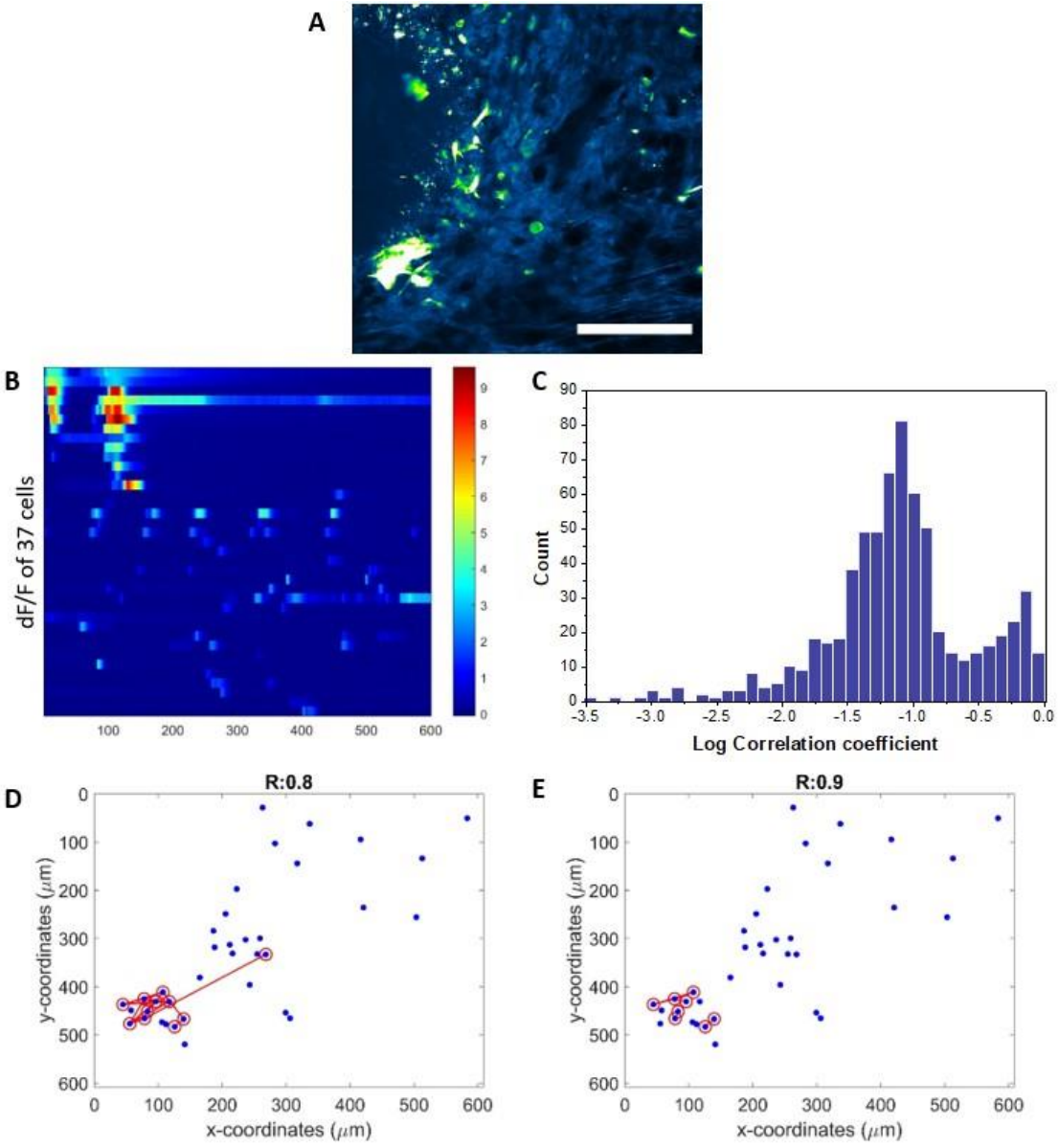

.

Supplementary Figure 4: Cluster activation in Mouse 2. **A)** Standard deviation projection of a 10 minutes' movie sequence, 84 μm depth from the surface, acquired from a two photon microscope (scale bar: 200um). **B)** Raster plot corresponding to dF/F of $(Ca^{2+})_i$ fluctuation of 37 cells belonging to clusters and remote cells. ROIs from clusters were arranged together in the raster plot for better visualization of dF/F activation. **C)** Distribution of correlation coefficient of $(Ca^{2+})_i$ traces from the selected 37 ROIs. **D and E)** Functional connectivity map of cells (red lines) at correlation threshold, R≥0.8 and R≥0.9. Centroid of all ROIs are represented in blue.

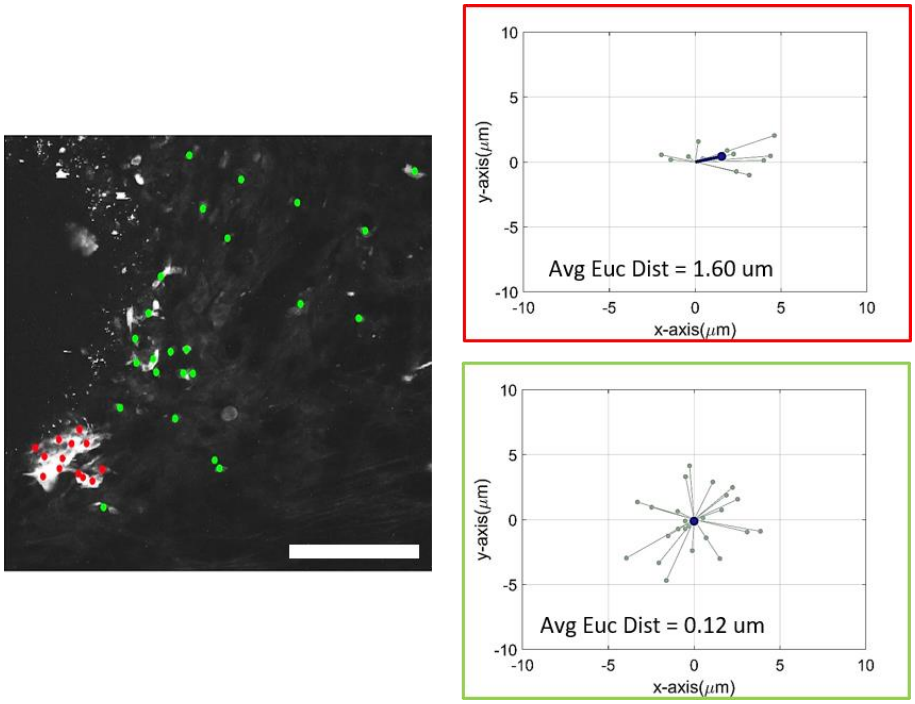

Supplementary Figure 5: Migrational pattern of cell clusters in Mouse 2. Maximum projection of a 10 minutes' time lapse sequence with sampling rate 1.07s (scale bar: 200 μm). Red dots represent centroid of cells that belong to cluster while green dots represent random cells. Cell tracks plot of cluster (in red square) and remote cells (in green square) observed over a period of 10 minutes'. Cell trajectories were plotted starting from xy coordinated (0,0) at time 0 minutes' and the end coordinates. The euclidean distance each cell is represented with a gray marker-line and the weighted average is represented by blue marker-line. (Cluster: 13 cells; Remote cells: 24 cells) (Avg Euc Dist = average euclidean distance).

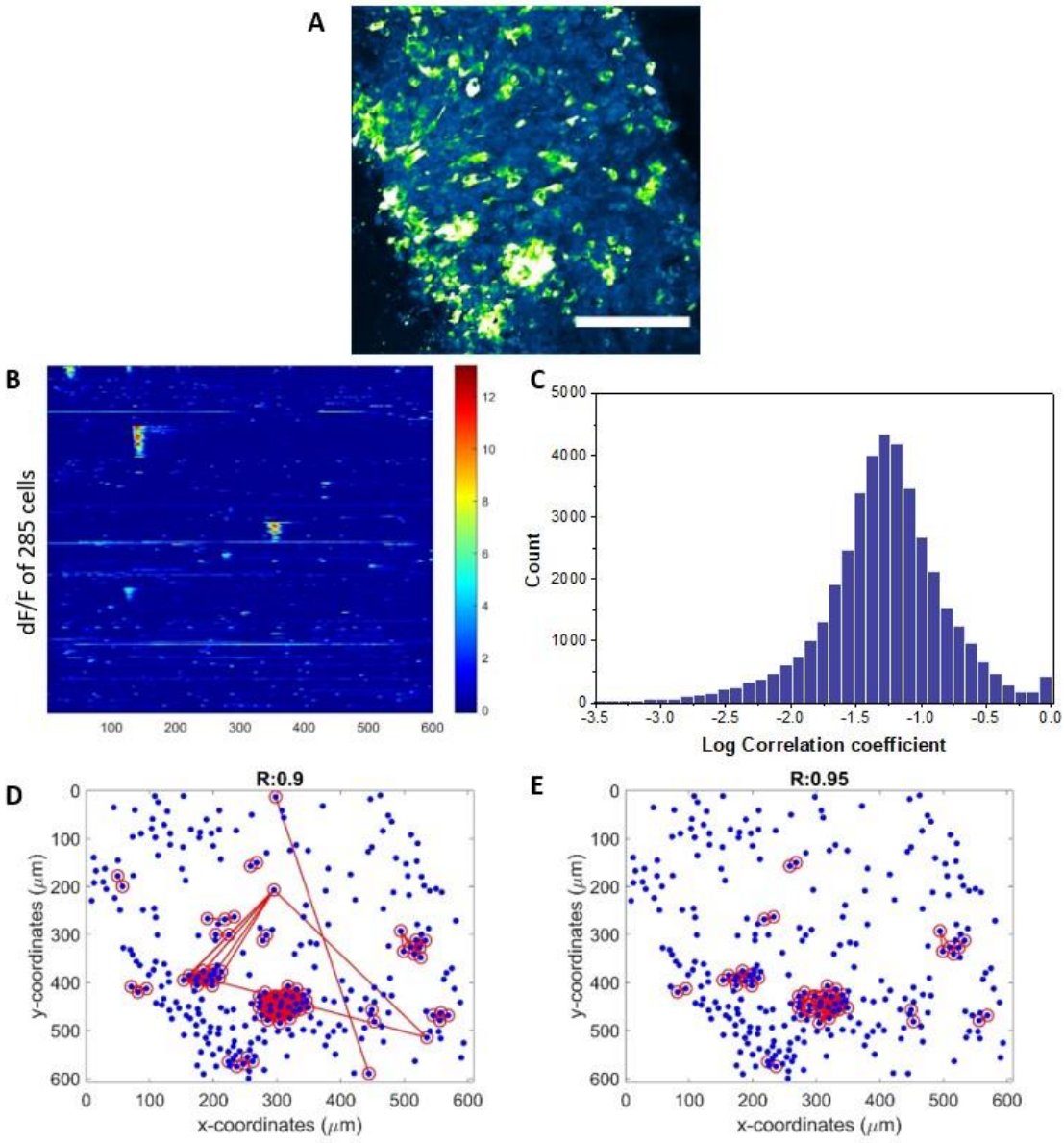

Supplementary Figure 6: Cluster activation in Mouse 3. **A)** Standard deviation projection of a 10 minutes' movie sequence, 90 μm depth from the surface, acquired from a two photon microscope (scale bar: 200um). **B)** Raster plot corresponding to dF/F of $(Ca^{2+})_i$ fluctuation of 285 cells belonging to clusters and remote cells. ROIs from clusters were arranged together in the raster plot for better visualization of dF/F activation. **C)** Distribution of correlation coefficient of $(Ca^{2+})_i$ traces from the selected 285 ROIs. **D and E)** Functional connectivity map of cells (red lines) at correlation threshold, R≥0.9 and R≥0.95. Centroid of all ROIs are represented in blue.

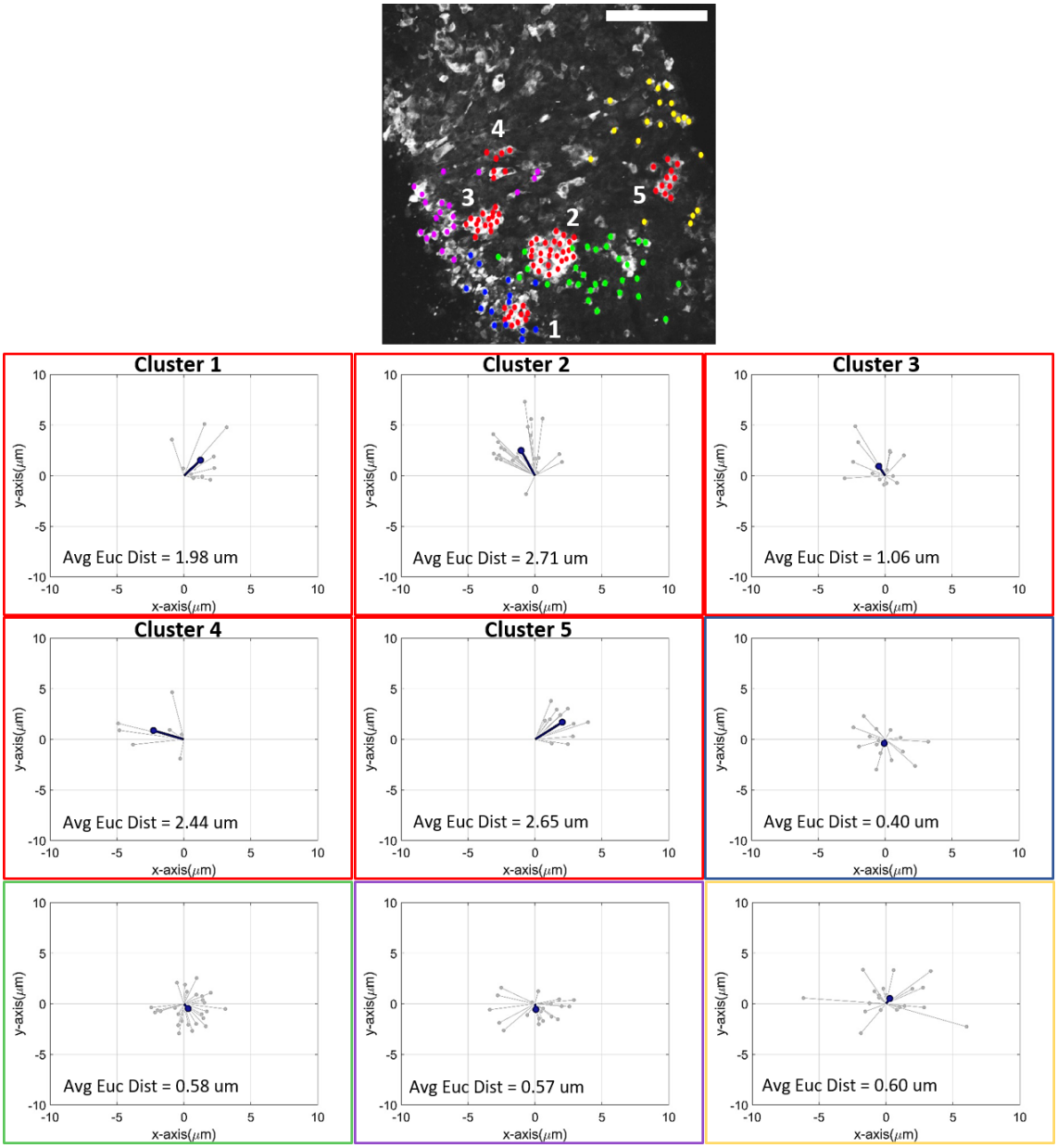

Supplementary Figure 7: Migrational pattern of cell clusters in Mouse 3. Maximum projection of a 10 minutes' time lapse sequence with sampling rate 1.07s (scale bar: 200 μm). Red dots represent centroid of cells that belong to clusters while blue, green, purple and yellow dots represents subsets of random cells. Cell tracks plot of clusters and remote cells are represented in their color coded boxes. The euclidean distance each cell is represented with a gray marker-line and the weighted average is represented by blue marker-line. (Cluster 1: 11 cells; Cluster 2: 26 cells; Cluster 3: 16 cells; Cluster 4: 7 cells; Cluster 5: 11 cells; Remote cells 1: 15 cells; Remote cells 2: 30 cells; Remote cells 3: 20 cells; Remote cells 4: 20 cells) (Avg Euc Dist = average euclidean distance).

Codes used for analysis can be found on GitHub: https://github.com/Vinoshene/GBM codes PhD